ROLE OF FLEXIBILITY IN ROBOTIC FISH

By

Sanaz Bazaz Behbahani

A DISSERTATION

Submitted to
Michigan State University
in partial fulfillment of the requirements
for the degree of

Electrical Engineering — Doctor of Philosophy

2016

ABSTRACT

ROLE OF FLEXIBILITY IN ROBOTIC FISH

By

Sanaz Bazaz Behbahani

Underwater creatures, especially fish, have received significant attention over the past several decades because of their fascinating swimming abilities and behaviors, which have inspired engineers to develop robots that propel and maneuver like real fish. This dissertation is focused on the role of flexibility in robotic fish performance, including the design, dynamic modeling, and experimental validation of flexible pectoral fins, flexible passive joints for pectoral fins, and fins with actively controlled stiffness.

First, the swimming performance and mechanical efficiency of flexible pectoral fins, connected to actuator shafts via rigid links, are studied, where it is found that flexible fins demonstrate advantages over rigid fins in speed and efficiency at relatively low fin-beat frequencies, while the rigid fins outperform the flexible fins at higher frequencies. The presented model offers a promising tool for the design of fin flexibility and swimming gait, to achieve speed and efficiency objectives for the robotic fish.

The traditional rigid joint for pectoral fins requires different speeds for power and recovery strokes in order to produce net thrust and consequently results in control complexity and low speed performance. To address this issue, a novel flexible passive joint is presented where the fin is restricted to rowing motion during both power and recovery strokes. This joint allows the pectoral fin to sweep back passively during the recovery stroke while it follows the prescribed motion of the actuator during the power stroke, which results in net thrust even under symmetric actuation for power and recovery strokes. The dynamic model of a robotic fish equipped with such joints is developed and validated through extensive experiments. Motivated by the need for

design optimization, the model is further utilized to investigate the influences of the joint length and stiffness on the robot locomotion performance and efficiency. An alternative flexible joint for pectoral fins is also proposed, which enables the pectoral fin to operate primarily in the rowing mode, while undergoing passive feathering during the recovery stroke to reduce hydrodynamic drag on the fin. A dynamic model, verified experimentally, is developed to examine the trade-off between swimming speed and mechanical efficiency in the fin design.

Finally, we investigate flexible fins with actively tunable stiffness, enabled by electrorheological (ER) fluids. The tunable stiffness can be used in optimizing the robotic fish speed or maneuverability in different operating regimes. Fins with tunable stiffness are prototyped with ER fluids enclosed between layers of liquid urethane rubber (Vytaflex 10). Free oscillation and base-excited oscillation behaviors of the fins are measured underwater when different electric fields are applied for the ER fluid, which are subsequently used to develop a dynamic model for the stiffness-tunable fins.

To Mohsen, for his advice, patience, and unconditional love; because he always understood.
To my beloved Mom and Dad, who have been a constant source of teaching and support.
To the loving memory of my grandpa, Sartip.

ACKNOWLEDGMENTS

It is a pleasure to thank the many people who made this thesis possible. I am deeply indebted to my advisor, Prof. Xiaobo Tan, for giving me the opportunity to pursue my dreams, without the support and advice of whom I would never have completed this project. I am really happy and lucky that I had the chance to work under his supervision. I learned a lot from his knowledge, enthusiasm, inspiration, and patient guidance throughout my time at Michigan State University.

I would like to thank Prof. Ranjan Mukherjee, Prof. Philip K. McKinley, and Prof. Lixin Dong, for kindly serving on my thesis committee, and being inspiring in many ways. They generously gave their time to offer me insightful comments and advices toward improving this work.

There is no way to express how much it meant to me to have been a member of the Michigan State University and Smart Microsystems Laboratory. These brilliant friends and colleagues inspired me over the many years: Dr. Jianxun Wang, Dr. Feitian Zhang, Dr. Hong Lei, Dr. Jun Zhang, Dr. Anthony J. Clark, Osama En-Nasr, Jason Greenberg, Montassar Sharif, Maria Castano, Thassyo Pinto, Pratap Bhanu Solanki, Mohammed Al-Rubaiai, Cody Thon, and all the other current and former SML students and visitors that I know. Special thanks must go to Mr. John Thon, for his assistance in prototyping the robotic fish platforms. He truly went above and beyond to make sure my robotic fish would run smoothly.

I would like to express my gratitude to the technical and administrative staff of the Electrical and Computer Engineering Department for their assistance during my study at Michigan State University, in particular, Brian Wright, Gregg Mulder, Roxanne Peacock, Meagan Kroll, and Laurie Rashid.

I would like to acknowledge the financial support of my research by National Science Foundation (Grants DBI 0939454, CNS 1059373, CCF 1331852, IIS 0916720, IIS 1319602, IIP 1343413, ECCS 1029683, ECCS 1446793), which I hope will fuel the future learning of those walking in my footsteps.

I cannot forget my friends who went through hard times together, cheered me up, and celebrated each accomplishment: Dr. Jiankun Liu, Dr. Mingwu Gao, Dr. Elaheh Esfahanian, Alireza Ameli, Maliheh Gholami, Dena Izadi, Ali Lahouti, Shima Lahouti, and many others.

I deeply thank my parents, Samad Bazaz Behbahani and Afsaneh Azari for their unconditional support, timely encouragement, and endless patience, and thank my sister, Roxana, and my brother, Rouzbeh, to whom I will always be in debt for their love and encouragement despite the long distance between us. Words alone cannot fully express my appreciation to what they have done for me.

Lastly, and most importantly, I wish to thank my husband and my hero, Dr. Mohsen Mosleh-pour, for always being beside me and giving me motivation to move forward. Who believed in me, often far more than I believed in myself. He has been my best friend and great companion, who loved, supported, encouraged, entertained, and helped me get through this agonizing period in the most positive way. You are the best treasure I can ever dream of.

PREFACE

This dissertation is submitted for the degree of Doctor of Philosophy at the Michigan State University. The research described herein was conducted under supervision of Prof. Xiaobo Tan in the Electrical and Computer Engineering Department, Michigan State University, between August 2011 and December 2016.

This work is to the best of my knowledge original, except where acknowledgment and references are made to previous work.

This work has been presented in the following publications:

- Chapter 2

  S. B. Behbahani, X. Tan, "Role of Pectoral Fin Flexibility in Robotic Fish Performance," *Journal of Nonlinear Science*, Under review, 2016.

- Chapter 3

  S. B. Behbahani, X. Tan, "Design and Modeling of Flexible Passive Rowing Joints for Robotic Fish Pectoral Fins," *IEEE Transactions on Robotics*, Vol. 32, No. 5, pp. 1119-1132, 2016.

- Chapter 4

  S. B. Behbahani, X. Tan, "Bio-inspired Flexible Joints with Passive Feathering for Robotic Fish Pectoral Fins," *Bioinspiration & Biomimetics*, Vol. 11, No. 3, pp. 036009, 2016.

- Chapter 5

  S. B. Behbahani, X. Tan, "Design and dynamic modeling of variable stiffness fin for robotic fish using electrorheological fluid," Under preparation, 2016.

TABLE OF CONTENTS

LIST OF TABLES

LIST OF FIGURES

Chapter 1

INTRODUCTION

How fish swim, their remarkable behaviors, and their unique swimming patterns have long intrigued biologists and engineers looking for clues to understand and imitate real fish [1–5]. Scientists and engineers have been motivated by fish to create a class of autonomous underwater vehicles called robotic fish. Different fish swimming modes and characteristics are applied to the design of these biomimetic robotic fish, with the virtues of being maneuverable, efficient, and lifelike [6–9]. There are complex interactions between a fish body, fins, and surrounding fluid, which makes the robotic fish design, development, and control challenging. Improved efficiency, maneuverability, and stealth are some of the potential advantages of robotic fish over traditional propeller-driven underwater vehicles [10–12]. Among their many applications, robotic fish can provide an underwater platform for aquatic environmental monitoring [13, 14], as well as serving as a tool for studying the behaviors of live fish through robot-animal interactions [15].

In this chapter, the motivation behind this study is described in Section 1.1. A review of the state of the art in robotic fish research, especially research involving flexible fins, is given in Section 1.2. The objectives of this study are discussed in Section 1.3. The contributions of this work and the structure of this dissertation are explained in Section 1.4 and 1.5, respectively. The author's publications during the course of Ph.D. studies are listed in Section 1.6.

1.1 Motivation

Biologists and engineers study fish swimming patterns to understand fish locomotion enabled by body and fin movements [16,17]. Numerous designs for robotic fish have been reported in the literature [18], with different actuation mechanisms and levels of system complexity [19–26]. Robotic fish can generate thrust using a tail (caudal) fin [27–29], paired pectoral fins [30–32], or blending both movements [33]. Based on the observations from nature, different kinds of actuators have been suggested to increase efficiency and maneuverability of a robotic fish. A typical strategy for actuating a robotic fish is to use motors, which entails single/multiple joints and rigid links for each tail fin or pectoral fins [20, 27, 34–36]. An alternative approach to fin actuation is the use of smart materials [23, 37–40]. Various studies have indicated that the shape and elasticity of the fish fins play significant roles in the hydrodynamic performance of a fish [11, 41]. From the biological point of view, a fish changes its flexural stiffness to perform different tasks, such as increasing swimming speed [42, 43].

The goal of this work is not just the development of a fish-like robot since it is hard to pursue this goal even with the most advanced technologies, due to the complexity of real fish and its complicated motion. Instead, we study the effect of flexibility of the fins and joints on the performance of robotic fish.

1.2 Literature Review

There is flourishing literature available on design and modeling of robotic fish. Besides mimicking live fish locomotion, biomimetic robotic fish allows researchers to study various fin designs and kinematics that would result in higher levels of performance in speed, maneuverability, stability and efficiency.

For the majority of this study, we focus on the periodic motion generated by paired pectoral fins for robotic fish. Although this mode of swimming is proven to be less efficient at higher speeds, it provides remarkable maneuvering and efficient swimming at lower swimming speeds. There is a large body of work conducted on pectoral fin morphology, kinematics, and hydrodynamics, both analytically [44–46] and computationally using computational fluid dynamics (CFD) methods [47–49] to obtain the forces and torques produced by these fins. Webb [50, 51] and Blake [52, 53] modeled the pectoral fin propulsion and motion of a live fish, providing insight into the computations of hydrodynamic forces involved in pectoral fin actuation. There are several studies on robotic fish with pectoral fins, most of which, however, have considered only rigid pectoral fins with one or more degrees of freedom, each controlled by a separate motor [32, 34, 35, 44, 54–60]. Some of these robotic fish are shown in Fig. 1.1.

Several groups have analyzed the case of flexible pectoral fins in robotic fish. Lauder *et al.* [30, 61] explored the hydrodynamics associated with pectoral fins using a self-propelled pectoral fin with bi-laminar fin rays, both experimentally and with Computational Fluid Dynamics (CFD) simulation. This pectoral fin is shown in Fig. 1.2. Kato *et al.* [62] designed two different types of elastic pectoral fins: An active pneumatic actuator pectoral fin, shown in Fig. 1.3(a), and a passive flexible fin, shown in Fig. 1.3(b). They conducted experiments to estimate the propulsive forces and used Finite Element Method (FEM) to analyze the behavior of these pectoral fins. Deng *et al.* [27, 63] modeled a robotic fish with two pectoral fins and a caudal fin, and used it to design controllers for robotic fish. However, the flexibility of the pectoral fins in their experimental prototype was not included in their model. The design of their robotic fish is shown in Fig. 1.4. With CFD simulation, Shoele *et al.* [64] numerically examined the fluid-structure interaction and force generation by pectoral fins of a fish during labriform swimming mode. Palmisano *et al.* [32] studied a pectoral fin with soft rays in a flapping motion and used CFD analysis for optimal fin

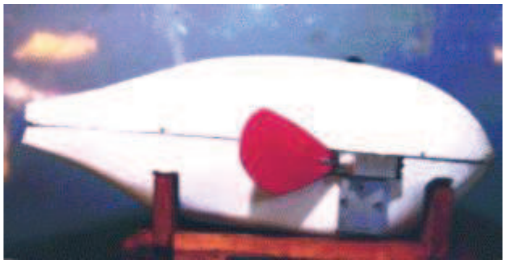

(a) Bass II [36]

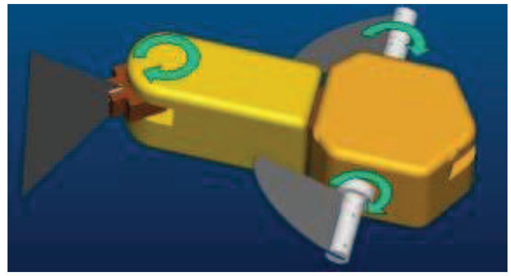

(b) Boxybot [34]

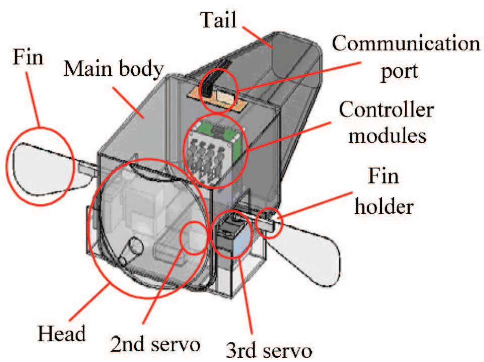

(c) Labriform swimming robotic fish [35]

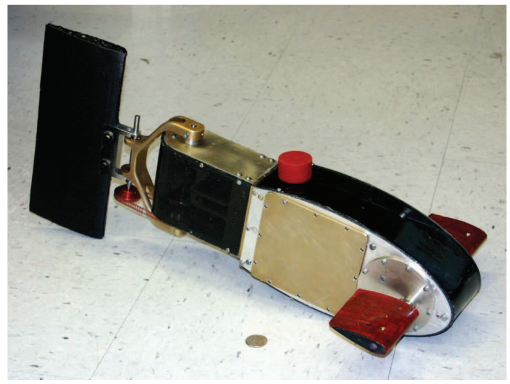

(d) University of Washington's robotic fish [44]

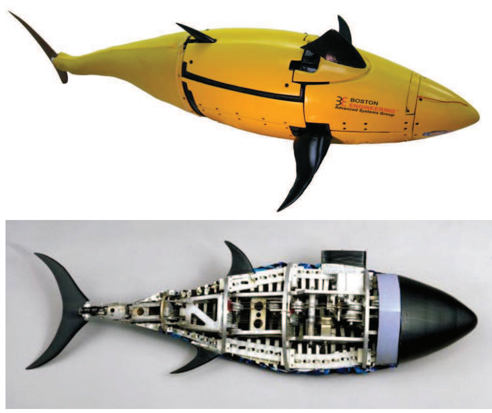

(e) Ghostswimmer [60]

Figure 1.1: Examples of reported robotic fish prototypes with paired pectoral fins.

design.

In summary, the paired pectoral fin swimming that provides drag and lift, can be mimicked under complicated motor control schemes [65, 66]. While flexibility is an important characteristic of pectoral fins for live fish and is expected to influence the hydrodynamics of robotic fish significantly, relevant studies have mostly focused on experimental or CFD exploration of this matter

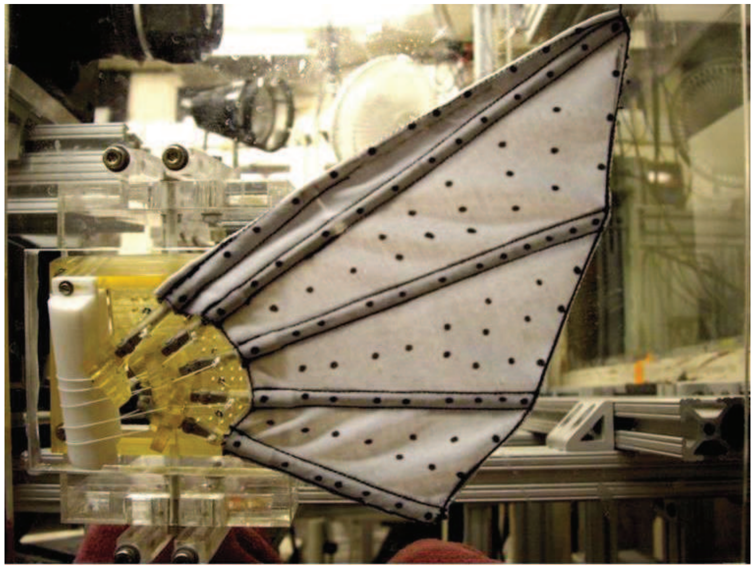

Figure 1.2: A flexible pectoral fin, where the individual tendons permit actuation of each fin ray [61].

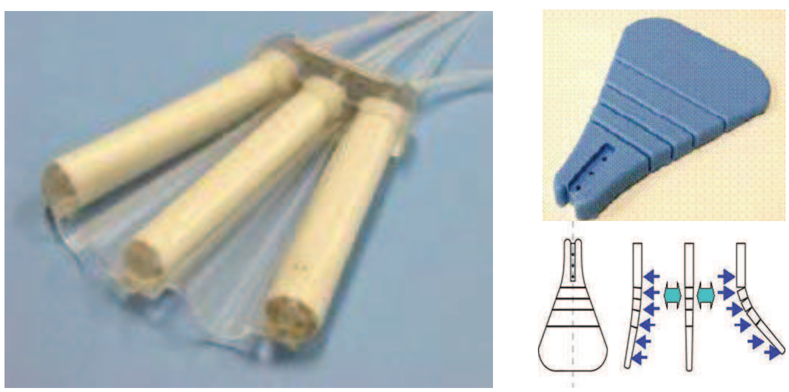

(a) (b)

Figure 1.3: Elastic pectoral fin actuators for biomimetic underwater vehicles [62]: (a) Active pneumatic actuator pectoral fin, and (b) passive flexible fin.

and the systematic analysis of the role of flexibility in pectoral fins and its impact on robotic fish performance has been limited.

In addition to flexible fins, the stiffness of the fin should ideally change with the operating condition to improve the performance of the robotic fish [42,43]. Namely, the fins should be stiffer when the oscillating frequency increases, to maximize the amount of thrust. More recently, limited studies have been conducted to address this issue. Ziegler *et al.* [67] developed a free-swimming

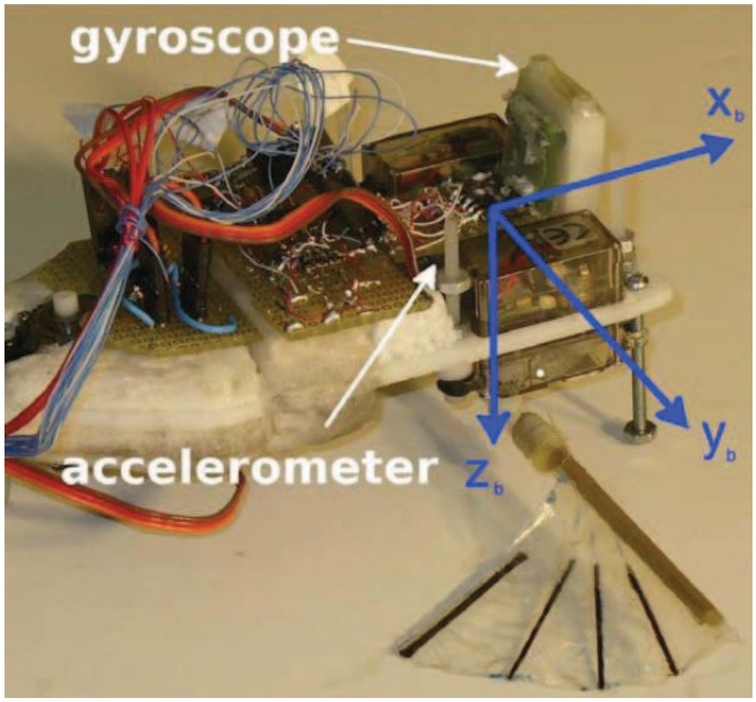

Figure 1.4: Robotic fish with flexible pectoral fins [27, 63].

robotic fish, which was actuated by a tail fin capable of varying its elasticity. The tail fin was actuated by a primary motor, and two small servos were used to vary the elasticity of the fin. This fin consisted of two main foils. Additional foils of various thickness and material could be inserted into the main foil, utilizing the small servos. This results in change of the stiffness of the flexible tail. The schematic of their proposed design is shown in Fig. 1.5(a). Park *et al.* [68] developed a fin with a variable-stiffness flapping mechanism, which was realized by compressing a compliant material to increase the stiffness. Their design was based on the endoskeleton structure, which used a simple mechanism. When the compliant material was compressed, the stiffness increased. Their design consisted of six rigid plates, which were used as the backbone of the robotic fish. The plates had specific intervals between them. Two tendons were used for driving the tail and two other tendons were used to change its stiffness. Basically, when the tendons were pulled, the variable-stiffness structure was compressed, which would result in an increase in axial stiffness, and when the tendons were released, the axial stiffness would decrease. This structure is shown in detail in Fig. 1.5(b). Nakabayashi *et al.* [69] developed a robotic fish with a variable-stiffness mechanism using a variable-effective-length spring. The bending stiffness of the tail fin could vary dynamically in this work, which worked by altering the length of a rigid plate using a motor. This would result in changing the effective-length of the spring, and thus change of stiffness. However, this design needs enough space to actually adjust the length of the spring. The structure for the proposed variable stiffness mechanism is shown in Fig. 1.5(c). In all the works mentioned above, the stiffness was controlled by servos, and consequently, the robots were relatively bulky due to the need for additional servos to perform the job.

1.3 Research Objectives

This dissertation addresses four issues of increasing complexity. (1) *How the flexibility of pectoral fins affects the swimming performance and mechanical efficiency of the robot?* An analytical study of the effect of flexibility of the fins on the performance of robotic fish is a vital contribution to the robotic society. (2) *How can we achieve more efficient swimming by introducing flexible passive joints, and reducing the complexity of the robot?* An alternative approach that reduces the effective area of the pectoral fin in the recovery stroke under symmetrical actuation can improve the performance of the robotic fish. (3) *How can we utilize the flexible passive joint idea and achieve a more complex fin motion, mimicking drag-based labriform swimming of live fish?* Real fish rarely exclusively use motion of pectoral fins; instead, they use a combination of different motions to move forward. (4) *Can we achieve a design that actively changes the stiffness of the robotic fish fins based on the operation conditions, and yet is quick and compact?* It is important to modify the stiffness of the robotic fish fins based on the performance states. This change needs to be applied instantly to the fin, base on the operation regime the robotic fish is in, to be most effective.

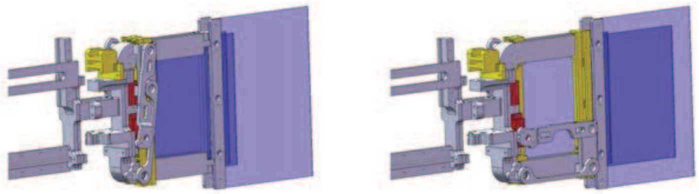

(a) Mechanism for stiffness change in tail fin [67]

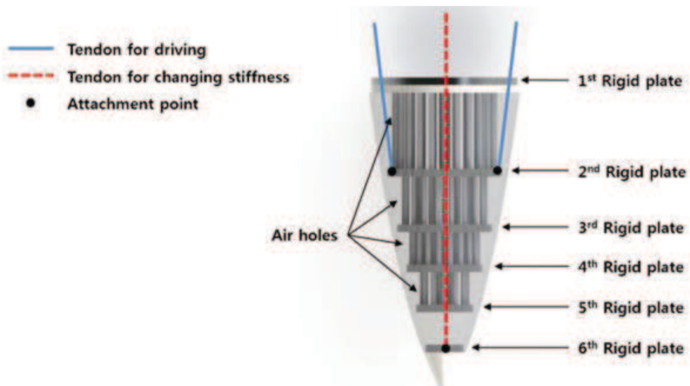

(b) Design of driving part with variable-stiffness structure and tendons [68]

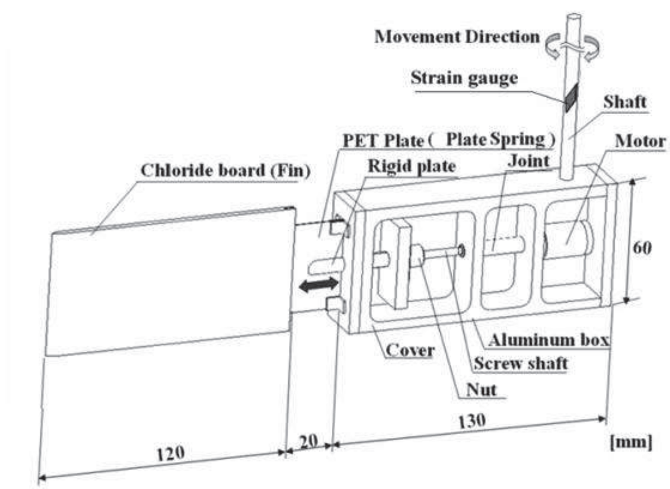

(c) Structure of fin with variable effective length spring [69]

Figure 1.5: Examples of reported designs for tunable stiffness fin.

1.4 Overview of Contributions

The goal of this research is to investigate the fundamentals of fish-like propulsion using flexible components for performance enhancement in aquatic robotics. To this end, the contributions of this research are further summarized as follows:

First, we explore the impact of the flexibility of robotic fish pectoral fins on the robot locomotion performance and mechanical efficiency. A dynamic model for the robotic fish is presented, where the flexible fin is modeled as multiple rigid elements connected via torsional springs and dampers. Blade element theory is used to capture the hydrodynamic force on the flexible fin. The model is validated with experimental results obtained on a robotic fish prototype, equipped with 3D-printed fins of different flexibility. The model is then used to analyze the impacts of fin flexibility and power/recovery stroke speed ratio on the robot swimming speed and mechanical efficiency.

Second, we introduce the design of a novel flexible passive joint that connects the servomotor arm to the pectoral fin, to overcome the difficulties that arise with a traditional rigid joint, which has slower recovery stroke speed and faster power stroke speed in order to generate a net thrust. A dynamic model is developed for the joint and for a robotic fish equipped with such joints. The design and the model are evaluated with extensive experimental results. Motivated by the need for design optimization, the model is further utilized to investigate the influence of the joint length and stiffness on the robot locomotion performance and efficiency.

Third, a novel flexible joint is proposed for robotic fish pectoral fins, which enables a swimming behavior emulating the fin motions of many aquatic animals. In particular, the pectoral fin operates primarily in the rowing mode, while undergoing passive feathering during the recovery stroke to reduce hydrodynamic drag on the fin. The latter enables effective locomotion even with symmetric base actuation during power and recovery strokes. A dynamic model is developed to facilitate the understanding and design of the joint, where blade element theory is adopted to calculate the hydrodynamic forces on the pectoral fins, and the joint is modeled as a paired torsion spring and damper. Experimental results on a robotic fish prototype are presented to illustrate the effectiveness of the joint mechanism, validate the proposed model, and indicate the utility of the proposed model for the optimal design of joint depth and stiffness in achieving the trade-off between swimming speed and mechanical efficiency.

Finally, we study the design, prototyping, and dynamic modeling of a tunable-stiffness fin for robotic fish, using an electrorheological (ER) fluid, which enables adapting the flexural stiffness of the compliant fin. A multi-layer composite fin with an ER fluid core is prototyped and utilized to investigate the influence of electric field on its performance. Lighthill's large amplitude elongated-body theory is adopted to evaluate the hydrodynamic forces on the fin, and Hamilton's principle is used to derive the dynamic equations of motion of the flexible composite caudal fin. The dynamic equations are then discretized using the finite element method, to obtain an approximate numerical solution. Experiments are conducted on the prototyped flexible ER-fluid filled beam to identify some parameters, validate the proposed dynamic model, and assess the efficacy of the proposed stiffness-tuning approach.

1.5 Dissertation Layout

This dissertation consists of 6 chapters and is organized as follows: In Chapter 2, a complete dynamic model of a robotic fish actuated by a pair of flexible pectoral fins is discussed. A detailed explanation of the various forces acting on the robotic fish and the full Newton-Euler equations are derived, where blade element theory is used to evaluate the hydrodynamic forces on the oscillating flexible pectoral fins. The swimming performance and mechanical efficiency of flexible pectoral fins, connected to actuator shafts via rigid links, are studied, where it is found that flexible fins demonstrate advantages over rigid fins in speed and efficiency at relatively low fin-beat frequencies, while the rigid fins outperform the flexible fins at higher frequencies. The presented model offers a promising tool for the design of fin flexibility and swimming gait, to achieve speed and efficiency objectives for the robotic fish. Chapter 3 provides detailed information about the novel flexible rowing joint mechanism. The joint design, dynamic modeling and experimental results are presented in this chapter. The influence of the joint length and stiffness on the robot locomotion performance and efficiency are investigated. In Chapter 4, we focus on another flexible passive joint, called flexible feathering joint. This joint enables the robotic fish to perform the drag-based labriform swimming without adding additional servo motors to the fins. The joint design, dynamic modeling, and experimental results of a robotic fish utilizing this joint are presented in this chapter. The effect of joint depth and stiffness in achieving the trade-off between swimming speed and mechanical efficiency is studied as well. Chapter 5 focuses on the design, prototyping, and dynamic modeling of the tunable-stiffness fin for robotic fish. The tunable stiffness can be used in optimizing the robotic fish speed or maneuverability in different operating regimes. Fins with tunable stiffness are prototyped, and free oscillation and base-excited oscillation behaviors of the fins are measured underwater when different electric fields are applied for the ER fluid, which are subsequently used to develop a dynamic model for the stiffness-tunable fins. Finally, the last chapter summarizes the most important aspects and results achieved in this work. Possible future developments are outlined as well.

1.6 Publications

1.6.1 Journal Articles

1. **S. B. Behbahani**, X. Tan, "Design and Modeling of Flexible Passive Rowing Joints for Robotic Fish Pectoral Fins," *IEEE Transactions on Robotics*, Vol. 32, No. 5, pp. 1119-1132, 2016.

2. **S. B. Behbahani**, X. Tan, “Bio-inspired Flexible Joints with Passive Feathering for Robotic Fish Pectoral Fins,” *Bioinspiration & Biomimetics*, Vol. 11, No. 3, pp. 036009, 2016, **[Featured article]**.

3. **S. B. Behbahani**, X. Tan, “Role of Pectoral Fin Flexibility in Robotic Fish Performance,” *Journal of Nonlinear Science*, Under review, 2016.

4. **S. B. Behbahani**, X. Tan, “Design and dynamic modeling of variable stiffness fin for robotic fish using electrorheological fluid,” Under preparation, 2016.

1.6.2 Conference Proceedings

1. **S. B. Behbahani**, X. Tan, “Dynamic Modeling of Robotic Fish Caudal Fin with Electrorheological Fluid-Enabled Tunable stiffness,” *Proceedings of the ASME Dynamic Systems and Control Conference (DSCC)*, Columbus, OH, USA, Oct. 2015, pp. V003T49A006 (9 pages).

2. **S. B. Behbahani**, X. Tan, “Design and Dynamic modeling of a Flexible Feathering Joint for Robotic Fish Pectoral Fins,” [Invited], *Proceedings of the ASME Dynamic Systems and Control Conference (DSCC)*, San Antonio, TX, USA, Oct. 2014, pp. V001T05A005 (9 pages), **[Finalist for Best Student Paper Award]**.

3. **S. B. Behbahani**, X. Tan, “A Flexible Passive Joint for Robotic Fish Pectoral Fins: Design, Dynamic Modeling, and Experimental Results,” *Proceedings of the IEEE/RSJ International Conference on Intelligent Robots and Systems (IROS)*, Chicago, IL, USA, Sept. 2014, pp. 2832-2838.

4. **S. B. Behbahani**, J. Wang, X. Tan, “A dynamic model for robotic fish with flexible pectoral fins,” *Proceedings of the IEEE/ASME International Conference on Advanced Intelligent Mechatronics (AIM)*, Wollongong, Australia, Jul. 2013, pp. 1552-1557.

Chapter 2

Role of Pectoral Fin Flexibility in Robotic Fish Performance

2.1 Introduction

Modeling the robotic fish dynamics is often critical for the design, control, and understanding of robotic fish behavior, and it has received extensive attention in the literature [20, 28, 39, 45, 70–72]. The most challenging step in dynamically modeling robotic fish is capturing the interactions between the body/fins and the fluid and calculating the resulting force and moment exerted on the body. Computational Fluid Dynamics (CFD) modeling [47–49, 73] is capable of describing such interactions with high fidelity and offering physical insight, but its computational cost often makes it infeasible for designing and control purposes. Several alternatives are available. For example, quasi-steady lift and drag models from airfoil theory can be applied to the body and fin surfaces of underwater robots [27, 44, 74–76]. One could also assume perfect fluids (irrotational potential flow) and exploit the symmetry to obtain a finite-dimensional model for the fluid-structure interactions [45, 77]. Effects of vorticity can be accommodated by assuming, for example, vortices periodically shed from the tail fin [46, 78].

In this chapter we are focused on paired pectoral fin locomotion of a robotic fish. Although the caudal fin is the primary appendage used for propulsion in robotic fish [20, 23, 28, 34], pectoral fins play a vital role in maneuvering and stability of live fish while providing or assisting propulsion [79, 80]. Kinematics and hydrodynamics of live fish pectoral fins have been studied be several researchers [50–53]. A number of investigations have been conducted on rigid pectoral fins with one or more degrees of freedom, to study their effect on robotic fish swimming [27, 35, 36, 44, 55, 81, 82]. Recently, studies have been pursued on flexible pectoral fins [21, 30, 32, 61–64, 83], and pectoral fins with flexible joints [84–87], to mimic live fish behavior more closely. While the flexibility of pectoral fins for live fish and robotic fish is appreciated and has been explored with both experimental [30, 61] and CFD [49] methods, systematic analysis of the role of pectoral fin flexibility in robotic fish performance has been limited.

The goal of this chapter is to develop a systematic, computation-efficient framework for analyzing how the flexibility of pectoral fins affects the swimming performance and mechanical efficiency of the robot. While pectoral fin motions can generally be classified into three modes based on the axis of rotation, rowing, feathering, and flapping, we focus on the rowing motion since it can be utilized for a number of in-plane locomotion and maneuvering tasks, such as forward swimming, sideway swimming, and turning. A dynamic model for the robotic fish is first proposed. We use Newton-Euler equations to model the rigid body dynamics of the robot. The flexible fins are approximated as multiple rigid elements, connected via torsional springs and dampers. Such an approach has been proven effective and computationally efficient in capturing large deformation in flexible caudal fins [29]. Blade element theory is adopted to evaluate the hydrodynamic forces on the fin elements. The proposed dynamic model is verified through experiments on a free-swimming robotic fish prototype equipped with pectoral fins. The fins are 3D-printed with different stiffness levels, ranging from very flexible to rigid.

The dynamic model is used to analyze the impact of fin flexibility on swimming speed behavior at different fin-beat frequencies. It is found that, while the robot with rigid fins achieves a linearly increasing speed with the fin-beat frequency, there is an optimal frequency in the case of a flexible fin at which the speed is maximized. Furthermore, fins with moderate flexibility outperform the rigid fins on the speed performance for a large range of operating frequencies. The impact of speed ratio ζ between the power stroke and the recovery stroke on the swimming behavior is also studied for different fins. Finally, the influences of fin flexibility and ζ on the mechanical efficiency of the robot are examined. The study reveals interesting trade-offs between the different objectives (speed and efficiency) and supports the use of the proposed model as a promising tool for fin flexibility and gait design.

The remainder of this chapter is organized as follows. Section 2.2 reviews the dynamics of the robotic fish body. Section 2.3 presents the dynamic model for the flexible pectoral fins. The kinematics of the flexible pectoral fins adopted in this work is presented in Section 2.4, while the method for mechanical efficiency calculation is discussed in Section 2.5. In Section 2.6 we present the robotic fish prototype, the pectoral fin fabrication method, the experimental setup, and the methods for model parameter identification. Section 2.7 is devoted to results. Finally, concluding remarks and future work directions are discussed in Section 2.8.

2.2 Dynamics of the Robotic Fish Body

The robotic fish under study contains two subsystems, the flexible pectoral fins, for which the dynamics are covered in Section 2.3, and the rigid body. The robotic fish prototype used in this study does have a caudal fin, but the consideration of caudal fin hydrodynamics is outside the scope of this work. To study the motion of the robot, we include the rigid body dynamics based on Kirchhoff's equations of motion in an inviscid fluid [28, 88], with the added mass effect incorporated.

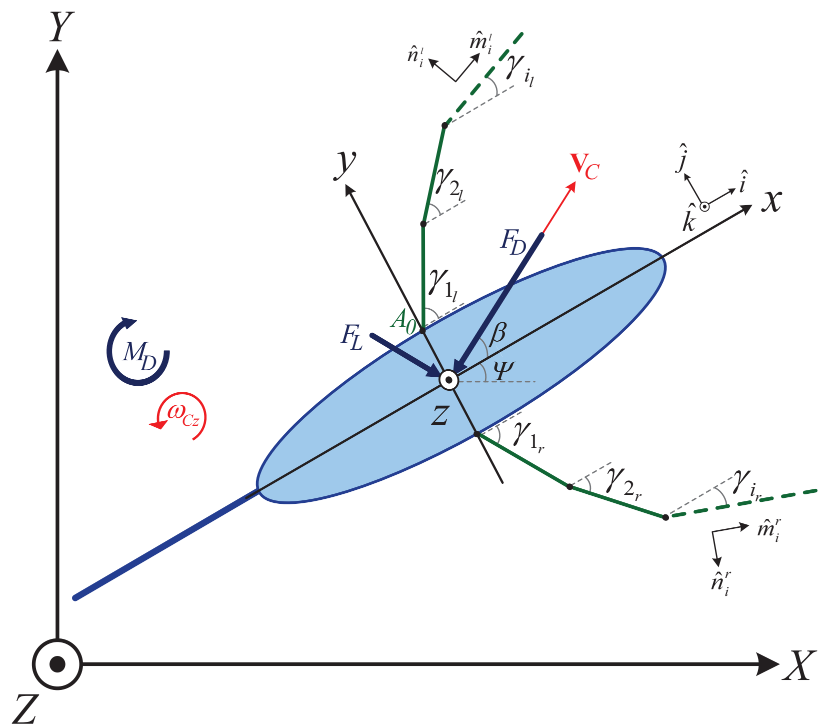

Figure 2.1: Top view of the robotic fish actuated by flexible pectoral fins and restricted to planar motion.

2.2.1 Rigid Body Dynamics

Fig. 2.1 illustrates a robotic fish, restricted to the planar motion, where $[X, Y, Z]^T$ denotes the global coordinates, and $[x, y, z]^T$ with unit vectors $[\hat{i}, \hat{j}, \hat{k}]$ indicates the body-fixed coordinates, attached to the center of mass of the robotic fish body. Each pectoral fin is modeled as multiple, connected, rigid elements, and $\hat{m}_i$ and $\hat{n}_i$ denote the unit vectors parallel to and perpendicular to the ith element of the pectoral fin, respectively, where superscripts r and l indicate the right and the left fin, respectively. The robotic fish body and the flexible pectoral fins are considered to be neutrally buoyant, with center of gravity and geometry coinciding. The simplified equations of the robotic fish body in the body-fixed coordinates are represented as [29, 63, 87]

$$(m_b - X_{\dot{V}_{C_x}})\dot{V}_{C_x} = (m_b - Y_{\dot{V}_{C_y}})V_{C_y}\omega_{C_z} + F_x, \tag{2.1}$$

$$(m_b - Y_{\dot{V}_{C_Y}})\dot{V}_{C_y} = -(m_b - X_{\dot{V}_{C_x}})V_{C_x}\omega_{C_z} + F_y, \tag{2.2}$$

$$(I_z - N_{\dot{\omega}_{C_z}})\dot{\omega}_{C_z} = M_z, \tag{2.3}$$

where m_b is the mass of the robotic fish body, I_z is the robot inertia about the z-axis, $X_{\dot{V}_{C_x}}$, $Y_{\dot{V}_{C_y}}$, and $N_{\dot{\omega}_{C_z}}$ are the hydrodynamic derivatives that represent the effect of the added mass/inertia on the rigid body [88]. V_{C_x}, V_{C_y}, and ω_{C_z} are the surge, sway, and yaw velocities, respectively. The variables F_x, F_y and M_z denote the external hydrodynamic forces and moment exerted on the fish body, which are described as

$$F_x = F_{h_x} - F_D \cos\,\beta + F_L \sin\,\beta, \tag{2.4}$$

$$F_y = F_{h_y} - F_D \sin\,\beta - F_L \cos\,\beta, \tag{2.5}$$

$$M_z = M_{h_z} + M_D, \tag{2.6}$$

where F_{h_x}, F_{h_y} and M_{h_z} are the hydrodynamic forces and moment transmitted to the fish body by the pectoral fins, the details of which are provided in Section 2.3. As depicted in Fig. 2.1, F_D, F_L, and M_D are the body drag, lift, and moment, respectively. These forces and moment are expressed as [28, 29, 44]

$$F_D = \frac{1}{2}\rho|V_C|^2 S_A C_D, \tag{2.7}$$

$$F_L = \frac{1}{2}\rho|V_C|^2 S_A C_L \beta, \tag{2.8}$$

$$M_D = -C_M \omega_{C_z}^2 \,\mathrm{sgn}(\omega_{C_z}), \tag{2.9}$$

where $|V_C|$ is the linear velocity magnitude of the robotic fish body, $|V_C| = \sqrt{V_{C_x}^2 + V_{C_y}^2}$, ρ is the mass density of water, S_A is the wetted area of the body, C_D, C_L and C_M are the dimensionless drag, lift, and damping moment coefficients, respectively, β is the angle of attack of the body, and $\mathrm{sgn}(.)$ is the signum function.

Finally, the kinematics of the robotic fish are described as [29]

$$\dot{X} = V_{C_x} \cos \psi - V_{C_y} \sin \psi, \tag{2.10}$$

$$\dot{Y} = V_{C_y} \cos \psi + V_{C_x} \sin \psi, \tag{2.11}$$

$$\dot{\psi} = \omega_{C_z}, \tag{2.12}$$

where ψ denotes the angle between the x-axis and the X-axis.

2.3 Dynamics of Flexible Rowing Pectoral Fins

This section focuses on calculating the hydrodynamic forces on the flexible pectoral fin and determining its dynamics using blade element theory [5], by dividing the fin span into multiple rigid elements. The rowing motion of the pectoral fin has been classified as a "drag-based" swimming mechanism, where the drag element of fluid dynamics generates the thrust [89, 90]. The pectoral fin is considered to be rectangular with span length of S and chord length of C. We consider a coordinate system with unit vectors $\hat{m}_i$ and $\hat{n}_i$ for the pectoral fin; see Fig. 2.1. The relationship between these unit vectors and the robotic fish body-fixed coordinates is given by

$$\hat{m}_i = \cos \gamma_i \hat{i} + \sin \gamma_i \hat{j}, \tag{2.13}$$

$$\hat{n}_i = -\sin \gamma_i \hat{i} + \cos \gamma_i \hat{j}, \tag{2.14}$$

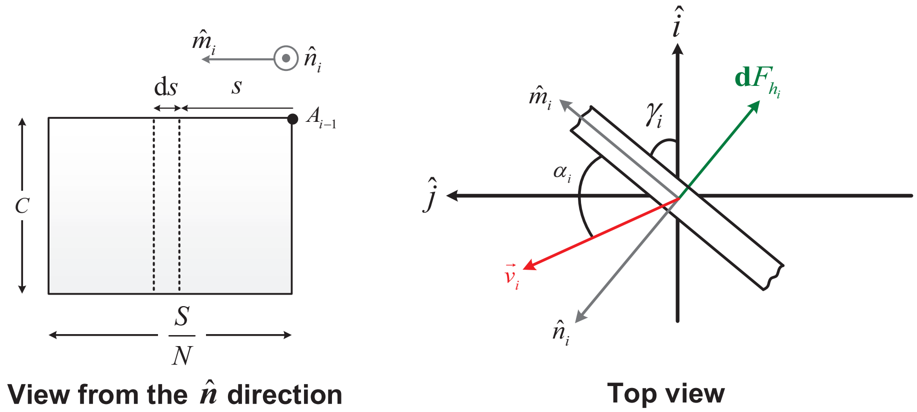

Figure 2.2: Top view of ith element of the flexible fin and its parameters and variables.

where γ_i is the angle between $\hat{m}_i$ and $\hat{i}$; see Fig. 2.1 for illustration. We use the left pectoral fin to illustrate the calculations. However, it is straightforward to extend the calculations to the right pectoral fin. Fig. 2.2 provides a visualization of the parameters and variables of a flexible fin element.

We divide the flexible fin into N rigid elements with an equal length of $l = \frac{S}{N}$, where each segment is connected to its neighbors via a pair of torsional spring and damper. The constants of the spring and damper can be derived from the properties of the flexible material. The spring constant K_S is evaluated as [91]

$$K_S = \frac{ECh^3}{12l}, \tag{2.15}$$

where h is the beam thickness, and E is the Young's modulus of the flexible material used for the pectoral fin. The damper coefficient K_D can be evaluated as $K_D = \kappa K_S$, where κ is a proportional constant. Fig. 2.3 illustrates the forces on the ith element of the flexible fin. The angle γ_1 is dictated by the pectoral fin actuator, and we need to find the angles γ_2 to γ_N, to know the trajectory of the flexible fin at each instant of time, which, subsequently, will allow one to evaluate the hydrodynamic force generated by the fin. In the following calculations we assume an anchored robotic fish body. This simplifying assumption is often adopted in the literature for similar prob-

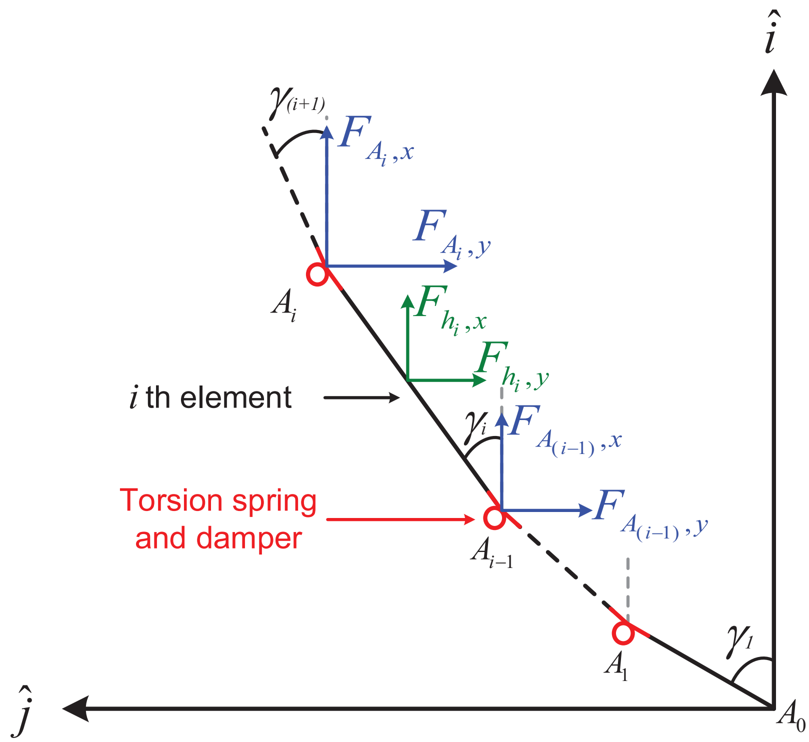

Figure 2.3: Illustration of forces on the ith element of the flexible fin.

lems [2,19,29], and the resulting error is typically negligible considering the much greater pectoral fin velocity compared to the robotic fish body speed.

The position of each point s on the ith element (see the definition of s in Fig. 2.2) at time t on the ith element can be described as

$$r_i(s,t) = \sum_{k=1}^{i-1} l \cdot \hat{m}_k + s \cdot \hat{m}_i. \tag{2.16}$$

The corresponding velocity at the point s is

$$v_i(s,t) = \left\{ \sum_{k=1}^{i-1} l\dot{\gamma}_k \cos(\gamma_i - \gamma_k) + s\dot{\gamma}_i \right\} \hat{n}_i + \left\{ \sum_{k=1}^{i-1} l\dot{\gamma}_k \sin(\gamma_i - \gamma_k) \right\} \hat{m}_i, \tag{2.17}$$

where $\dot{\gamma}_k$ indicates the time derivative of γ_k. Respectively, the corresponding acceleration at the point s is evaluated as

$$\begin{aligned} a_i(s,t) = &\Big\{ \sum_{k=1}^{i-1} \big[l\ddot{\gamma}_k \cos(\gamma_i - \gamma_k) + l\dot{\gamma}_k^2 \sin(\gamma_i - \gamma_k) \big] + s\ddot{\gamma}_i \Big\} \hat{n}_i \\ &+ \Big\{ \sum_{k=1}^{i-1} \big[l\ddot{\gamma}_k \sin(\gamma_i - \gamma_k) - l\dot{\gamma}_k^2 \cos(\gamma_i - \gamma_k) \big] - s\dot{\gamma}_i^2 \Big\} \hat{m}_i, \end{aligned} \tag{2.18}$$

where $\ddot{\gamma}_k$ indicates the second time derivative of γ_k.

2.3.1 Force Calculations for Element i

The hydrodynamic force on each element of the flexible fin is evaluated based on the blade element theory [5] as follows

$$\mathrm{d}F_{h_i}(s,t) = -\frac{1}{2} C_n\big(\alpha_i(s,t)\big) \rho C |v_i(s,t)|^2 \mathrm{d}s \quad \hat{e}_{v_i}, \tag{2.19}$$

where $\hat{e}_{v_i}$ is a unit vector in the direction of the velocity of the ith element. C_n is the force coefficient, which depends on the angle of attack at each point, $\alpha_i(s,t)$, and has a form of

$$C_n(\alpha_i) = \lambda \sin \alpha_i, \tag{2.20}$$

where the parameter λ is evaluated empirically through experiments. Note that Eq. (2.19) captures both normal and span-wise components of the hydrodynamic force. The angle of attack at each point, $\alpha_i(s,t)$, is defined via

$$\tan \alpha_i(s,t) = \frac{< v_i(s,t), \hat{n}_i >}{< v_i(s,t), \hat{m}_i >}, \tag{2.21}$$

where $< \cdot, \cdot >$ denotes the inner product.

The total hydrodynamic force acting on the ith element is defined by integrating Eq. (2.19) along the length of the element

$$F_{h_i}(t) = \int_0^l \mathrm{d}F_{h_i}(s,t) \ . \tag{2.22}$$

The interaction between two consecutive elements is captured via force balance on each element:

$$F_{h_i} + F_{A_{i-1}} - F_{A_i} = m_i a_i, \tag{2.23}$$

where F_{A_i} is the force applied by element i on element $i+1$, $F_{A_{i-1}}$ is the force applied by element $i-1$ on element i, m_i is the effective mass of the ith element (which contains the mass and the added mass of element i, where the added mass is calculated based on a rigid plate moving in the water), and a_i denotes the acceleration of the midpoint of the ith element, which can be evaluated using Eq. (2.18) with $s = \frac{l}{2}$. See Fig. 2.3 for illustration of the forces. Note that for the last element, $F_{A_N} = 0$; therefore, Eq. (2.23) can be solved iteratively for F_{A_i}, where $0 \leq i \leq N-1$.

2.3.2 Moment Calculations for Element *i*

The total hydrodynamic moment on the ith element is calculated as

$$M_{h_i} = \int_0^l s\hat{m}_i \times \mathrm{d}F_{h_i}(s,t), \tag{2.24}$$

where $\mathrm{d}F_{h_i}(s,t)$ is as expressed in Eq. (2.19). The total moment relative to point A_{i-1} for element i is evaluated as

$$M_i = M_{h_i} + l \times F_{A_i} + M_{i+1} + M_{(S+D)_i} = I_i \ddot{\gamma}_i, \tag{2.25}$$

where $\times$ denotes the cross product, I_i represents the effective inertia of the ith element, and $M_{(S+D)_i}$, the moment induced by the torsional spring and damper at A_{i-1}, is evaluated as

$$M_{(S+D)_i} = -[K_S(\gamma_i - \gamma_{i-1}) + K_D(\dot{\gamma}_i - \dot{\gamma}_{i-1})]\hat{k}, \tag{2.26}$$

where K_S and K_D are the spring and damper coefficients used to model the flexible pectoral fin. Note that for the element N, $M_{N+1} = 0$, which, through the recursion in the first equality in [25], allows the explicit expression of M_i, $2 \leq i \leq N$, in terms of other variables. The second equality in (2.25) thus provides (N-1) nonlinear second-order equations for γ_i, where $2 \leq i \leq N$, which fully describe the dynamics of the N-element pectoral fin.

Eqs. (2.23) and (2.25) are used to find the total force/moment exerted on the robotic fish body:

$$F_{h_x} = < F_{A_0}, \hat{i} >, \tag{2.27}$$

$$F_{h_y} = < F_{A_0}, \hat{j} >, \tag{2.28}$$

$$M_{h_z} = -c_p < F_{A_0}, \hat{i} > -M_1, \tag{2.29}$$

where c_p is the distance between robotic fish center of mass and the base of the flexible fin, F_{A_0} is the total force applied by the flexible pectoral fin to the center of mass of the robotic fish body, and M_1 is the moment applied by the flexible pectoral fin to the center of mass of the robotic fish body. These forces and moments are then plugged into (2.4)-(2.6) to solve the rigid body dynamics of the robotic fish.

2.4 Kinematics of Flexible Rowing Pectoral Fins

The pectoral fins in this study sweep back and forth within the frontal plane. The rowing motion has distinct power and recovery strokes. During the power stroke, the pectoral fin moves backward to produce thrust through induced drag on the pectoral fin surface. On the other hand, during the recovery stroke, the fin moves toward the front of the fish, with minimal loading, to get ready for next fin-beat cycle. The pectoral fin is actuated at different speeds during the power and recovery strokes (faster power stroke) to produce a net thrust. In particular, we define the ratio

$$\zeta = \frac{P}{R} = \frac{\text{Power stroke speed}}{\text{Recovery stroke speed}}. \tag{2.30}$$

For each fin-beat cycle, the pectoral fin base rotates according to

$$\gamma_1(t) = \begin{cases} \frac{\pi}{2} - \gamma_A \cos\left[\pi\left(\frac{\zeta+1}{T_p}\right)t\right], & 0 \le t \le \frac{T_p}{\zeta+1} \\ \frac{\pi}{2} + \gamma_A \cos\left[\pi\left(\frac{\zeta+1}{\zeta T_p}\right)\left(t - \frac{T_p}{\zeta+1}\right)\right], & \frac{T_p}{\zeta+1} < t \le T_p \end{cases} \tag{2.31}$$

where γ_A is the amplitude of fin the actuation and T_P denotes the period of one cycle.

Fig. 2.4 illustrates the pectoral fin kinematics. The visualization of the pectoral fin motion during one fin-beat cycle is shown in Fig. 2.4(a). Note that for $\zeta = 1$, the pectoral fin flaps symmetrically during the power stroke and the recovery stroke, and for $\zeta > 1$, the pectoral fin slows down and spends more time in the recovery phase. Fig. 2.4(b) illustrates the orientation angle γ_1 and the angular velocity $\dot{\gamma}_1$ of the base of the pectoral fin with respect to the x-axis of the robotic fish during one fin-beat cycle. For turning the robotic fish, we just actuate one of the pectoral fins and keep the other fin still.

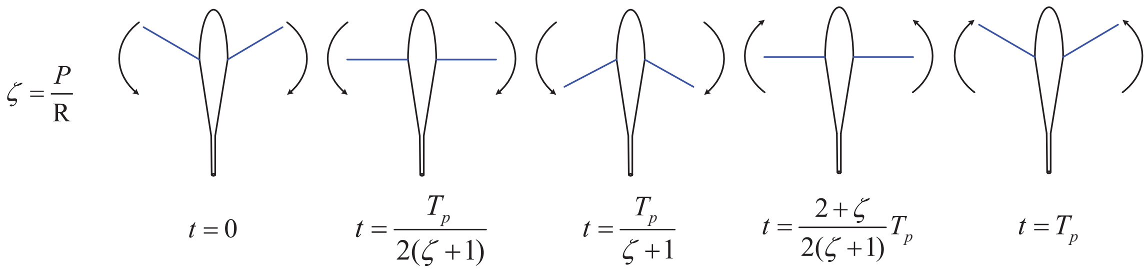

(a)

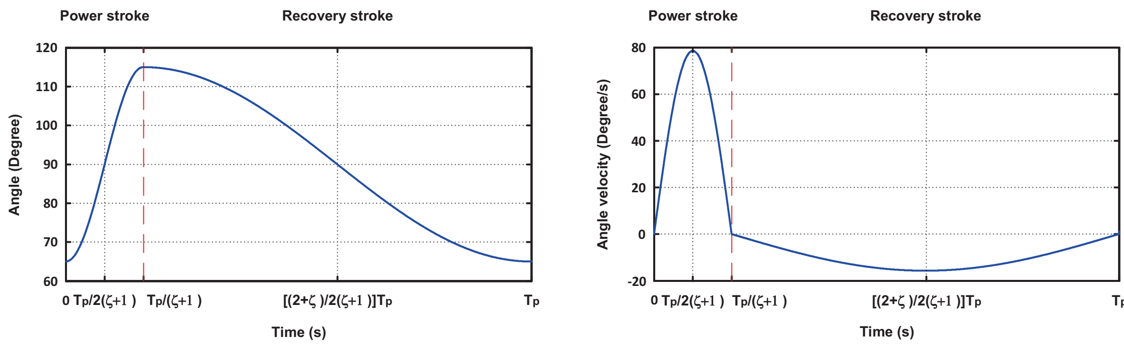

(b)

Figure 2.4: Illustration of the pectoral fin motion during power and recovery strokes: (a) The snapshots at different time instances of one fin-beat cycle, where T_p represents the total time for each cycle; (b) orientation and angular velocity of the base of the pectoral fin with respect to the main axis of the robotic fish, where $\zeta = 5$, $\gamma_A = 50$ deg, and $T_p = 1$ s are used.

2.5 Mechanical Efficiency

Aside from the swimming performance (for example, swimming speed or turning radius), another critical factor about the robotic fish is its mechanical efficiency. We will analyze the efficiency of the robot under different pectoral fin properties using the model presented in Sections 2.3 and 2.4. In particular, it is of interest to investigate the effect of flexibility of the pectoral fins on the mechanical efficiency. During steady-state swimming, the mechanical efficiency of the robot is evaluated as [5, 92, 93]

$$\eta = \frac{W_b}{W_T}, \tag{2.32}$$

where W_b is the useful work needed to move the robotic fish during each fin-beat cycle, and W_T is the total work done by the pectoral fins during the same period. In this study, we do not consider other energy losses, such as the amount of electrical power used by other electronics, or frictional losses in motors and gears. The useful work W_b is determined by

$$W_b = \int_{t_0}^{t_0+T_p} F_{\mathrm{Thrust}}(t) V_{C_x}(t) \mathrm{d}t, \tag{2.33}$$

where t_0 denotes the beginning of the fin-beat cycle, and $F_{\mathrm{Thrust}} = F_{h_x}$ is the total hydrodynamic force produced by the pectoral fin in the x direction, exerted on the robotic fish body. The total work done by the paired pectoral fins, W_T, is obtained via

$$W_T = 2\int_{t_0}^{t_0+T_p} \max\{0, \sum_{i=1}^{N} \int_0^l < \mathrm{d}F_{h_i}(s,t), v_i(s,t) >\} \mathrm{d}t. \tag{2.34}$$

At some instants of time, the mechanical power of the pectoral fins could be negative. However, the servos cannot reclaim this energy from the water. Therefore, we treat the instantaneous power for these cases to be zero, which explains the $\max(0,\cdot)$ operation in (2.34).

2.6 Materials and Methods

2.6.1 Robotic Fish Prototype

A robotic fish prototype, similar to that in [86], was used to test and validate the proposed dynamic model, and to support the performance analysis. This robotic fish included a rigid body, two pectoral fins, and a caudal fin. The rigid body was designed in SoildWorks software and printed in the VeroWhitePlus material from a PolyJet multi-material 3D printer (Objet350 Connex 3D System from Stratasys), and was coated with acrylic paint to minimize water absorption of the 3D-printed material. The body had a length of 15 cm, height of 8 cm, and width of 4.6 cm. Three

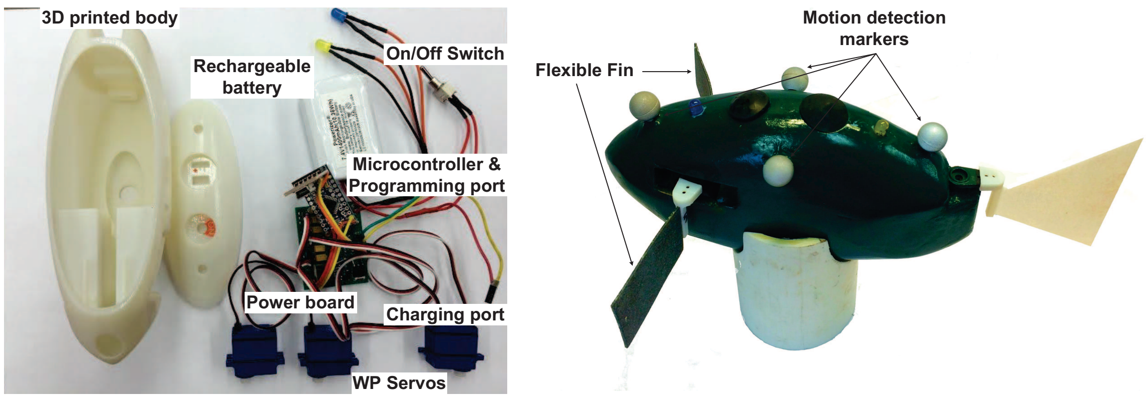

Figure 2.5: 3D-printed robotic fish body and other components of the robot.

waterproof servomotors (Traxxas 2065 Waterproof Sub-Micro Servo from Traxxas) was used to move the pectoral fins and caudal fin individually. The robot was battery-operated, using a Li-ion rechargeable battery (7.4 V, 1400 mAh from Powerizer), and a customized power converter PCB was designed to regulate the voltage to 5 V (through LM2673) and 3.3 V (through LP38690) for the servomotors and the microcontroller, respectively. The robot fin motion was controlled by a microcontroller (Arduino Pro Mini, 3.3 V). A picture of the 3D-printed body, along with all the other components for the robot, is shown in Fig. 2.5.

2.6.2 Pectoral Fin Fabrication

The pectoral fins used in this study were designed to have a composite structure and were 3D-printed. The fins could be easily detached from the fin mounts, to enable testing of the robot with different fins. We followed the approach proposed in [94] for creating the composite fins, the effective stiffness of which can be easily adjusted by changing the thicknesses of different layers. The composite fins were made of two different materials, a rigid plastic material (VeroWhitePlus) and a flexible rubber-like material (TangoBlackPlus). The details of the design are illustrated in Fig. 2.6. The flexibility of the fins was controlled by adjusting the thickness of the VeroWhitePlus

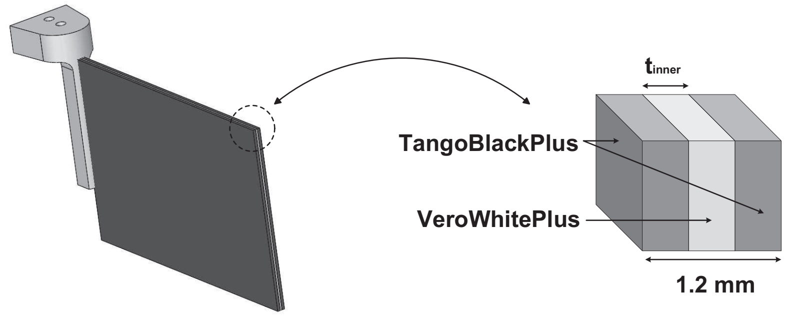

Figure 2.6: Solidworks design of a composite pectoral fin.

Table 2.1: Specifications of pectoral fins with different flexibilities.

Fin name	t_{inner} (mm)	K_S (N·m)	K_D (N·m·s)
F1	1.2	NA	NA
F2	0.3	1.13×10^{-3}	2.59×10^{-4}
F3	0	1.83×10^{-4}	4.37×10^{-5}

inner layer while keeping the total thickness of the fin constant (1.2 mm). Pectoral fins of size 45 mm $\times$ 37.5 mm, with three different stiffness values were fabricated. The specifications of these fins are summarized in Table 2.1. The fins are named F1 – F3 for later reference in this paper.

The 3D-printed pectoral fins were treated with a thin coat of Ultra-Ever Dry omniphobic material (UltraTech International Inc.) to prevent changes of properties that may occur when they come in contact with water. Fig. 2.7 shows an actual 3D-printed pectoral fin, before and after the Ultra-Ever Dry treatment. The application of Ultra-Ever Dry results in a white cast on the treated part.

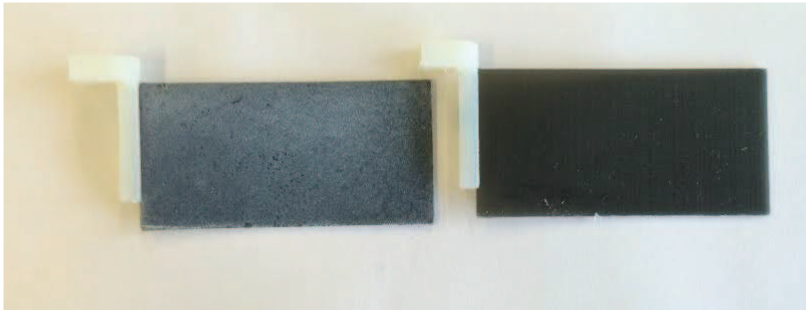

Figure 2.7: An actual 3D-printed pectoral fin. Right: original fin; left: printed fin treated with Ultra-Ever Dry omniphobic material.

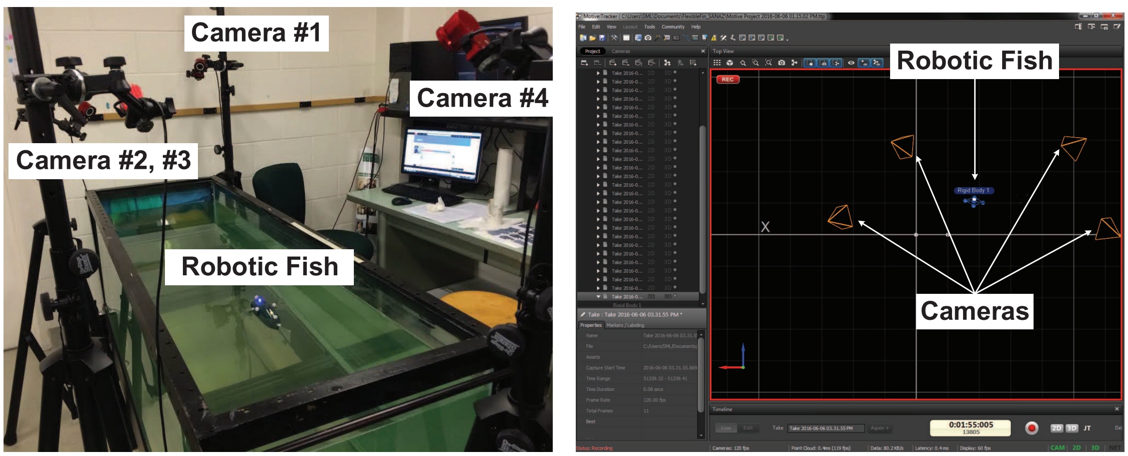

(a) (b)

Figure 2.8: Experimental setup: (a) Actual, (b) output of the Motive software.

2.6.3 Experimental Setup

Experiments were conducted in a 6 ft long, 2 ft wide, and 2 ft deep tank. An Optitrack motion capture system, containing four Flex 13 cameras, each mounted on heavy-duty universal stand via Manfrotto super clamp and 3D junior camera head, were used to track the robotic fish swimming. A computer equipped with Motive 1.7.5 software, capable of supporting real-time and offline work-flows, was used to extract the desired data. The details of this setup are shown in Fig. 2.8. Two different locomotion modes, forward swimming and turning, were adopted for the robotic fish in the experiments. For each experiment, the robotic fish swam for approximately 30 seconds to reach its steady-state motion, and then the steady-state data were captured and extracted. In the forward swimming case, we recorded the time it took for the robot to swim a distance of 50 cm. The experiment for each setting was repeated ten times, to minimize the impact of random factors on the experimental results.

2.6.4 Parameter Identification

All the parameters used in the simulations were either measured directly or identified experimentally. Details of the identification procedure for parameters of the robotic fish body can be found in [86, 87]. The mass of the robotic fish was $m_b = 0.502$ kg and the inertia was evaluated to be $I_z = 7.26 \times 10^{-4}$ kg/m^2. The added masses and added inertia were calculated based on a prolate spheroid approximation for the robotic fish body [28, 88], which were $-X_{\dot{V}_{Cx}} = 0.1619$ kg, $-Y_{\dot{V}_{Cy}} = 0.3057$ kg, and $-N_{\dot{\omega}_{Cx}} = 5.52 \times 10^{-5}$ kg/m^2. The wetted surface area of the robotic fish body was $S_A = 0.0325$ m^2. The drag, lift, and moment coefficients were identified empirically, using the rigid pectoral fins and $\zeta = 2$. In particular, these parameters were tuned to match the forward velocity, turning radius, and turning period obtained in simulation with the experimental measurement, when two different power stroke speeds are used, completing the power stroke in 0.5 s and 0.3 s, respectively. The resulting coefficients were $C_D = 0.42$, $C_L = 4.86$, and $C_M = 7.6 \times 10^{-4}$ kg/m^2. The parameter λ from Eq. (2.20), which represents the hydrodynamic force coefficient of the pectoral fin, was identified empirically to be 0.6, by matching the forward swimming velocity of the robotic fish utilizing rigid pectoral fins for the fin-beat frequencies of 1 Hz and 1.667 Hz, and power/recovery stroke ratio $\zeta = 2$. This parameter was then used for all the other fin-beat frequencies, pectoral fin flexibilities, and ζ ratios.

The spring and damper coefficients of the flexible fins were tuned to match the forward swimming velocity and the turning period of the robotic fish collected from experiments for $\zeta = 2$, and fin-beat frequencies of 1 Hz and 1.667 Hz. Each fin is discretized into three elements. The parameters for each fin are summarized in Table 2.1. These numbers were then used for all the other fin-beat frequencies and ζ ratios throughout the simulations.

2.7 Results and Analysis

2.7.1 Dynamic Model Validation

First, we have included plots of simulation results to illustrate how the flexible pectoral fin moves. The time history of the angles of different elements of the flexible pectoral fin, and the respective angles of attack, is shown in Fig. 2.9. In this simulation, the flexible fin F2 was used. Note the clear phase lags between the consecutive elements' angles γ_i. The angles of attack for all elements are constant (90 or -90 degrees) for most of the time, but they experience abrupt changes during the transition between power and recovery strokes.

Next, we present results that validate our proposed dynamic model, where the case of pectoral fin F2 with $\zeta = 2$ is used. Additional results supporting the model can be found in Section 2.7.2. Fig. 2.10 shows the comparison between model predictions and experimental measurements of the forward swimming velocity, reported in both cm/s and BL/s (body length per second) versus the fin-beat frequency. The fin-beat frequency is defined as $\frac{1}{T_p}$, where T_p is the duration of each fin-beat cycle. In the experiments, for $\zeta = 2$, the speed limit of the servo motors translated to a maximum actuation frequency of 2 Hz, so we have extended the simulation results to fin-beat frequency of 3 Hz in order to capture the performance trend of the robotic fish. From Fig. 2.10, the speed of the robotic fish drops after the fin-beat frequency reaches an optimal value, beyond which it gets harder for the flexible pectoral fins to follow the prescribed servo motion. Figs. 2.11 and 2.12 show a comparison between simulation and experimental results on the turning period and the turning radius versus fin-beat frequency, respectively. In Fig. 2.11, the turning period

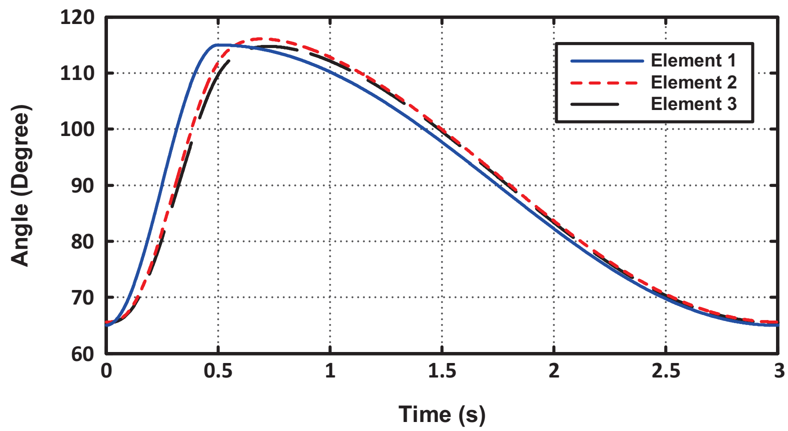

(a)

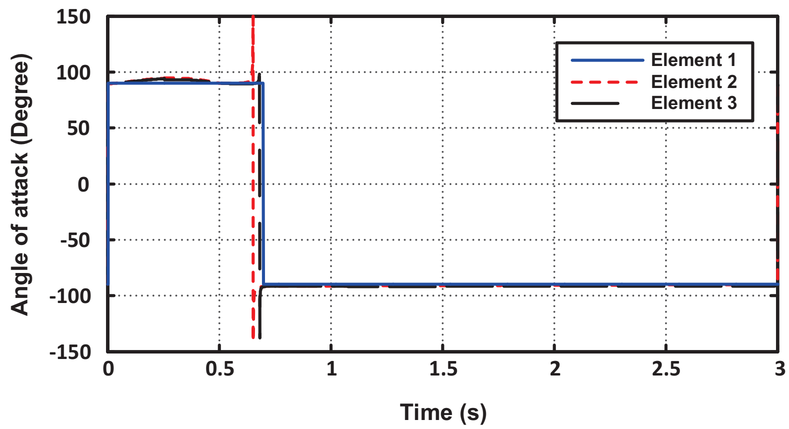

(b)

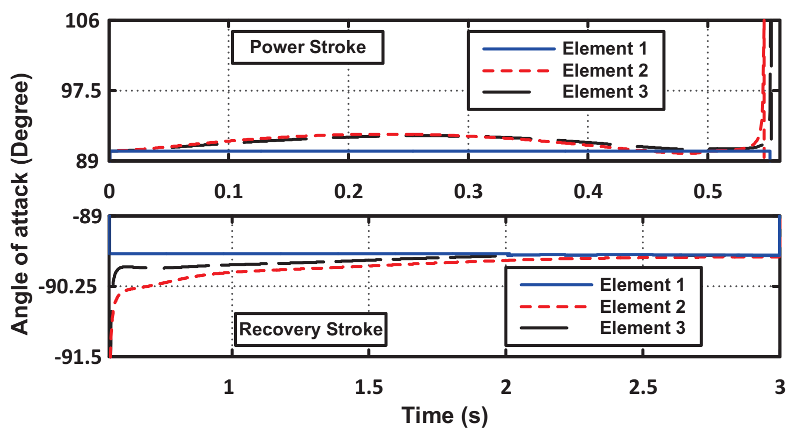

(c)

Figure 2.9: Time history of flexible pectoral fin: (a) Evolution of the rigid element angles $\gamma_1 - \gamma_3$, for one movement cycle, (b) variation of the angles of attack for all elements, where $\zeta = 5$, $\gamma_A = 50$ deg, and $T_p = 3$ s, (c) zoom-in view of the angle of attack for one movement cycle.

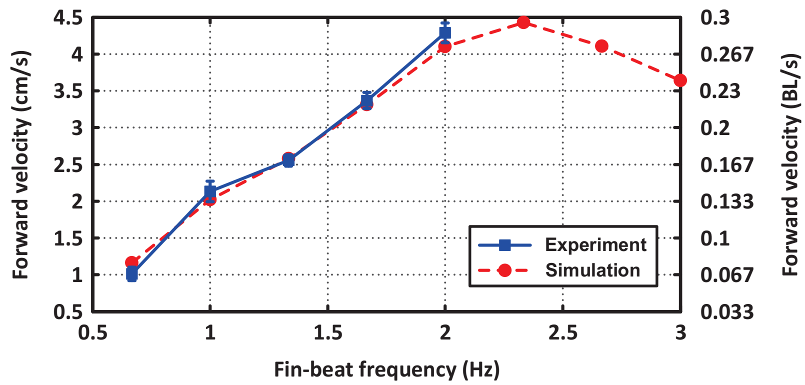

Figure 2.10: Case of F2 with $\zeta = 2$: Comparison between dynamic model simulation and experimental measurement of the forward swimming velocity, for different fin-beat frequencies.

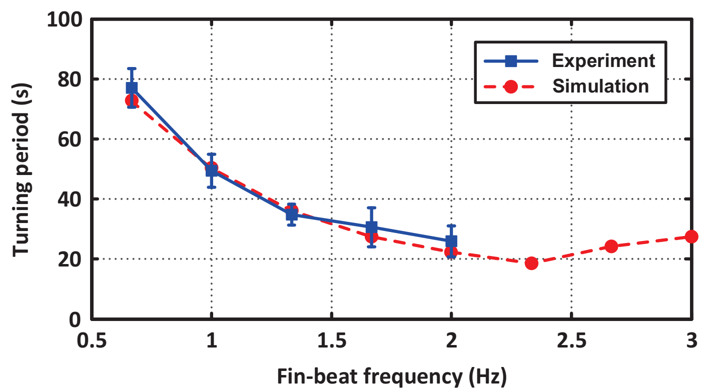

Figure 2.11: Case of F2 with $\zeta = 2$: Comparison between dynamic model simulation and experimental measurement of the turning period, for different fin-beat frequencies.

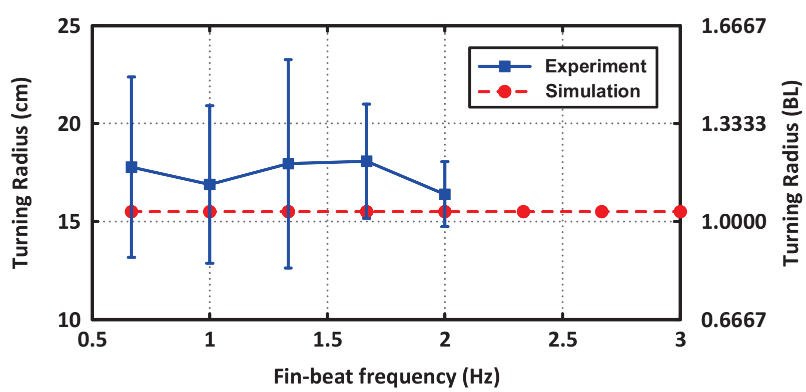

Figure 2.12: Case of F2 with $\zeta = 2$: Comparison between dynamic model simulation and experimental measurement of the turning radius, for different fin-beat frequencies.

drops with the fin beat rate, as expected, up to a particular optimal frequency, beyond which it starts to increase. The optimal frequency in Fig. 2.11 coincides with that in Fig. 2.10, which is

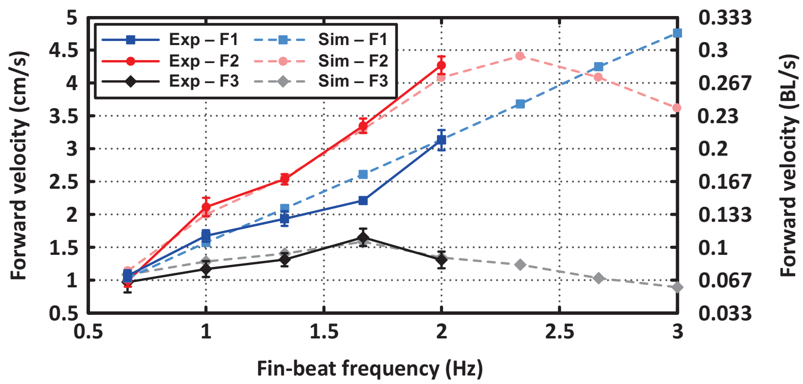

Figure 2.13: Experimental and simulation results on the forward swimming velocity versus fin-beat frequency for different flexibilities of the pectoral fin, where the power/recovery stroke ratio $\zeta = 2$ for all cases.

not surprising. The simulation results in Fig. 2.12 suggest that the turning radius of the robotic fish is nearly independent of fin-beat frequencies. The experimental data support the simulation to some extent. The mean of the turning radius remains almost the same (between 16 and 18 cm) for different fin-beat frequencies. Due to the disturbances from the interaction between the fluid and the tank wall, the robotic fish typically would not stay repeatedly on the same orbit in each turning experiment, which inevitably introduced noticeable error in the turning radius measurement.

Overall, it can be concluded from Figs. 2.10 - 2.12 that the proposed dynamic model can well capture the motion of the robotic fish actuated by flexible pectoral fins. Additional results in Section 2.7.2 will further validate the model through good match between experimental and simulation results.

2.7.2 Impact of Fin Stiffness

Here we compare the performance of pectoral fins with different flexibilities to gain insight into the influence of fin flexibility. We utilized a fin-beat pattern as specified in (2.31), where $\zeta = 2$. The simulation and experimental results, shown in Fig. 2.13, are reported both in cm/s and BL/s. Again, we have extended the simulation results to fin-beat frequency of 3 Hz in order to capture the performance trend of the robotic fish. From Fig. 2.13, it is interesting to note that with rigid fins (F1), the swimming velocity increases nearly linearly with the fin-beat frequency, while for the flexible fins (F2 and F3), there is a clear optimal frequency at which the velocity is maximum. Fins with moderate flexibility outperform the rigid fins for the entire fin-beat frequency range achievable by the robotic fish prototype. The optimal frequency of operation for the flexible fin case is believed to be correlated to the resonant frequency of the fin in water, and it drops as the flexibility of the fin increases. When the fin is too flexible (F3), the robotic fish's speed performance becomes poor.

2.7.3 Impact of the Power to Recovery Stroke Speed Ratio

This subsection is devoted to studying the effect of the power to recovery stroke speed ratio (ζ) on the performance of the robotic fish. For a fixed power stroke speed, a higher ζ results in a slower overall fin-beat frequency, which could imply a slower swimming speed for the robot; on the other hand, a higher ζ means slower recovery stroke speed, which means weaker "braking" force and potentially helps increase the overall swimming speed. Fig. 2.14 shows the experimental results on the forward swimming velocity, comparing the cases of $\zeta = 2$ and 4. Here the fin flexibility spans F1–F3. Fig. 2.14(a) shows the velocity versus fin-beat frequency. Overall, it can be seen that the higher ζ provides better performance for each fin flexibility at each fin-beat frequency. Note that the rightmost point in each curve corresponds to the maximum speed that the servo can handle. Fig. 2.14(b) presents the comparison on the swimming velocity versus the power stroke time (duration). Note that while the performance of the robotic fish with the larger ratio, $\zeta = 4$, outperforms the case of $\zeta = 2$ most of the time, for the most flexible fin F3, the case of $\zeta = 2$ outperforms that of $\zeta = 4$ when the power stroke time is small (or equivalently, at high power stroke speeds). Therefore, in the following we use model-based simulation to further study the impact of the power to recovery stroke speed ratio.

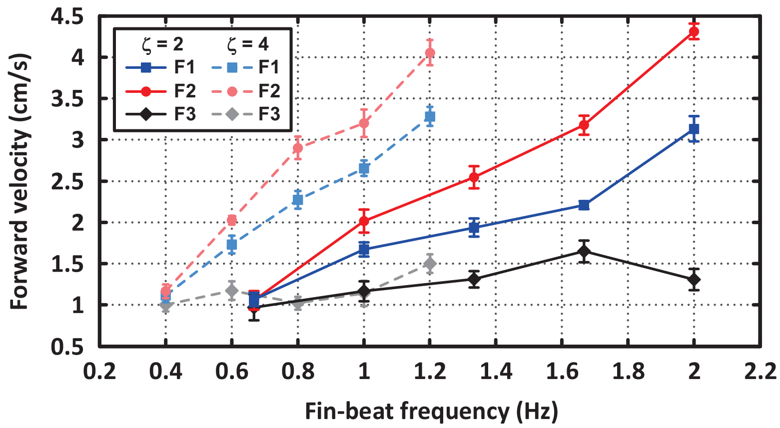

(a)

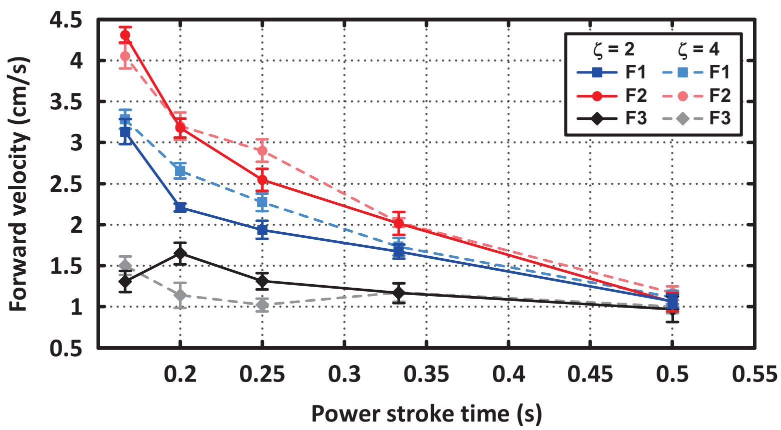

(b)

Figure 2.14: Experimental comparison of the forward swimming velocities at different power/recovery stroke speed ratios $\zeta = 2$ and $\zeta = 4$. (a) Velocity versus fin-beat frequency, and (b) Velocity versus power stroke time.

Fig. 2.15 provides a comparison within a wider range of power/recovery stroke speed ratios $\zeta = 1.5$, 2, 3, 4, and 5, for pectoral fins F1 – F3, and for an extended fin-beat frequency. In all simulations the maximum servo speed is fixed, which corresponds to a fin-beat frequency of 3 Hz when $\zeta = 2$. Therefore, the rightmost point on each curve represents the highest fin-beat frequency achievable with the corresponding ζ under the servo constraint. From Fig. 2.15(a), one can conclude that for the rigid pectoral fin F1, a higher ζ provides a faster swimming speed at each fin-beat frequency, which matches the results from Fig. 2.14. On the other hand, the

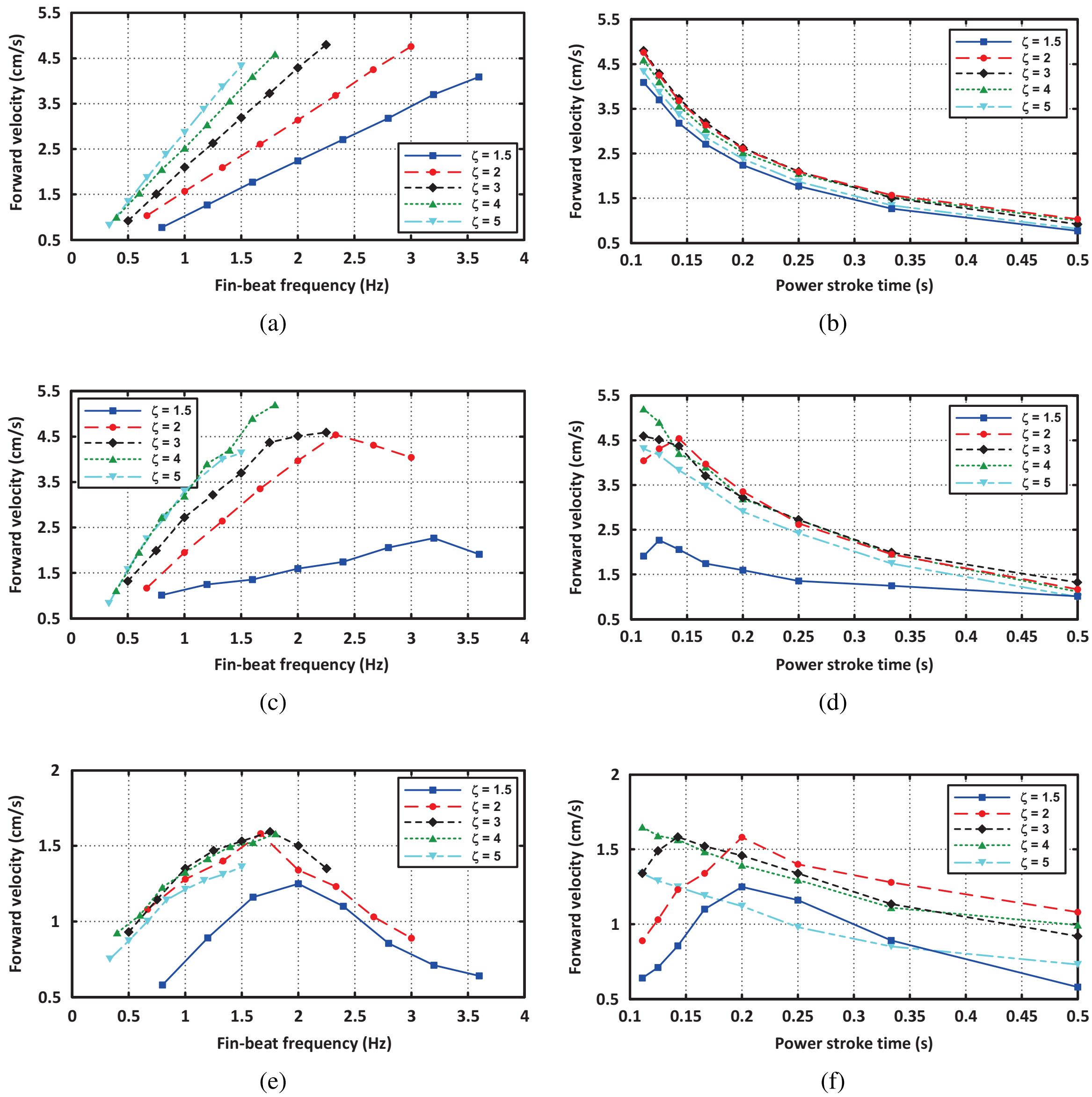

Figure 2.15: Simulation comparison of the forward swimming velocities at different power/recovery stroke speed ratios $\zeta = 1.5$, 2, 3, 4, and 5. (a) Velocity versus fin-beat frequency for case of F1,(b) velocity versus power stroke time for case of F1, (c) velocity versus fin-beat frequency for case of F2, (d) velocity versus power stroke time for case of F2, (e) velocity versus fin-beat frequency for case of F3, (f) velocity versus power stroke time for case of F3.

highest achievable swimming speed under the constraint of the servo speed, does not happen at the highest ζ. Instead, the highest swimming speed is obtained if a moderate ζ (2 or 3) is used. From Figs. 2.15(c) and (e), it can be observed that, for flexible fins, the swimming speed is no longer a monotone increasing function of ζ at each fin-beat frequency. There is a critical value ζ^*, beyond

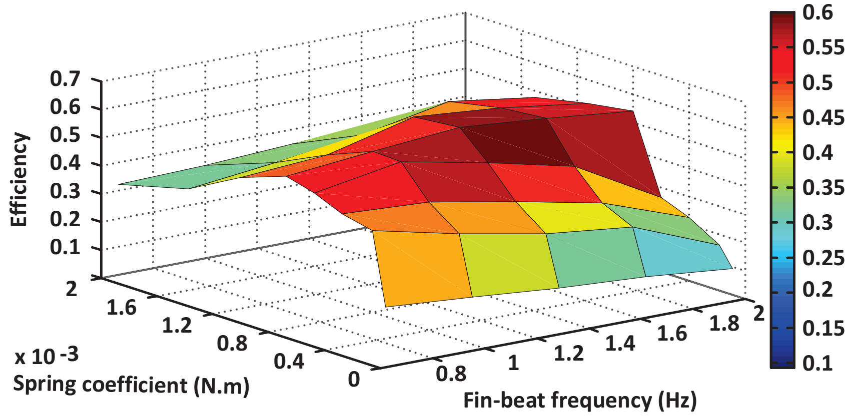

Figure 2.16: Calculated mechanical efficiency versus fin-beat frequency and spring constant of the flexible fins.

which a higher ζ results in a slower robot speed for a given fin-beat frequency. In addition, by comparing Figs. 2.15(c) and (e), the more flexible the fin is, the lower ζ^*; in particular, $\zeta^* = 4$ for F2, and $\zeta^* = 3$ for F3. For each flexible fin, the maximum swimming speed achievable with servo constraints takes place at the optimal fin-beat frequency when the power/recovery stroke speed ratio is ζ^*. Similarly, Figs. 2.15(b), (d), and (f) present the comparison on the swimming velocity versus the power stroke time. Since we fix the amplitude γ_A of the fin beat, each power stroke time corresponds to a particular power stroke speed. From the figures, it is clear that, for each fin, for any given power stroke speed, there is an intermediate value ζ^* that achieves the best swimming speed. In other words, for a given power stroke speed, there is an optimal recovery stroke speed, not too high, not too low.

2.7.4 Impact of Flexibility on Mechanical Efficiency

Finally we focus on the mechanical efficiency of the robotic fish. Fig. 2.16 shows the efficiency curve versus fin-beat frequency and spring constant values of the flexible fins. Here the calculations are based on power/recovery stroke speed ratio $\zeta = 2$. We considered eight different fins with different spring constants, where the damper to spring constant ratio, κ, was kept at 0.24. This value matches the ratios obtained from the tested pectoral fins F2 and F3 in this work (0.23 and 0.24, respectively, from the parameters in Table 2.1). The figure confirms that there is an optimal flexibility for each fin-beat frequency, that results the highest mechanical efficiency for the robotic fish. Additional insight can be drawn based on Fig. 2.17(a), where the computed mechanical efficiency of the robot is shown as a function of the fin-beat frequency, for all three fins F1 – F3. It can be seen that the mechanical efficiency of the rigid fin (F1) slightly increases with the fin-beat frequencies. On the other hand, flexible fins tend to be more efficient at lower frequencies. In fact, the efficiency with fin F2 is higher than that with F1 when for frequencies lower than 2.7 Hz; and even fin F3 outperforms F1 on efficiency until the frequency reaches about 1.2 Hz.

To bring additional insight into the robotic fish performance analysis, one can further study some non-dimensionalize parameters of the robotic fish. These parameters include the Reynolds number, $Re = \frac{|V_C|L}{\nu}$, and the Strouhal number $St = \frac{2fS\sin\gamma_A}{|V_C|}$, where $|V_C|$ is the swimming speed of the robot, L is the robotic fish length, ν is the kinematic viscosity of water, S is the pectoral fin span length, γ_A is the fin flapping amplitude [27,35], and f is the fin-beat frequency. Another non-dimensionalize parameter of interest is the dimensionless velocity, which is defined as $V_{DL} = \frac{|V_C|}{S\omega_A}$, where $\omega_A = \pi\frac{(\zeta+1)}{T_p}$. These dimensionless parameters are reported in Fig. 2.17 for pectoral fins with different flexibilities and ζ=2, versus different fin-beat frequencies. Fig. 2.17(a) shows a distinct inverse correlation between the efficiency and the Strouhal number. For each fin flexibility, when the Strouhal number is at its lowest, the efficiency is highest. Fig. 2.17(b) shows that the robotic fish demonstrates the highest dimensionless velocity when the Reynolds number is at the lower end, except for the rigid fin (F1), where the dimensionless velocity remains almost constant. Fig. 2.17(c) shows that the optimal frequency for the forward swimming velocity of the robotic fish for each fin does not coincide with the optimal frequency for the efficiency. Therefore, the model presented in this paper can be used as a tool to address an optimal, multi-objective design problem.

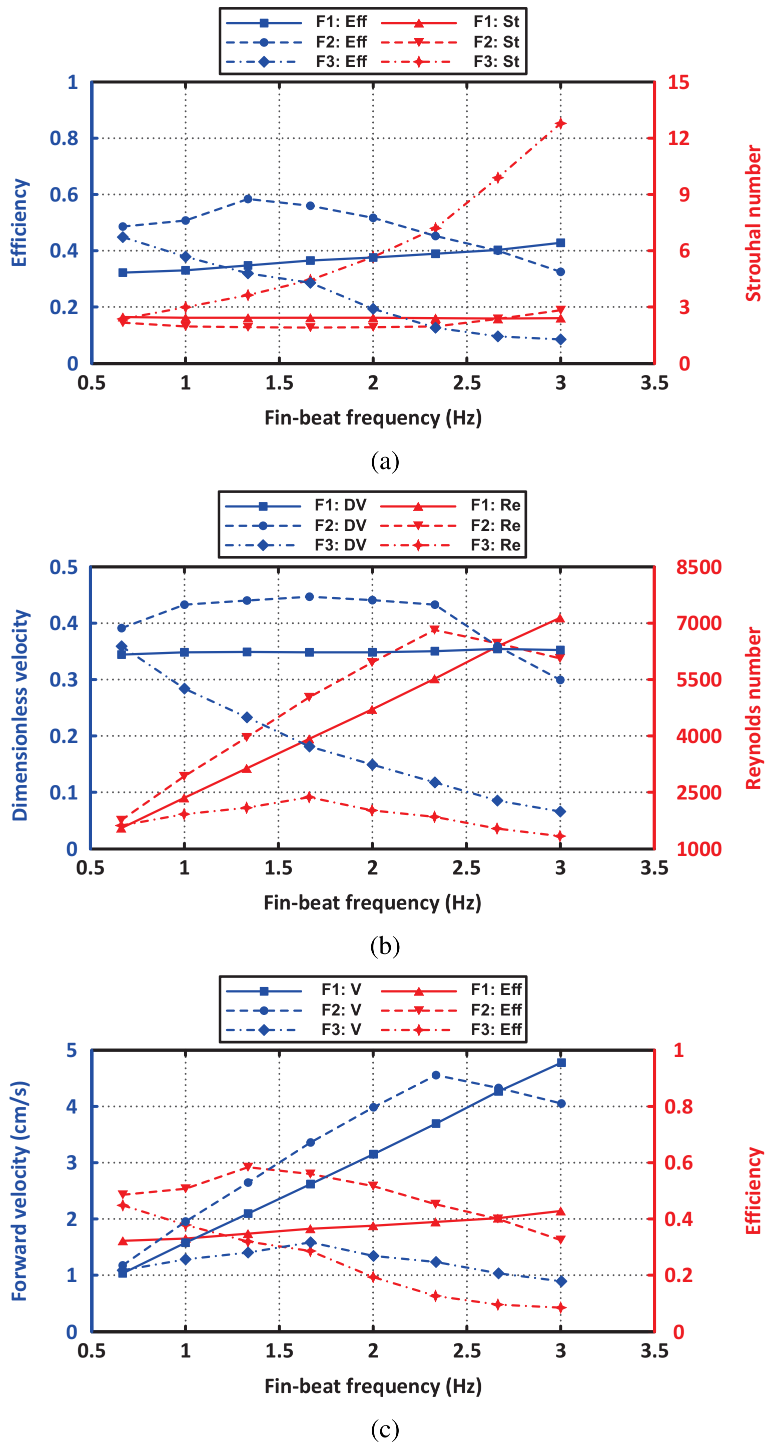

Figure 2.17: Comparison of non-dimensionalized parameters of the robotic fish actuated by paired pectoral fins with different flexibilities versus different fin-beat frequencies for the case of $\zeta = 2$: (a) Calculated efficiency and Strouhal number, (b) dimensionless velocity and Reynolds number, and (c) forward swimming velocity in cm/s and efficiency.

Note that the Strouhal numbers shown here are higher than 1, which are far from the Strouhal numbers of biological fish, (typically in the range of 0.25-0.5 [35, 95, 96]). The reason is that the robotic fish used in this study is driven solely by the pectoral fins, which results in relatively low forward swimming speeds and thus large Strouhal numbers.

2.8 Conclusion

The goal of this chapter was to study the impact of the pectoral fin flexibility on the robotic fish performance and mechanical efficiency. We introduced a novel dynamic model for a robotic fish actuated with paired pectoral fins, where the fin is modeled as multiple rigid elements joined through torsional springs and dampers and blade element theory is used to calculate the hydrodynamic forces on the elements. The dynamic model was validated through experiments conducted on a robotic fish, where the swimming and turning performance of the robot was measured for fins with different flexibilities (two flexible, one rigid). The model was then used extensively to evaluate the impacts of fin stiffness, fin-beat frequency, and power/recovery stroke speed ratio on robot swimming speed and mechanical efficiency. It is found that fins with more flexibility are the winner in terms of robotic fish forward velocity performance in lower fin-beat frequencies and for higher frequencies, more rigid fins outperform the flexible fins. As for the effect of ζ on robotic fish performance, we found that more flexible fins have lower critical $zeta^*$, which corresponds to the maximum swimming speed achievable for robotic fish. In other words, there is an optimal recovery stroke speed, which results in the best performance of robotic fish for a given power stroke. The analysis reveals the intricate trade-off between objectives (swimming speed versus efficiency) and supports the use of the presented model for multi-objective design of fin morphology and control.

Chapter 3

Design and Modeling of Flexible Passive Rowing Joint for Robotic Fish Pectoral Fins

3.1 Introduction

One of the swimming modes that a live fish often uses in maneuvering and assistive propulsion is the "labriform" swimming mode, in which the fish oscillates its paired pectoral fins to generate thrust [5, 11]. Previous works done on a robotic fish actuated by paired pectoral fins include both rigid pectoral fins [35,44,55,81,93] and flexible fins or fins with controlled curvature [21,32,62,83]. As illustrated in Figure 3.1, pectoral fin motions can generally be classified into three modes based on the axis of rotation, rowing, feathering, and flapping. The feathering motion represents fin

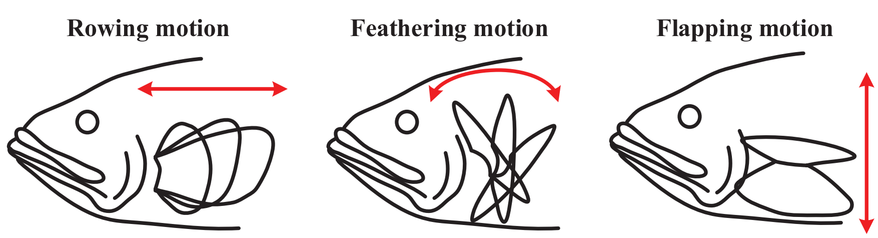

Figure 3.1: Types of pectoral fin motion (Adapted from [81]). The rotation axes for the rowing, feathering, and flapping motions are vertical, transverse, and longitudinal, respectively.

rotation about the transverse axis, and in robotic fish, feathering pectoral fins have often been used as bow planes to control the dive and ascent of the robots [44,97,98]. The flapping motion involves fin rotation about the longitudinal axis, which has been used in several robotic manta rays involving expanded flexible pectoral fins [99,100]. Finally, the rowing motion involves fin rotation about the vertical axis, which can be utilized for a number of in-plane locomotion and maneuvering tasks, such as forward swimming, sideway swimming, and turning [101].

The fin-beat cycle in the rowing motion involves a power stroke, where the fin rotates toward the back of the robot and gains thrust via the induced-drag on the fin, and a recovery stroke, where the fin rotates back toward the front of the body and gets ready for the next cycle. In order to generate a net thrust over each cycle, the fin has to be actuated differently in the power and recovery strokes. For example, one can actuate the fin (much) faster in the power stroke than in the recovery stroke [21]. The downside of this approach, however, is that the robot will decelerate and lose momentum during the extended recovery stroke and the resulting robot motion is slow. An alternative approach is to feather the fin to reduce its effective area and thus drag during the recovery stroke [27, 35, 101]. The latter, however, entails the need of one additional actuator for each pectoral fin, which significantly increases the size, weight, and complexity of the fins and the overall robot.

The contribution of this chapter is the proposal and modeling of a flexible, passive joint for a pectoral fin that enables net thrust generation under symmetric actuation of a single rowing actuator in power and recovery strokes. The proposed design has significantly reduced complexity and cost comparing to the approach adopting active feathering, and as demonstrated later in the paper, it results in superior swimming performance comparing to the case of a single actuator with a rigid link and differential power/recovery actuation. The flexible joint allows the pectoral fin to sweep back passively during the recovery stroke, while following the motion prescribed by the actuator during the power stroke. Consequently, the fin experiences less drag in the recovery stroke than in the power stroke, resulting in a net thrust. To analyze the robot locomotion performance, a dynamic model is developed for the joint and fin structure and for a robotic fish equipped with a pair of such pectoral fins. This model is then validated by performing experiments on a free-swimming robotic fish. Experiments are also conducted to compare the robot performance using the flexible joint with the case where a rigid joint is used. The model is further exploited to investigate the effect of length and stiffness of the flexible joint on the robotic fish swimming performance at different fin-beat frequencies. Joint structures of different length and stiffness values are prototyped with a multi-material 3D printer to confirm the model analysis. Finally, the mechanical efficiency for a given flexible joint design is computed, which, along with the swimming performance analysis, offers an instrumental tool for multi-objective optimization of the fin joint and its operating frequency.

The remainder of this chapter is organized as follows. The design and prototyping of the flexible rowing joint are described in detail in Section 3.2. Section 3.3 presents the dynamic model for the joint structure along with the model for robotic fish adopting such joints for pectoral fins. Blade element theory is used to calculate the hydrodynamic forces on the pectoral fins, and the flexible rowing joint is modeled as a pair of torsional spring and damper. In Section 3.4, experimental results are provided to support the modeling analysis. The effect of the flexible joint length and stiffness is investigated in Section 3.5. The mechanical efficiency of robotic fish adopting a given design of the pectoral fin joint is derived and explored numerically in Section 3.6. Finally, concluding remarks are provided in Section 3.7.

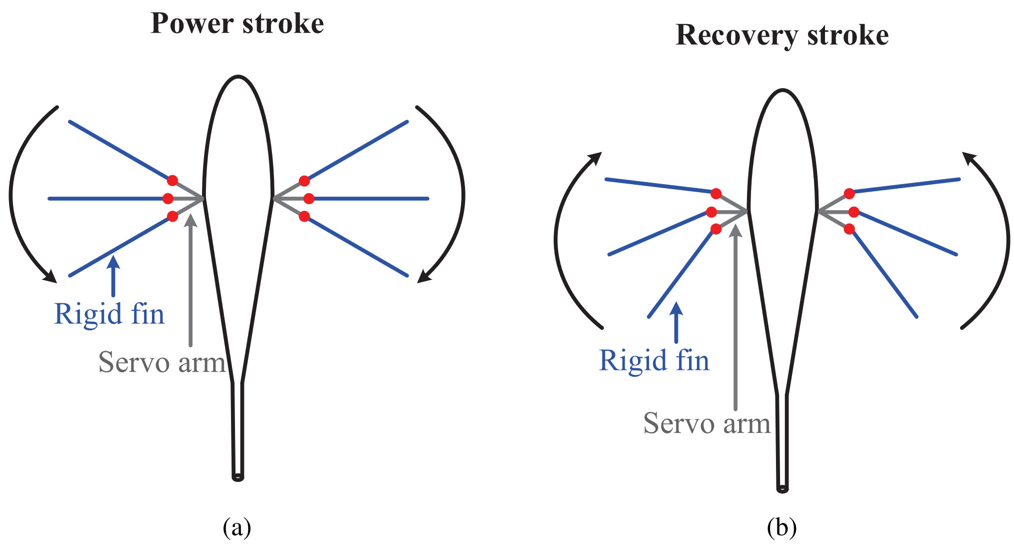

Figure 3.2: Illustration of the motion of the pectoral fins with flexible rowing joints (top view): (a) Power stroke, (b) recovery stroke. The flexible joints are marked with red dots.

3.2 Joint Design

This section is dedicated to describing the design and prototyping of the proposed flexible rowing joint. Each pectoral fin moves back and forth utilizing a servo motor as the source of actuation. In fish locomotion, the main target is to maximize the overall thrust force and minimize the hydrodynamic drag force in the recovery stroke [5]. To meet this goal for a robotic fish, the flexible rowing joint is designed such that the pectoral fin maintains the motion prescribed by the servo in the power stroke, to produce the maximum thrust, while sweeping back passively along the body in the recovery stroke, to minimize the drag force on the fin. Figure 3.2(a) and 3.2(b) illustrate the motion of the pectoral fins with the flexible rowing joints during the power and recovery strokes, respectively. One can see that in this case the fin plane stays vertical throughout the stroke cycle and thus the resulting hydrodynamic force is restricted to the horizontal plane. SolidWorks software is used to design the passive joints, which is shown in Figure 3.3. The entire joint assembly consists of four parts: (1) a rigid servo arm connection that will fit to the servo arm, (2) a mechanical stopper rigidly attached to the servo arm connection, (3) a fin mount (rigid) with a slit for

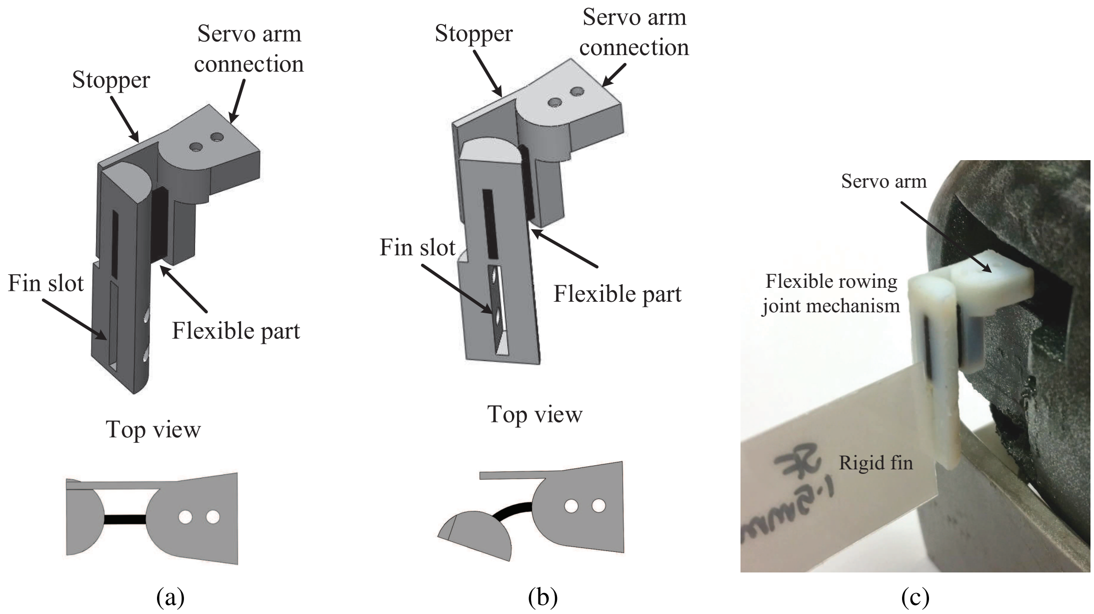

Figure 3.3: The proposed flexible rowing joint designed in SolidWorks software: (a) During the power stroke, the mechanical stopper prevents the fin from sweeping forward passively (which would reduce thrust), (b) during the recovery stroke, the fin bends back passively under the hydrodynamic forces, which reduces the drag on the fin and thus on the robot, and (c) 3D-printed rowing passive joint assembled on the robotic fish.

attaching the pectoral fin, and (4) a piece of flexible material with a rectangular shape, serving as the joint between the servo arm connection and the fin mount. The stopper is designed to prevent the pectoral fin from sweeping forward passively and let it follow the prescribed servo motion, during the power stroke, as illustrated in Figures 3.2(a) and 3.3(a), while allowing the fin to sweep back passively during the recovery stroke, as illustrated in Figures 3.2(b) and 3.3(b).

The joint is prototyped using a multi-material 3D printer (Connex 350 from Objet). The printer is capable of simultaneously jetting rigid and flexible materials, so the entire joint structure is printed seamlessly as a single piece, as shown in Figure 3.3(c). All the rigid parts are printed with RGD835 (VeroWhitePlus). Two different materials, FLX980 (TangoBlackPlus), which is the most flexible material from the printer, and DM9850 (Digital Material 9850), which is still flexible but stiffer than the former, are explored for the flexible part of the joint structure. Other than different stiffnesses for the flexible part, we aim to investigate the effect of joint dimension on the

Table 3.1: Specifications of four different flexible rowing joints.

Joint name	Flexible part material	Flexible part length (mm)
JR1	FLX980	0.5
JR2	FLX980	1
JR3	FLX980	1.5
JR4	DM9850	0.5

performance of the fish as well. To do so, four different joints are printed, three using FLX980 and one using DM9850. All the joints have fixed depth and thickness of 10 mm and 1 mm, respectively, to ensure the joints survive through extensive experiments. Table 3.1 summarizes the specifications of all four joints.

3.3 Dynamic Modeling

One of the main foci of this work is to analyze and compare the passive joint mechanism with a traditional rigid joint. For this purpose, we have developed a dynamic model for robotic fish propelled with pectoral fins, for the case involving flexible, passive rowing joints. The fluid that the robotic fish operates in is considered to be inviscid and incompressible. The robot is assumed to have a rigid body with a pair of rigid pectoral fins, which are coupled to the actuator arms through the proposed flexible joints. While one can incorporate an active caudal fin for the robotic fish, as we did for our prototype reported in this paper, its modeling and study are outside the scope of this work. The blade element theory [5] is used to evaluate the hydrodynamic forces generated by the pectoral fins.

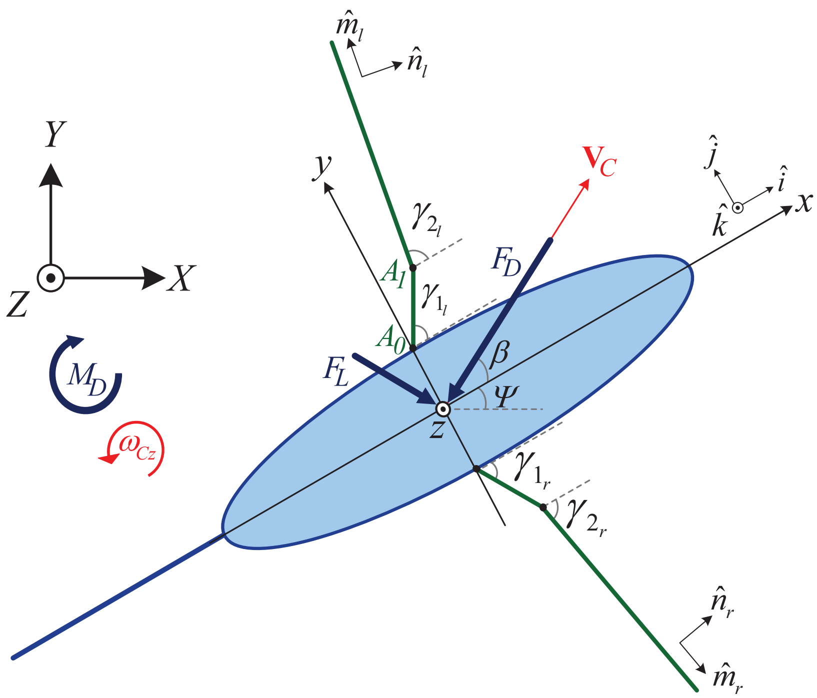

Figure 3.4: Top view of the robotic fish actuated by pectoral fins in a planar motion.

3.3.1 Rigid Body Dynamics

To model the robotic fish motion properly, some coordinate systems need to be defined. As illustrated in Figure 3.4, the inertial coordinate system is denoted with $[X,Y,Z]$, and the body-fixed coordinate system is represented by $[x,y,z]$, with the corresponding unit vectors denoted by $[\hat{i},\hat{j},\hat{k}]$, which is attached to the center of mass of the robotic fish. Here the x-axis is along the body's longitudinal axis pointing to the head, the z-axis is perpendicular to the x-axis and points upward, and the y-axis is automatically formed by the right-hand orthonormal principle. We denote by $\vec{r}_{c_p} = c_p\hat{j}$ the vector pointing from robotic fish center of mass to the base of the pectoral fin servomotor (point A_0). Point A_1 is the base of the pectoral fin. We use $\hat{m}$ and $\hat{n}$ to denote the unit vectors parallel and perpendicular, respectively, to each pectoral fin, where subscripts r and l are used to denote the right and left fins, respectively. The robotic fish is considered to be neutrally buoyant. Let $\mathbf{V}_C = [V_{C_x}, V_{C_y}, V_{C_z}]^T$ denote the velocity vector of the robotic fish in the body-fixed coordinates, where V_{C_x}, V_{C_y}, and V_{C_z} are the surge, sway, and heave components, respectively. On the other hand, $\omega_C = [\omega_{C_x}, \omega_{C_y}, \omega_{C_z}]^T$ denotes the body-fixed angular velocity vector of the body, where ω_{C_x}, ω_{C_y}, and ω_{C_z} are the roll, pitch, and yaw components, respectively. We use γ_1 and γ_2, along with subscripts r and l, to denote the angle of the servo, and deflection angle of each pectoral fin with respect to the x-axis, respectively. The angle of attack for the body is denoted as β, which is the angle between the x-direction of the body-fixed coordinate system and the velocity vector $\mathbf{V}_C$. Finally, let ψ denote the angle between the x-axis and X-axis.

The rigid body dynamics in the body-fixed coordinates are represented as [102]

$$\begin{bmatrix} \mathbf{m} & 0 \\ 0 & \mathbf{I} \end{bmatrix} \begin{bmatrix} \dot{\mathbf{V}}_C \\ \dot{\omega}_C \end{bmatrix} + \begin{bmatrix} \omega_C \times \mathbf{m}\mathbf{V}_C \\ \omega_C \times \mathbf{I}\omega_C \end{bmatrix} = \begin{bmatrix} \mathbf{f} \\ \tau \end{bmatrix}, \tag{3.1}$$

where $\mathbf{m}$ is the mass matrix (incorporating both the actual robot mass and the added mass, which is calculated considering an ellipsoid accelerating in the fluid [63]), $\mathbf{I}$ is the inertia matrix (including both the actual and added inertias), $\mathbf{f} = [f_x, f_y, f_z]^T$ represents the external hydrodynamic forces, $\tau = [\tau_x, \tau_y, \tau_z]^T$ represents the external moments, applied to the center of mass of the robotic fish, and "$\times$" denotes the vector product.

In this paper we focus on the planar motion for the robotic fish, so it has three degrees of freedom, namely, surge (V_{C_x}), sway (V_{C_y}), and yaw (ω_{C_z}). We further assume that the body is symmetric with respect to the xz-plane, the pectoral fins move in the xy-plane, and the z-axis of the body-fixed frame is parallel to the Z-axis of the inertial frame. The inertial couplings between these three states are assumed to be negligible [28], which simplifies Eq. (3.1) to

$$(m_b - m_{a_x})\dot{V}_{C_x} = (m_b - m_{a_y})V_{C_y}\omega_{C_z} + f_x, \tag{3.2}$$

$$(m_b - m_{a_y})\dot{V}_{C_y} = -(m_b - m_{a_x})V_{C_x}\omega_{C_z} + f_y, \tag{3.3}$$

$$(I_z - I_{a_z})\dot{\omega}_{C_z} = \tau_z, \tag{3.4}$$

where m_b is the robotic fish mass, $-m_{a_x}$ and $-m_{a_y}$ are the added mass components along the x and y directions of the body-fixed coordinates, respectively. I_z is the robot inertia about the z-axis, and $-I_{a_z}$ is the added inertia of the robot about the same axis. The variables f_x, f_y and τ_z denote the external hydrodynamic forces and moment exerted on the fish body, which are described as

$$f_x = F_{h_x} - F_D \cos\,\beta + F_L \sin\,\beta, \tag{3.5}$$

$$f_y = F_{h_y} - F_D \sin\,\beta - F_L \cos\,\beta, \tag{3.6}$$

$$\tau_z = M_{h_z} + M_D, \tag{3.7}$$

where F_{h_x}, F_{h_y} and M_{h_z} are the hydrodynamic forces and moment transmitted to the fish body by the pectoral fins and the calculation procedure is addressed in detail in Section 3.3.2. F_D, F_L, and M_D are the body drag, lift, and moment, respectively. These forces and moment are expressed as [28, 29, 44]

$$F_D = \frac{1}{2}\rho V_C^2 S_A C_D, \tag{3.8}$$

$$F_L = \frac{1}{2}\rho V_C^2 S_A C_L \beta, \tag{3.9}$$

$$M_D = -C_M \omega_{C_z}^2 \,\mathrm{sgn}(\omega_{C_z}), \tag{3.10}$$

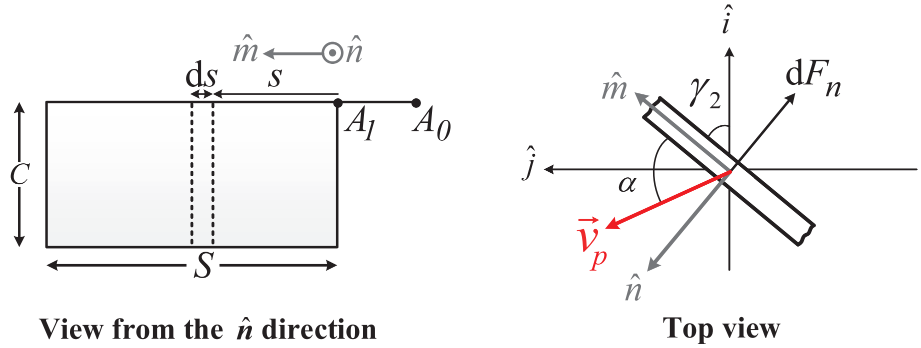

Figure 3.5: Illustration of a rigid, rectangular pectoral fin and its parameters and variables.

where V_C is the linear velocity magnitude of the robotic fish body, $V_C = \sqrt{V_{C_x}^2 + V_{C_y}^2}$, ρ is the mass density of water, S_A is the wetted area of the body, C_D, C_L and C_M are the dimensionless drag, lift, and damping moment coefficients, respectively, and sgn$(.)$ is the signum function.

Finally, the kinematics of the robotic fish is described as [29],

$$\dot{X} = V_{C_x} \cos \psi - V_{C_y} \sin \psi, \tag{3.11}$$

$$\dot{Y} = V_{C_y} \cos \psi + V_{C_x} \sin \psi, \tag{3.12}$$

$$\dot{\psi} = \omega_{C_z}. \tag{3.13}$$

3.3.2 Hydrodynamic Forces from Pectoral Fins with Flexible Rowing Joints

In this subsection, we present the detailed model for computing the hydrodynamic forces generated by the pectoral fins. First we introduce the blade element theory that is used to evaluate the hydrodynamic forces and moment for a given fin movement. We then describe the dynamic model of the pectoral fins under the proposed flexible joints, which enable the computation of the corresponding hydrodynamic forces and moment for a prescribed servo motion.

3.3.2.1 Blade Element Theory

Following [5], the blade element theory is used to evaluate the hydrodynamic forces on the pectoral fins. For ease of calculations, the pectoral fin is considered to be rectangular with span length S and chord length (depth) C, as illustrated in Figure 3.5. The following calculation uses the left pectoral fin as an example, but it will extend trivially to the right pectoral fin.

The relationship between the unit vectors $\hat{m}$ and $\hat{n}$, and the body-fixed coordinates is given by

$$\hat{m} = \cos\gamma_{2_l}\ \hat{i} + \sin\gamma_{2_l}\ \hat{j}, \tag{3.14}$$

$$\hat{n} = -\sin\gamma_{2_l}\ \hat{i} + \cos\gamma_{2_l}\ \hat{j}. \tag{3.15}$$

The hydrodynamic forces on the pectoral fin have span-wise and normal components. Since the pectoral fins are considered to have pure rowing motion in this work, the angle between the pectoral fin and the flow is large, which results in a very small span-wise force, which arises from friction, and can be neglected [103]. In blade element theory, the normal force $\mathrm{d}F_n(s,t)$ is calculated on each defined blade element, ds, at time t

$$\mathrm{d}F_n(s,t) = \frac{1}{2}C_n\rho C|\vec{v}_p(s,t)|^2\mathrm{d}s, \tag{3.16}$$

where $\vec{v}_p(s,t)$ is the velocity of each blade element of the pectoral fin as a result of both the robot body motion and the pectoral fin motion, and C_n is the normal force coefficient, which depends on the angle of attack of each arbitrary blade, $\alpha(s,t)$. Utilizing a model empirically evaluated for insect wings and assuming that its validity holds underwater [63], $C_n = 3.4\sin\alpha$. The details on calculating the angle of attack for the fin is presented in Section 3.3.2.2. The total hydrodynamic force acting on each pectoral fin is calculated by integrating the force density along the span length

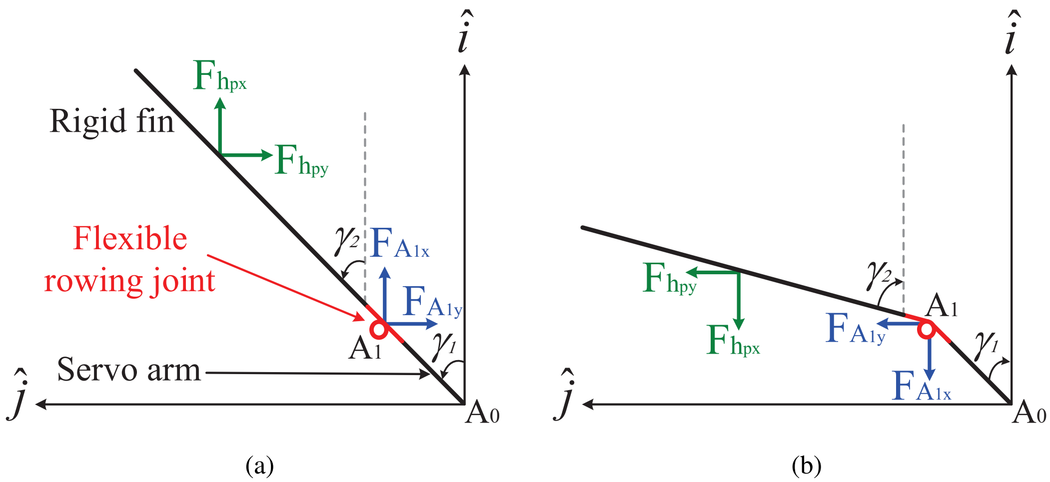

Figure 3.6: Dynamic configuration of the pectoral fin with flexible rowing joint during: (a) Power stroke, and (b) recovery stroke. A_1 represents the flexible joint.

of the fin

$$F_n(t) = \int_0^S \mathrm{d}F_n(s,t) \; . \tag{3.17}$$

3.3.2.2 Modeling of the Flexible Joint

The motion of the fin in both power and recovery strokes should be known, in order to utilize blade element theory to calculate the hydrodynamic forces. To do so, the flexible rowing joint is modeled as a couple of torsional spring and damper, where the parameters are derived from the properties of the flexible part and its dimensions. We consider the servo arm and the rigid pectoral fin as two links, which are connected by the flexible rowing joint. We denote the angles made by the first and second links with respect to the x-axis as γ_1 and γ_2, respectively. As illustrated in Figure 3.6(a), during the power stroke, the angle γ_1 is dictated by the servo and the fin follows the prescribed motion of the servo arm, resulting in $\gamma_2 = \gamma_1$, so the trajectory of the pectoral fin is fully known. On the other hand, for the recovery stroke, the motion of each point on the rigid fin is determined by the hydrodynamic interactions, as shown in Figure 3.6(b). Therefore, we need to find the angle of the second link, γ_2, in order to compute the motion of each point on the fin.

Refer to Figure 3.4. Velocities of the point A_0 (base of the servomotor) and point A_1 (base of the pectoral fin) in the inertial frame can be expressed as

$$\vec{v}_{A_0}(t) = \left\{V_{C_x} - c_p \omega_{C_z}\right\} \ \hat{\imath} + \left\{V_{C_y}\right\} \ \hat{\jmath}, \tag{3.18}$$

$$\begin{aligned} \vec{v}_{A_1}(t) = \vec{v}_{A_0} &- \left\{l_1(\dot{\gamma}_1 + \omega_{C_z}) \sin\gamma_1\right\} \ \hat{\imath} \\ &+ \left\{l_1(\dot{\gamma}_1 + \omega_{C_z}) \cos\gamma_1\right\} \ \hat{\jmath}, \end{aligned} \tag{3.19}$$

where c_p is the distance from the body center to point A_0, and l_1 is the length of the servo arm. The velocity at each point s along the pectoral fin is

$$\begin{aligned} \vec{v}_p(s,t) &= \vec{v}_{A_1} - \left\{s(\dot{\gamma}_2 + \omega_{C_z}) \sin\gamma_2\right\} \ \hat{\imath} \\ &\quad + \left\{s(\dot{\gamma}_2 + \omega_{C_z}) \cos\gamma_2\right\} \ \hat{\jmath} \\ &= v_{px} \ \hat{\imath} + v_{py} \ \hat{\jmath}. \end{aligned} \tag{3.20}$$

The angle of attack of each blade element is calculated via

$$\tan\alpha = \frac{< v_p(s,t), \hat{n} >}{< v_p(s,t), \hat{m} >} = \frac{-v_{px}\sin\gamma_2 + v_{py}\cos\gamma_2}{v_{px}\cos\gamma_2 + v_{py}\sin\gamma_2}, \tag{3.21}$$

where $< \cdot, \cdot >$ denotes the inner product, v_{px} and v_{py} are the velocity of the pectoral fin in x and y direction, respectively. The total force acting on the rigid pectoral fin is

$$\vec{F}_2 = \vec{F}_n - \vec{F}_{A_1} = m_p \left.\frac{\mathrm{d}\vec{v}_p(s,t)}{\mathrm{d}t}\right|_{s=\frac{S}{2}}, \tag{3.22}$$

where $\vec{F}_{A_1}$ represents the force applied by the rigid pectoral fin on the servo arm, and m_p is the effective mass of the rigid fin (which contains the fin mass and the added mass, where the added mass is calculated base on a rigid plate moving in the water) [104].

The moment of the rigid fin relative to its pivot point (point A_1) is evaluated as

$$\vec{M}_n = \int_0^S s\hat{m} \times \mathrm{d}F_n. \tag{3.23}$$

Note that $\vec{M}_n$ is a function of γ_2 and $\dot{\gamma}_2$. The moment produced by the torsional spring and damper (namely, the flexible joint itself) is evaluated as

$$\vec{M}_{(S+D)} = [K_S(\gamma_1 - \gamma_2) + K_D(\dot{\gamma}_1 - \dot{\gamma}_2)]\hat{k}, \tag{3.24}$$

where K_S and K_D are the spring and damper coefficients used to model the flexible rowing joint.

The total moment equation of the rigid fin relative to point A_1 is written as

$$\vec{M}_2 = \vec{M}_n + \vec{M}_{(S+D)} = I_p(\ddot{\gamma}_2 + \dot{\omega}_{C_z}), \tag{3.25}$$

where I_p is the effective inertia of the rigid fin (which contains the fin inertia and the added inertia, and is calculated base on a rigid plate moving in the water) and $\ddot{\gamma}_2$ is the angular acceleration of the second link. By solving Eq. (3.25), which is a second-order equation for γ_2, the dynamics of the pectoral fin with a flexible joint in the recovery stroke is fully described.

The hydrodynamic force transmitted to the servo arm can be obtained as $\vec{F}_{A_1} = F_n\hat{n} - m_p\frac{\mathrm{d}\vec{v}_p(s,t)}{\mathrm{d}t}$, where $\frac{\mathrm{d}\vec{v}_p(s,t)}{\mathrm{d}t}$ can be evaluated once γ_2 and $\dot{\gamma}_2$ are solved from Eq. (3.25). The total force exerted by the arm on the robot body is

$$\vec{F}_h = F_{h_x}\hat{\imath} + F_{h_y}\hat{\jmath} = \vec{F}_{A_1}. \tag{3.26}$$

The moment applied by the fin on the body is represented as

$$\vec{M}_h = M_{h_z}\hat{k} = c_p\hat{j} \times \vec{F}_{A_1}. \tag{3.27}$$

By substituting Eqs. (3.26), (3.27) into Eqs. (3.5)-(3.7), the dynamics of the robotic fish utilizing flexible rowing joints are fully described.

The presented model applies to the case where the robotic fish is free-swimming. The coupled body and fin motions introduce significant complexity in evaluating the fin-generated hydrodynamic force and moment. Alternatively, one could assume an anchored robot body when evaluating the fin-produced force and moment, as often adopted in the literature for similar problems [2, 19, 29]. While the latter simplification, also adopted in the simulation part of this paper, introduces modeling error, the error is typically acceptable considering the much larger fin velocity comparing to the velocity of the robot itself.

3.4 Experimental Model Validation

3.4.1 Robotic Fish Prototype and Experimental Setup

To evaluate the proposed flexible rowing joint mechanism and validate the presented dynamic model, we conduct experiments on a free-swimming robotic fish prototype. The robot is designed to swim on the surface and is slightly positive buoyant with about 15% of its height above water (as opposed to the neutrally buoyant assumption for dynamic modeling). Due to the relatively slow pectoral fin-actuated locomotion, the effect of tank walls and surface waves is contemplated to be negligible in this work. The body of the robotic fish is designed in SolidWorks and 3D-printed. Both the design schematic and the actual prototype are shown in Figure 3.7. This prototype is

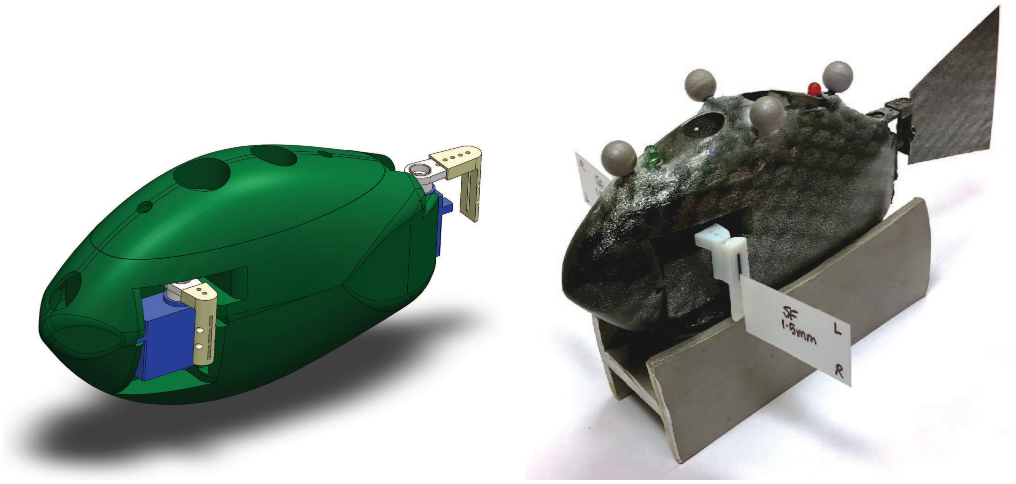

(a) (b)

Figure 3.7: Robotic fish prototype: (a) Designed SolidWorks model; (b) 3D-printed robotic fish body along with mounted fins.

about 15 cm long, 8 cm high and 4.6 cm wide without the pectoral and caudal fins, and weighs close to 0.3 kg. The robotic fish utilizes a pro mini microcontroller board from Arduino to realize the control of the three servos. A power converter printed circuit board (PCB) is specifically designed for this robotic fish. Three waterproof servos (Traxxas 2065) are utilized to actuate the fins, although tail actuation is not included in this study. The servomotors are programmed to rotate each pectoral fin according to

$$\gamma_1(t) = \gamma_A \sin(\omega_\gamma t) + 90^\circ, \tag{3.28}$$

with γ_A and ω_γ denoting the amplitude (in deg) and the angular frequency of fin actuation, respectively. The actual pectoral fins are made of a polypropylene sheet with 0.5 mm thickness and Young's modulus of approximately 2 GPa, which is considered to be almost rigid.

The experiments are conducted in a tank that measures 2 feet wide, 6 feet long, and 2 feet deep. The tank is equipped with a motion capture system from NaturalPoint, which contains four Optitrack Flex 13 cameras along with the Motive software to capture the motion of the robotic fish. The experimental setup is shown in Figure 3.8. Two types of experiments, forward swimming and

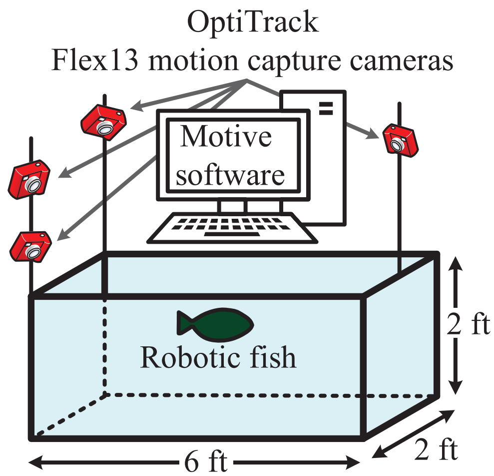

(a)

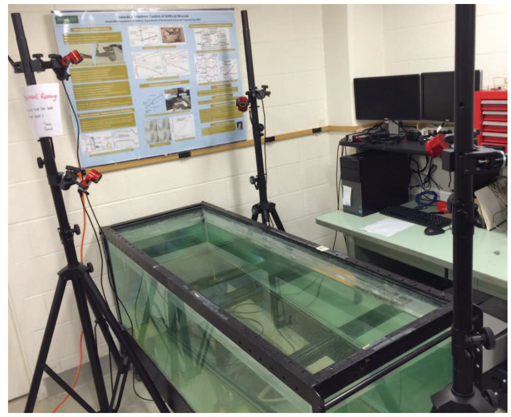
(b)

Figure 3.8: Experimental setup: (a) Schematic; (b) actual.

turning, are performed to evaluate the dynamic model. We let the robotic fish swim for some time (approximately 30 seconds) to reach the steady-state motion, and then video-tape its swimming. For example, in the forward swimming case we record the time it takes for the robot to swim a distance of 50 cm. The experiment for each setting is repeated 10 times. Finally, we analyze the captured videos to extract the steady-state speed for the forward swimming, and turning radius and period for the turning motion.

3.4.2 Parameter Identification

The parameters for the dynamic model are measured directly or calculated based on measurements and are listed in Table 3.2. The body inertia about z-axis is evaluated as $I_z = \frac{1}{5}m_b(a^2+c^2)$, where $a = \frac{\text{Body length}}{2}$ and $c = \frac{\text{Body width}}{2}$ are the semi-axis lengths [28]. Even though the robotic fish body (with all its internal components) is not homogeneous, later experimental results show that the aforementioned inertia formula produces a satisfactory approximation to the reality. The wet surface area, added masses, and added inertia are calculated considering an prolate spheroid accelerating in the fluid [28, 88].

Table 3.2: Identified Model Parameters

Component	Parameter	Value	Unit
Body	Mass (m_b)	0.295	Kg
	Inertia (I_z)	4.26×10^{-4}	Kg/m^2
	$-m_{a_x}$	0.095	Kg
	$-m_{a_y}$	0.1794	Kg
	$-I_{a_z}$	2.7×10^{-5}	Kg/m^2
	Wet surface area (S_A)	0.0325	m^2
	Drag coef. (C_D)	0.42	–
	Lift coef. (C_L)	4.86	–
	Moment coef. (C_M)	7.6×10^{-4}	Kg/m^2
Fin	Length (S)	0.043	m
	Depth (C)	0.025	m
	Servo arm lenght (l_1)	0.01	m
	Effective mass (m_p)	0.0194	Kg
	Effective inertia (I_p)	3.49×10^{-6}	Kg/m^2
	Distance from body center c_p to servo base,	0.025	m
	Water density (ρ)	1000	Kg/m^3

The robotic fish drag and lift coefficients, C_D, C_L, and C_M, are empirically identified using the data collected when the robotic fish is equipped with rigid joints for the pectoral fins. With the rigid joints, the power stroke and recovery stroke need to have different fin speeds, in order to produce a net thrust [21]. This ratio is denoted as $\frac{P}{R}(\frac{\text{Power stroke speed}}{\text{Recovery stroke speed}})$, which is equal to 1 for the symmetric fin-beating pattern. In this paper, experiments are conducted for the cases of $\frac{P}{R}$ = 2, 3, 4, and 5. The experimental results for both forward and turning swimming motions of the robotic fish with $\frac{P}{R}$ = 2 are used in the body parameter identification. Turning is realized by actuating one pectoral fin only. In particular, these parameters are tuned to match the forward velocity, turning radius, and turning period obtained in simulation with the experimental measurement when two different power stroke speeds are used, completing the power stroke in 0.5 s and 0.3 s, respectively. The fin-beat amplitude is set to γ_A = 25 deg. The resulting coefficients are $C_D = 0.42$, $C_L = 4.86$, and $C_M = 7.6 \times 10^{-4}$ Kg/m^2. These parameters are then used in independent model validation for all other cases using the flexible rowing joint.

Among all the rowing joints mentioned in Table 3.1, joint “JR1” results in the highest forward velocity. Without the loss of generality, this case is chosen to illustrate the model validation performance. To identify the spring and damper coefficients, K_S and K_D are tuned to match the forward swimming velocity of the robotic fish obtained in simulation with the experimental measurements for fin-beat frequencies of 0.75 Hz, 1 Hz and 1.5 Hz. The coefficients are identified $K_S = 6.34 \times 10^{-4}$ N·m and $K_D = 9.98 \times 10^{-5}$ N·m·s. These parameters are then used for model validation for various other cases involving the same joint.

3.4.3 Comparison between Flexible and Rigid Joints

Before presenting the model validation results, we first compare the performance of flexible rowing joints with that of a rigid joint (where the pectoral fins are connected to the servos with a rigid connection). For the rigid joint case, we have the different power and recovery stroke speeds, as mentioned in Section 3.4.2, so that the robotic fish can have a net thrust. Figure 3.9(a) shows the experimental results on the forward swimming velocities of the rigid joint case with $\frac{P}{R}$= 1, 2, 3, 4, 5, the case of the flexible feathering joint from [86], and the flexible rowing joint JR1, over different power stroke times. Figure 3.9(b) presents these results in terms of the effective fin-beat frequencies. The fin-beat frequency means $\frac{1}{T}$, where T denotes the period of each fin-beat cycle (power and recovery stroke combined) and the servos are programmed to run up to the limit of 200 °/sec. This maximum speed corresponds to the rightmost point in each curve in Figure 3.9(b). From Figure 3.9, we can conclude that, overall, the velocity performance of the flexible rowing passive joint significantly outperforms the rigid joint case.

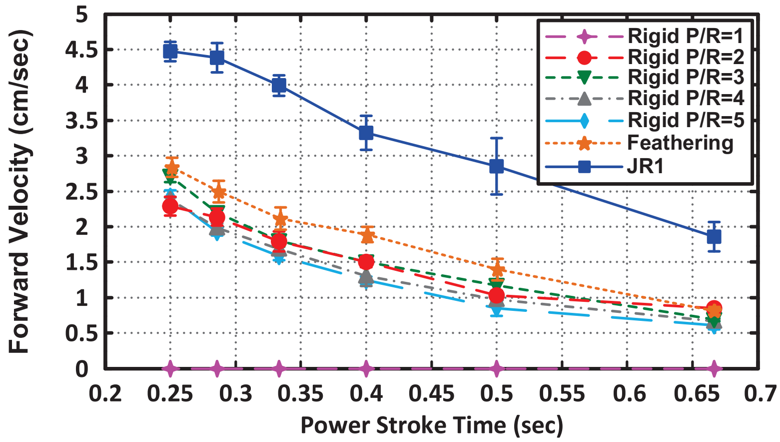

(a)

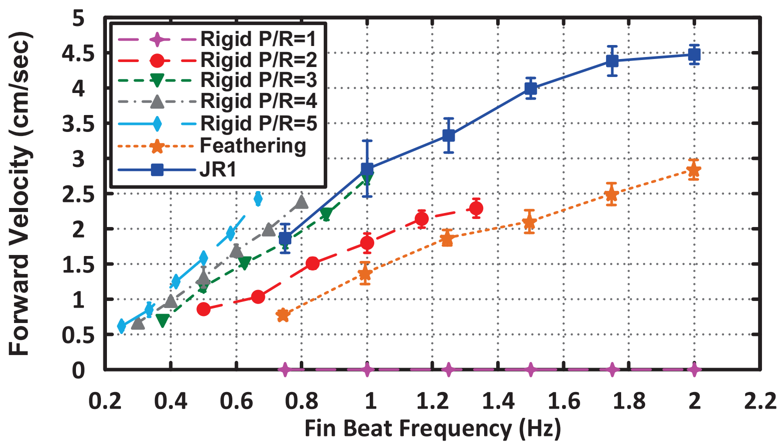

(b)

Figure 3.9: Experimental results of the forward swimming velocity versus (a) power stroke time, and (b) effective actuation frequency, for the cases of rigid joint and flexible rowing joint.

3.4.4 Dynamic Model Validation

3.4.4.1 Dynamic characteristics of pectoral fins

Before presenting experimental results that validate the dynamic model, we first present simulation results based on the experimentally identified model, to shed insight into the dynamic characteristics of the pectoral fins with flexible joints, as well as their effects on the robotic fish body. In the interest of brevity, we have only included the plots for one case (joint JR1 with fin-beat frequency of 1 Hz, where both fins are actuated). Figure 3.10(a) shows the time history of the pectoral fin and servo arm angles in one beat cycle. It is interesting to note that, while the pectoral fin angle follows closely the motor shaft angle during much of the power stroke, the "detachment" starts shortly after the servo passes the 90° during the power stroke, which is due to the inertial effect of the fin when the servo arm starts decelerating. Similarly, the difference between the two angles shrinks down to zero before the recovery stroke ends. Figure 3.10(b) shows the angle of attack in power and recovery strokes of one beat cycle, assuming that the robotic fish body is anchored. Figure 3.10(c) shows the total force exerted on the body by pectoral fins in the x-direction (F_{h_x}). Note that the mean value of the positive thrust is approximately 4 times larger than the mean value of negative thrust. The total hydrodynamic force in the y-direction (F_{h_y}) and the total hydrodynamic moment (M_{h_z}) are zero in this case due to the left-right symmetry in paired pectoral fin flapping. Finally, Figure 3.10(d) shows the surge velocity of the robotic fish (V_{C_x}) from the simulation. Again, the sway (V_{C_y}) and yaw (ω_{C_z}) components of the robotic fish velocities are zero due to the symmetry in fin-beat flapping. It can be seen that, starting at rest, the robot takes approximately 11 seconds to reach the steady-state.

3.4.4.2 Anchored experiments

To validate the proposed dynamic model, two sets of experiments are conducted on the robotic fish. During the first set of experiments, the robotic fish body is anchored using a bracket and the angle of the pectoral fin (γ_2) is measured with respect to $\hat{\imath}$, the robot's heading direction. The motion of the pectoral fin is captured from above, using a Casio Exilim (EX-FH25) high-speed camera at 40 frames per second. Figure 3.11 compares the measured maximum values of the rowing angle during the recovery stoke in both simulation and experiments at different fin flapping frequencies, when the robotic fish body is anchored. It can be seen that the model is able to capture the rowing angle well for all frequencies up to 1.75 Hz. For the case of 2 Hz, the noticeable

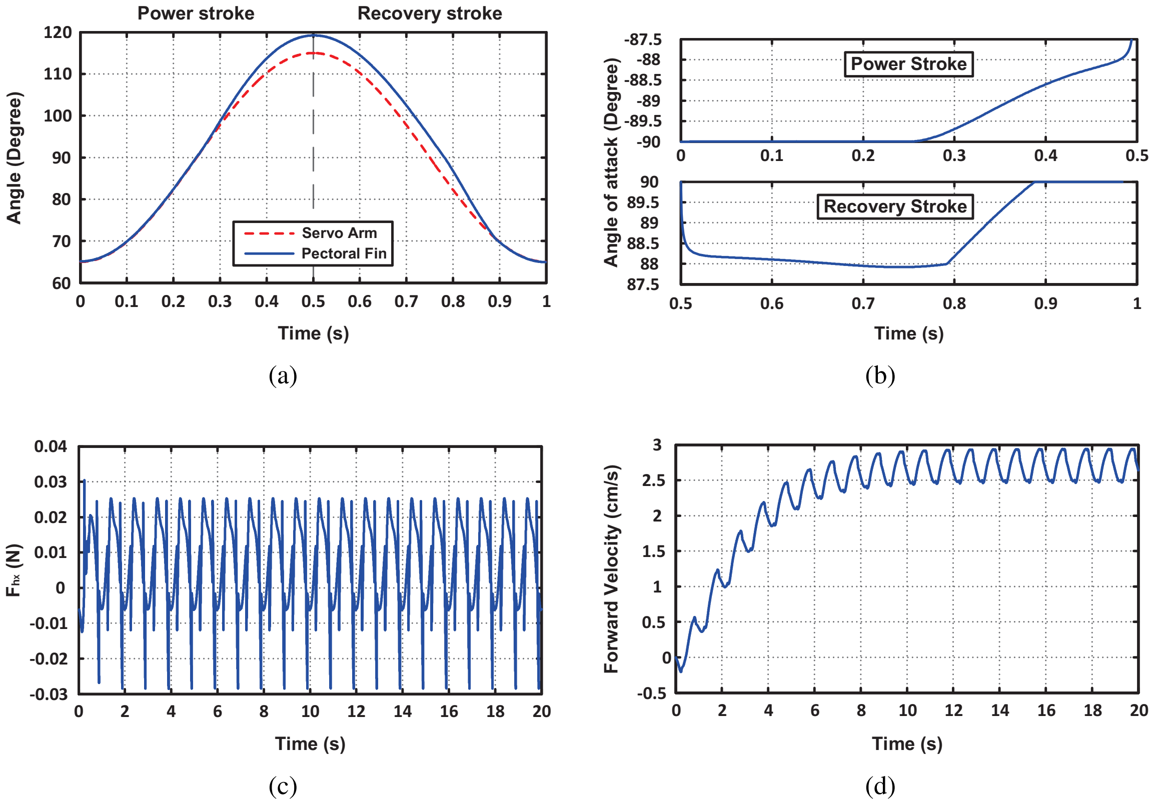

Figure 3.10: With fin-beat frequency of 1 Hz: (a) Variation of the pectoral fin and servo arm angle for one movement cycle, (b) Variation of the pectoral fin angle of attack for one movement cycle, (c) Variation of the total hydrodynamic force exerted to robotic fish body in x-direction (F_{h_x}) versus simulation time, (d) Variation of robotic fish velocity in x-direction (V_{C_x}) versus simulation time.

discrepancy between the model prediction and the measurement is likely caused by the constraints in fabrication, were the actual pectoral fin angle goes beyond the servo angle in the power stroke, ($\gamma_1 \neq \gamma_2$), due to the larger hydrodynamic loading on the pectoral fin.

Figure 3.12 compares the measured time-dependent pectoral fin angle (γ_2) during the recovery stroke and the corresponding model prediction for the case of 1 Hz actuation. Here, we show the frames every 0.1 sec during the recovery stroke. Overall there is a good match between the model prediction and experimental measurement. The prediction error is slightly larger at the beginning and the end of the cycle, which is attributed to the transition from/to the power stroke, where the mechanical stopper is in effect.

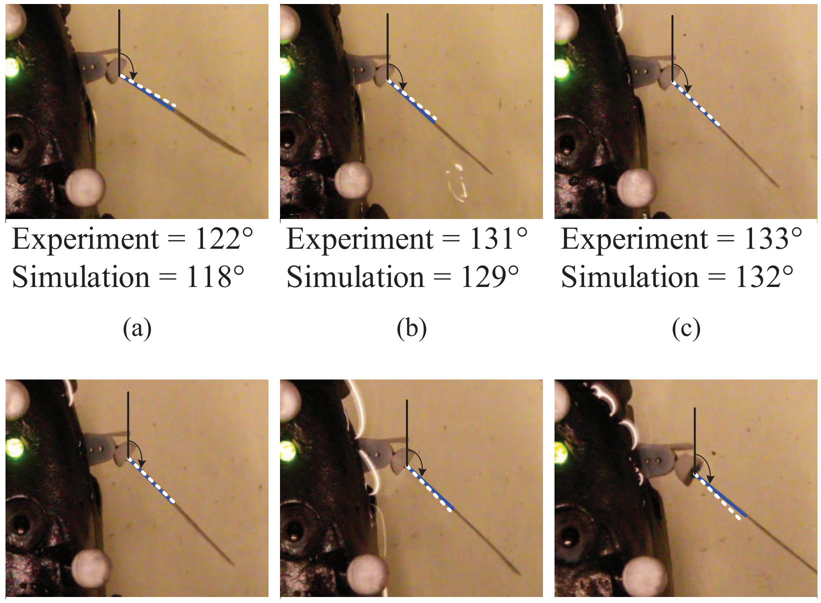

Experiment = 122° Simulation = 118°

(a)

Experiment = 131° Simulation = 129°

(b)

Experiment = 133° Simulation = 132°

(c)

Experiment = 135° Simulation = 135°

(d)

Experiment = 133° Simulation = 135°

(e)

Experiment = 128° Simulation = 133°

(f)

Figure 3.11: Comparison between model prediction (white dashed line) and experimental measurement (blue solid line) of the maximum rowing angle during the recovery stroke, with fin-beat frequencies of (a) 0.75 Hz, (b) 1 Hz, (c) 1.25 Hz, (d) 1.5 Hz, (e) 1.75 Hz, and (f) 2 Hz. The black vertical line indicates the robotic fish heading direction, the green dotted line shows the servo arm direction and the right pectoral fin is shown.

3.4.4.3 Free-swimming experiments

For the second set of experiments, the robotic fish swims freely in the tank, including both forward swimming and turning that are enabled with the pectoral fins utilizing the flexible rowing joints. Figure 3.13 shows the comparison between model prediction and experimental measurement of the forward swim velocity at different fin-beat frequencies. Figures 3.14 and 3.15 show similar comparisons on the turning radius and turning period. From Figure 3.14, the turning period drops with the frequency, which is expected. The simulation results in Figure 3.15 suggest that the turning radius has negligible dependence on the frequency, which is supported by the experimental results, where the mean values of the measured radius stay around 23-24 cm across all frequencies. The discrepancy between the simulation and experimental results in Figure 3.15 is largely attributed to

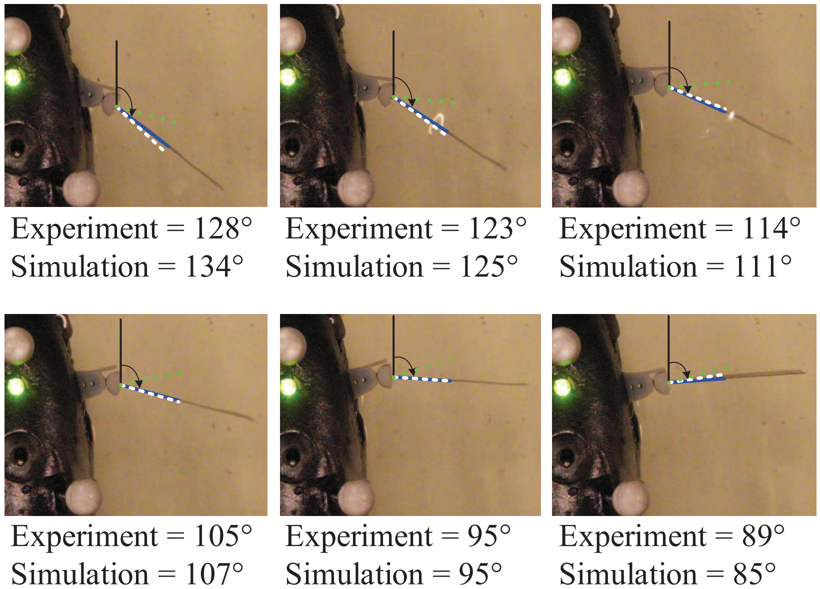

Figure 3.12: Comparison between experimental measurement of the time-dependent recovery stroke angle with model predictions. The pectoral fin beats at 1 Hz. The blue solid line and white dashed line imply the experimental measurement and model prediction, respectively, and the green dotted line shows the servo arm direction.

the challenge in measuring precisely the turning radius in experiments – the robot does not track closed orbits for each turn, which could be due to the disturbances from the interactions between the water and tank walls. The results of Figures 3.13-3.15 show that the proposed model is able to capture the motion of the robotic fish with flexible rowing joints very well. In particular, for the tested frequency range, the forward swimming velocity increases with the fin-beat frequency. In the turning case, the turning period (the time it takes to complete one turn) drops with the increasing fin-beat frequency, which matches one's intuition.

3.5 Effect of Flexible Joint Length and Stiffness

In this section, we investigate the impact of two design parameters for the flexible joint, its length and stiffness, which will allow further validation of the proposed model and demonstrate its potential use for design optimization. As described in [91], the torsional spring constant of a flexible

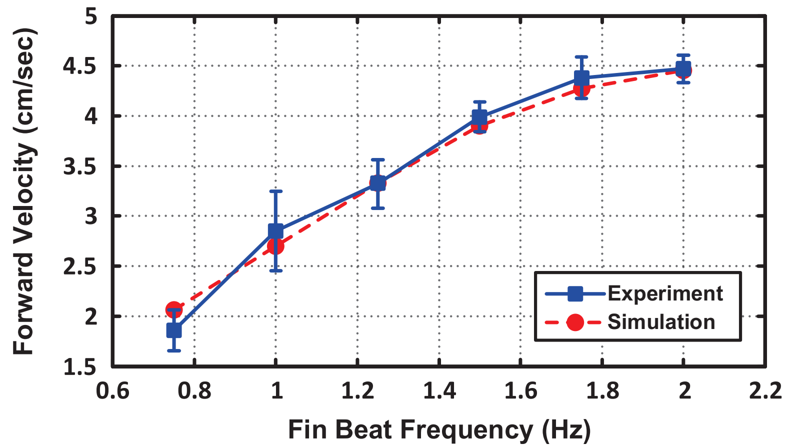

Figure 3.13: Case of rowing joint (JR1): Comparison between the model-predicted and measured forward swimming speed, for different fin-beat frequencies.

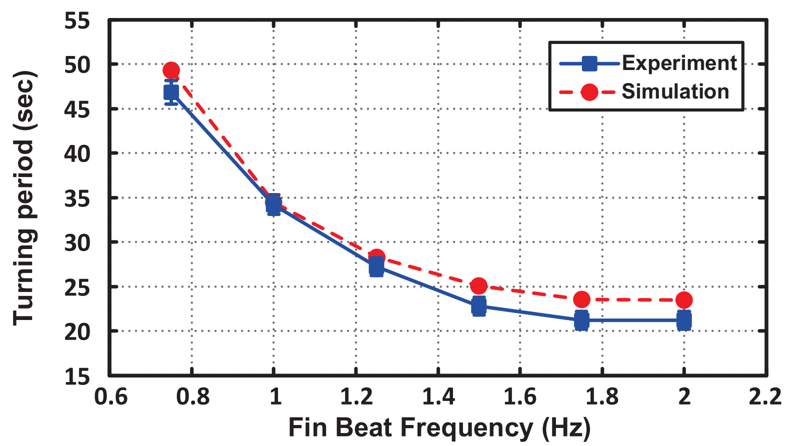

Figure 3.14: Case of rowing joint (JR1): Comparison between the model-predicted and measured turning period, for different fin-beat frequencies.

material can be evaluated as

$$K_S = \frac{Edh^3}{12l}, \tag{3.29}$$

where h is the thickness, l is the length, d is the width (depth), and E is the Young's modulus of the flexible material. The damper coefficient K_D can be evaluated as $K_D = \kappa K_S$, where κ is a proportional constant. So the spring constant changes with both dimension and stiffness of the flexible part of the passive joint.

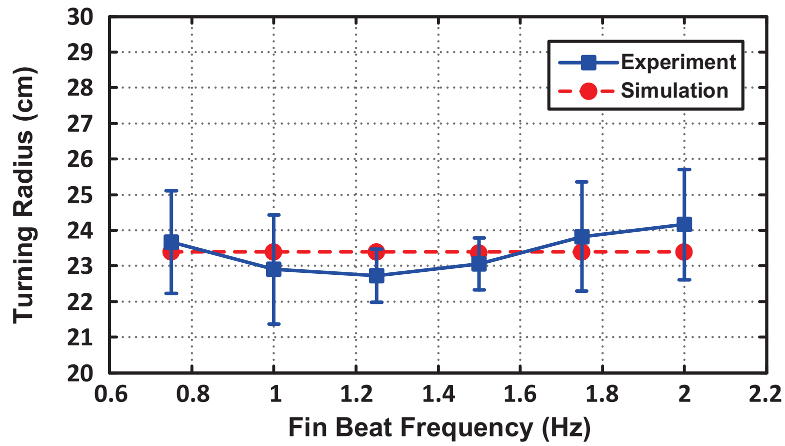

Figure 3.15: Case of rowing joint (JR1): Comparison between the model-predicted and measured turning radius, for different fin-beat frequencies.

We have chosen three different values for the length of the flexible rowing joint made of FLX980 material, 0.5 mm, 1 mm and 1.5 mm (Joints JR1, JR2, and JR3 in Table 3.1). The spring and damper constants for JR2 and JR3 are calculated using Eq. (3.29), where the Young's modulus (E) and κ values are kept the same as the ones derived from the parameters K_S and K_D for JR1. Figure 3.16 shows the model prediction and experimental results on the forward swimming velocity at different fin-beat frequencies, for all three joints. The joint JR1 has the best performance among the three joints for higher fin-beat frequencies. For lower frequencies (up to 1.25 Hz), joint JR3 (most flexible among the three) has a better performance. We can see that the model is able to effectively capture the joint length-dependence of the forward swimming velocity for all cases. While the experimental limit for the actuation frequency is 2 Hz, we have extended the simulation results to fin-beat frequency of 3 Hz in order to capture the optimal frequency of each joint. The forward swimming speed will drop after reaching this optimal frequency.

Finally, we compare the performance of flexible joints with different material stiffness. Two flexible joints with identical dimensions, JR1 made of FLX980 and JR4 made of DM9850 (stiffer), are used in the comparison. The spring and damper coefficients for JR4 are identified to be $K_S =$

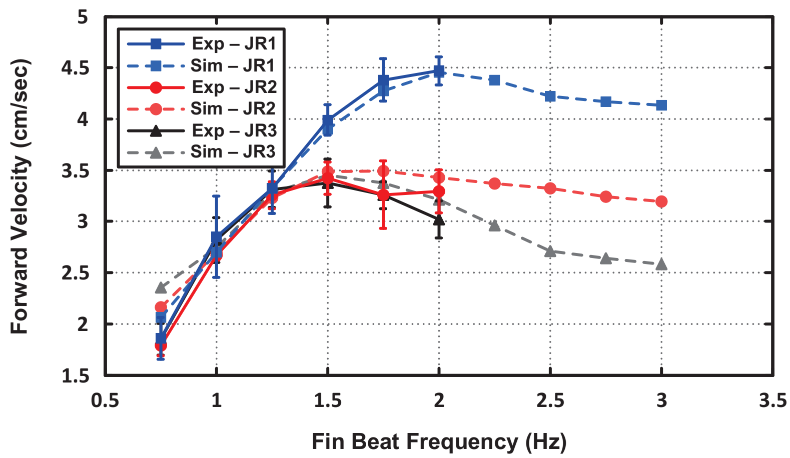

Figure 3.16: Model prediction and experimental measurement of the forward swimming velocity of the robotic fish with the use of three flexible joints (all made of FLX980) with different lengths.

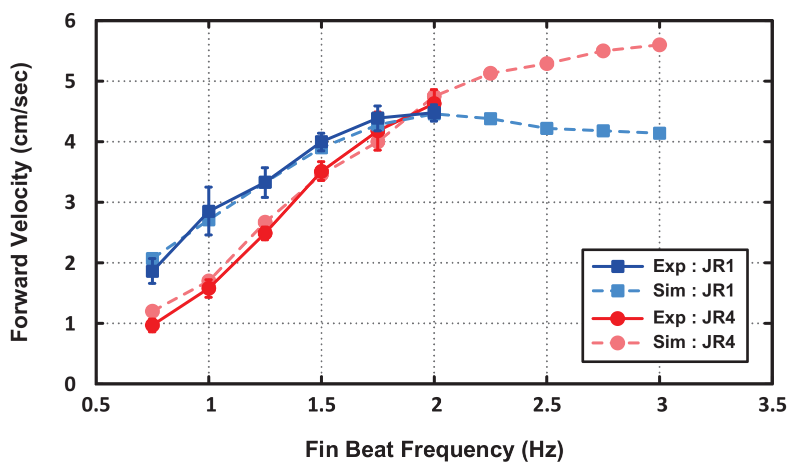

Figure 3.17: Model prediction and experimental results of the forward swimming velocity of the robotic fish with the use of two flexible joints with different stiffness values.

4.38×10^{-3} N $\cdot$ m and $K_D = 9.34 \times 10^{-4}$ N $\cdot$ m $\cdot$ s using the same method described in Section 3.4.2, and are used for model predictions for all other cases. Figure 3.17 shows the comparison of forward swimming speed between the two cases. Again, it can be seen that there is a good match between model predictions and experimental data. For the lower frequencies, the joint JR1 outperforms JR4, while JR4 is the winner for the higher frequencies. Again we have extended the simulation results to higher frequencies to better capture the performance trend of the joints.

3.6 Mechanical Efficiency

Robot efficiency, defined as the ratio of useful work for propulsion over total consumed energy, is of great relevance to practical operation of the robot. Mechanical work done by fins to the surrounding water, energy used for powering electronics, electrical losses, and frictional losses, among others, all contributed to the total consumed energy. Mechanical work is arguably the most significant source of energy expenditure, and therefore, it is important to understand how the design of pectoral fin joints influences the mechanical efficiency of the robot. In this section, we use the validated dynamic model to evaluate the propulsive efficiency of the robotic fish swimming with pectoral fins that use the flexible rowing joints. The mechanical efficiency during steady-state swimming is calculated as [5, 92, 93]

$$\eta = \frac{W_b}{W_T}, \tag{3.30}$$

where W_b is the amount of useful work needed to propel the robotic fish and W_T is the total work done by the pectoral fins during each fin-beat cycle. We call this the mechanical efficiency since it does not consider other energy losses, such as the electrical power used for running the electronics or frictional losses in motors and gears. The useful work W_{b_1} can be calculated as follows [92, 93],

$$W_{b_1} = \int_{t_0}^{t_0+T_0} F_{\text{Thrust}}(t) V_C(t) \mathrm{d}t \tag{3.31}$$

where F_{Thrust} is the x-component of the total fin-generated hydrodynamic force exerted on the robotic fish body (F_{h_x}), $V_C(t)$ is the velocity of the robotic fish body projected into the $x-$direction, and T_0 denote the total duration of each fin-beat cycle. In this paper we take an alternative approach that uses product of the mean thrust and the mean velocity at the steady-state. When the robotic fish is at the steady-state and cruises with a constant speed $V_{C_{\text{mean}}}$, its mean thrust is balanced by its

Table 3.3: Comparison between the two methods of computing W_b.

Frequency (Hz)	W_{b_1}	W_{b_2}	$\frac{W_{b_1}-W_{b_2}}{W_{b_2}}(\%)$
0.75	0.112	0.114	1.75
1	0.1887	0.1939	2.68
1.25	0.2826	0.2888	2.15
1.5	0.3787	0.3905	3.02
1.75	0.4281	0.4383	2.33
2	0.4233	0.4391	3.6

(mean) drag force, and thus

$$F_T = \frac{1}{2}\rho V_{C_{\text{mean}}}^2 S_A C_D. \tag{3.32}$$

which results in the following expression of W_{b_2}

$$W_{b_2} = \frac{1}{2}\rho V_{C_{\text{mean}}}^3 S_A C_D T_0. \tag{3.33}$$

As shown in Table 3.3, the values of W_b computed with these two methods are actually very close to each other (with error less than 4%). Given that the second method of evaluating W_{b_2} ignores the oscillatory nature of the thrust and velocity and is thus simpler, it is adopted in the efficiency analysis for the remainder of this paper.

The total work done by the paired pectoral fins, W_T, is obtained as

$$\begin{aligned} W_T &= 2\int_{t_0}^{t_0+T_0} \max\{0, \int_0^S \mathrm{d}F_n(s,t)\cdot\vec{v}_p(s,t)\}\mathrm{d}t \\ &= 2\int_{t_0}^{t_0+T_0} \max\{0, \int_0^S \frac{1}{2}C_n\rho C|\vec{v}_p(s,t)|^2\cdot\vec{v}_p(s,t)\mathrm{d}s\}\mathrm{d}t, \end{aligned} \tag{3.34}$$

where t_0 represents the beginning of a fin-beat cycle, "$\cdot$" denotes the inner product. Note that

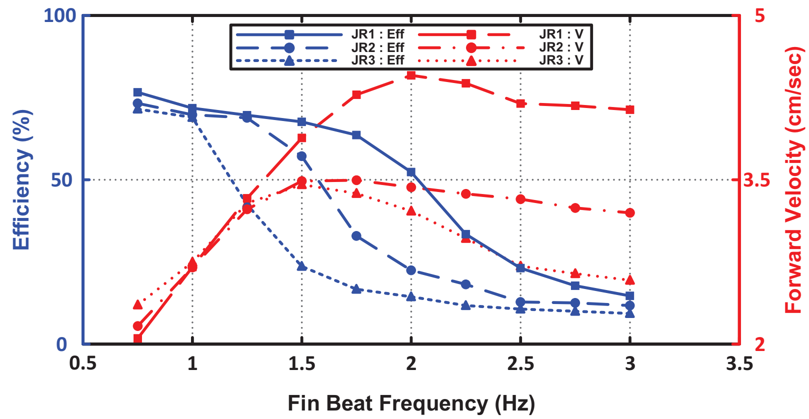

Figure 3.18: Calculated mechanical efficiency and forward velocity of different flexible rowing joints at different fin-beat frequencies.

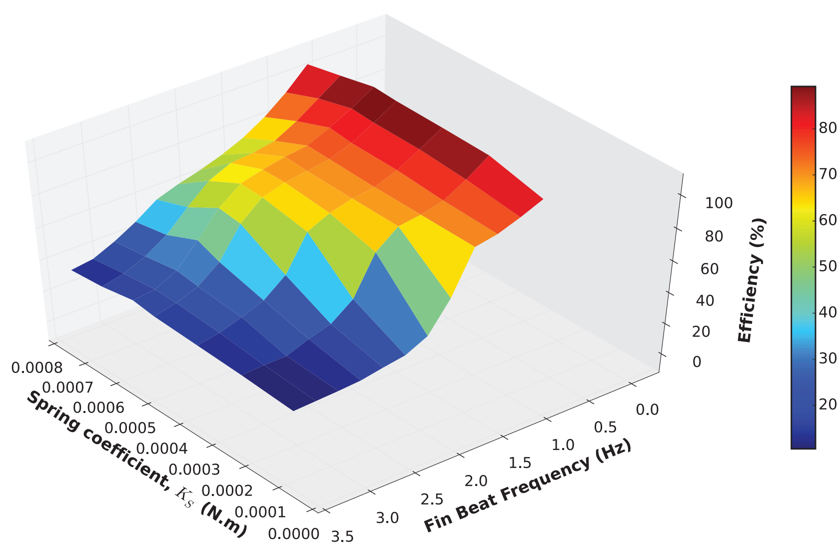

Figure 3.19: Calculated mechanical efficiency versus fin-beat frequency and spring constant of the flexible joint.

at some time instants t, the instantaneous mechanical power exerted by pectoral fins on water could be negative; however, since the servos cannot reclaim this energy from water, we treat the instantaneous power at such a t as zero, which explains the operator $\max\{0,\cdot\}$ in Eq. (3.34). Note that even at the steady-state, the actual velocity is not a constant; instead, it periodically fluctuates around some value. Therefore, $V_{C_{\text{mean}}}$ in Eq. (3.32) is evaluated by the distance traveled over N cycles ($N = 10$) divided by NT_0.

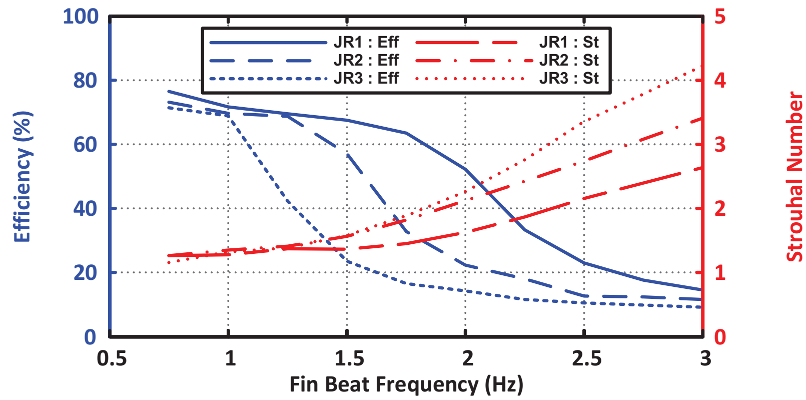

(a)

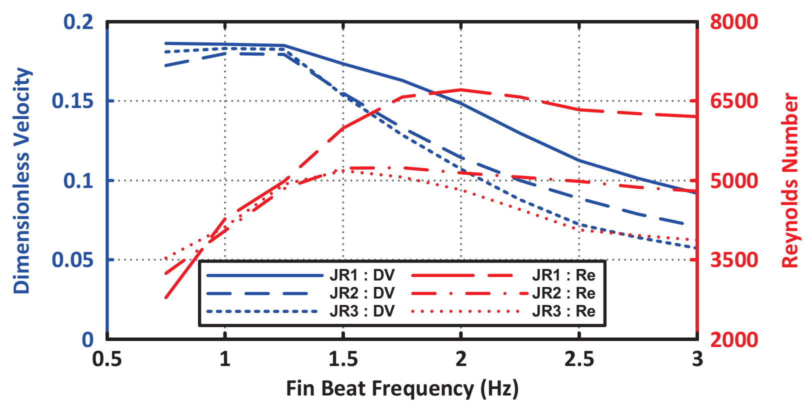

(b)

Figure 3.20: Comparison of non-dimensionalized parameters for joints JR1, JR2, and JR3 at different fin-beat frequencies: (a) Calculated mechanical efficiency and Strouhal number, (b) Dimensionless velocity and Reynolds number.

Figure 3.18 shows the calculated efficiency, along with the corresponding swimming velocity, for the joints JR1, JR2 and JR3. The efficiency of the joint JR1 is higher than the other two and overall the efficiency is higher for lower fin-beat frequencies. Figure 3.18 reveals interesting trade-off between the speed performance and mechanical efficiency. In particular, for a given joint design, with a higher frequency, the speed is higher but at the cost of lower efficiency. Figure 3.19 shows the efficiency curve versus different fin-beat frequencies and spring constant values (k_S). This figure shows that the robotic fish performs more efficiently in lower fin-beat frequencies with stiffer flexible rowing joints up to a certain optimal stiffness ($K_S \approx 7 \times 10^{-4}$ N $\cdot$ m). For any joint stiffer or more flexible than this optimal amount, the efficiency starts to drop. Overall, Figures 3.18 and 3.19 indicate that the optimization of the flexible joint presents an interesting, multi-objective design problem that involves consideration of the joint stiffness, dimension, and the frequency of fin operation. The proposed dynamic model in this paper shows promise in addressing the optimal design problem.

Figure 3.20 provides a comparison of the non-dimensionalized parameters for joints JR1, JR2, and JR3 at different fin-beat frequencies. The non-dimensionalized parameters considered include the Reynolds number Re, the Strouhal number St, and the dimensionless velocity V_{DL}. Recall the Reynolds number $\mathrm{Re} = \frac{V_{C_{mean}} L}{\nu}$, where $V_{C_{mean}}$ is the swimming speed of the robot, L is the robotic fish length, and ν is the kinematic viscosity of water. The robotic fish length $L = 0.15$ m and $\nu = 10^{-6}$ m^2/s are used in the calculation. The Strouhal number is defined as $\mathrm{St} = \frac{fA}{V_{C_{mean}}}$, where f is the fin-beat frequency, A is the maximum excursion of the trailing edge for pectoral fin, and $V_{C_{mean}}$ is the swimming speed of the robot. We use $A = 2S \sin \gamma_A$, where S is the pectoral fin span length and γ_A is the fin flapping amplitude [27, 35]. The dimensionless velocity is defined as $V_{DL} = \frac{V_{C_{mean}}}{fL}$ [105].

It can be seen in Figure 3.20(a) that the efficiency shows clear inverse correlation with the Strouhal number. For example, JR1 demonstrates the highest mechanical efficiency among the three joints and has the lowest Strouhal number. For each joint, the Strouhal number increases while the efficiency drops when the frequency increases. Note that the Strouhal numbers for biological fish are usually in the range of 0.25-0.5 [35, 95, 96]. The Strouhal numbers presented here are higher than 1 and thus beyond the biological range. The reason is that the robotic fish used in this study is propelled purely by the pectoral fins, which results in low speeds and higher Strouhal numbers. Note that, from Figure 3.20(a), when the efficiency of the robotic fish gets higher, the Strouhal number gets closer to the biological range. On the other hand, Figure 3.20(b) shows

Table 3.4: Comparison of non-dimensionalized parameters.

Robotic fish	St	Re	V_{DL}
This work - JR1	1.27	4273	0.19
This work - JR2	1.35	4044	0.18
This work - JR3	1.32	4116	0.183
[35] with $\gamma_A = 30^\circ$	2.95	5925	0.042
[35] with $\gamma_A = 45^\circ$	2.96	8737	0.0621
[35] with $\gamma_A = 60^\circ$	7.76	4350	0.031
[21]	6.05	900	0.04
[86] - JF1	2.55	1744	0.078
[34]	0.94	10000	0.16

that the robotic fish demonstrates the highest dimensionless velocity when the Reynolds number is at the lower end. Comparing Figure 3.20(a) and 3.20(b) also suggests that there is a positive (negative, resp.) correlation between the mechanical efficiency (the Strouhal number, resp.) and the dimensionless velocity, which is expected given the definitions of the Strouhal number and the dimensionless velocity.

We have also compared our results with the results (all actuated at 1 Hz) from several pectoral fin-actuated robotic fish reported in the literature, as seen in Table 3.4. From the table, it can be seen that the Strouhal numbers achieved in this work are generally closer to the biological range than what was achieved in other reported work (with the exception of [34], which is slightly lower than our results). The dimensionless velocities achieved in this work are also the highest among all cases. These comparisons provide strong support for the effectiveness of the proposed approach.

3.7 Conclusion

While biological fish use sophisticated pectoral fin kinematics to achieve superior swimming and maneuvering performance [18, 106], the goal of this work is to achieve sound performance for robotic fish pectoral fins with simple structure and simple control. In particular, we have proposed a novel flexible, passive joint for rowing pectoral fins in robotic fish, and presented a dynamic model for the robotic fish equipped with such pectoral fin mechanisms. The flexible joint enables the pectoral fin to bend back passively along the fish body during the recovery stroke, to minimize the drag force, while maintaining the prescribed motion of the actuator during the power stroke. This design eliminates the need to have different actuation speeds for power and recovery strokes. Blade element theory is used to evaluate the hydrodynamic forces on the pectoral fins. The flexible joint is modeled as a pair of torsional spring and damper. To validate the dynamic model, we have conducted experiments involving both a configuration where the robotic fish is anchored and the fin bending angles are measured, and a free-swimming configuration, where forward swimming speeds and turning radii/periods at different fin-beat frequencies are measured. The performance of the proposed joint is also compared with a traditional rigid joint, to show the effectiveness of this design. The results showed a drastic improvement in the performance of the robotic fish. Multiple flexible rowing joints are used in the experiments to examine the influence of the flexible joint's length and stiffness on the robotic fish performance, and the experimental data match the model predictions well in all cases, which further supports the utility of the presented model in design optimization. Finally, with the aforementioned model, we have numerically evaluated the mechanical efficiency of the robotic fish and explore its dependence on the flexible joint stiffness and the operating frequency.

Chapter 4

Bio-inspired Flexible Joints with Passive Feathering for Robotic Fish Pectoral Fins

4.1 Introduction

Development of robotic fish has been inspired by unique characteristics of swimming in live fish and other aquatic animals, such as agility, maneuverability, and efficiency [2–4, 28, 30, 31, 95, 107–115]. Robotic fish change their body shape or flap different fins to generate propulsion [5, 27, 39, 51, 101, 116–119]. According to [11], based on the propulsors that fish use, their locomotion can be divided into two main categories: median/paired fin propulsion, and body/caudal fin propulsion. In this work, we consider the case where a robotic fish oscillates its paired pectoral fins to generate thrust. The pectoral fin propulsion provides good maneuverability and stability for robotic fish [80]. There are some studies dealing with robotic fish propelled by paired pectoral fins. Most of the early investigations employed rigid pectoral fins that were motor-driven to produce different fin motions [32, 35, 44, 55]. Several recent studies investigated the impact of flexible pectoral fins on robotic fish performance [21, 62]. In order to generate a net thrust, there are typically two strategies. The first strategy involves the use of multiple actuators for each pectoral fin, to provide

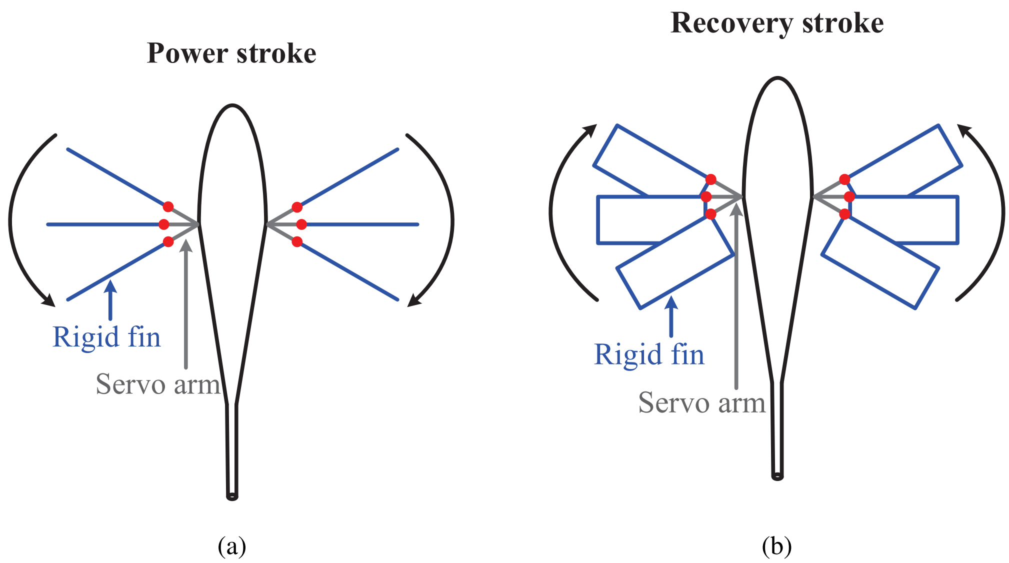

Figure 4.1: schematics of the drag-based labriform swimming mode, using flexible feathering joints (top view): (a) Power stroke, (b) recovery stroke. The flexible feathering joint is shown with a red circle.

combinations of different degrees of freedom, namely rowing, feathering and flapping, where the axes of rotation are vertical, transverse, and longitudinal, respectively. Although this strategy enables the mimicking of live fish pectoral fin motion, it results in large size and high energy consumption for robotic fish [35, 55]. An alternative actuation strategy is to use a single actuator per fin to maintain the small robot size, but employ different power and recovery stroke speeds to minimize the drag force during the recovery stroke. However, this method tends to significantly slow down the fish in the extended recovery stroke period [21]. This issue was addressed in [84], where the authors proposed a design of a passive joint for the rowing motion, which enables the pectoral fin to sweep back passively (along the same rowing axis) in order to minimize the drag force during the recovery stroke.

In this study, to more precisely mimic drag-based labriform swimming mode of live fish [11], we combine two different pectoral fin motions, rowing and feathering, realized with only a single actuator per fin, as illustrated in Figure 4.1. As discussed in [120, 121], a real fish rarely moves its pectoral fin by an exclusive rowing or feathering movement; instead, it uses a combination of these motions to move forward. The contribution of this paper is the design and modeling of a flexible, passively feathering joint that enables the robotic fish to mimic the drag-based labriform swimming mode. Here, the pectoral fin motion is divided into two phases, namely, power and recovery strokes. During the power stroke, the mechanical stoppers of the designed joints allow the paired fins to move backward with respect to the body, following a prescribed rowing motion. This would induce a drag force opposite to the moving direction of the fins, pointing in the forward direction. In the recovery stroke, the pectoral fin feathers passively while following the actuated rowing motion, which effectively reduces the drag force on the fin. The mechanism of the joints and how the stoppers work in each cycle are described in detail in Section 4.2. The proposed joint reduces the cost and complexity of the fin motion, comparing to adopting an active feathering fin [35, 55].

The dynamic model of the pectoral fin is developed based on blade element theory [5], where the joint is modeled as a pair of torsional spring and damper. With the consideration of the combined rowing and feathering motions, the 3D hydrodynamic forces are captured in the model. The model is then validated by conducting different experiments on a robotic fish. The performance of the robotic fish utilizing the flexible feathering joint is also compared with the case where differential actuation during power/recovery strokes is adopted along with a traditional rigid joint. The effect of the depth and stiffness of the flexible joint is further investigated using the dynamic model, which is also validated with experiments. Finally, the mechanical efficiency of the robotic fish is computed for flexible feathering joints for different spring constants and operating frequencies, which provides insight that is useful in optimizing the joint design and the frequency regime of fin flapping.

The remainder of this paper is organized as follows. In Section 4.2 the design and prototyping of the proposed flexible joint are described in detail. The dynamic model of the joint along with the model for robotic fish adopting such joints is presented in Section 4.3. In Section 4.4 the experimental setup is described and experimental results are provided along with the simulation results to validate the dynamic model. Section 4.5 is focused on the effect of joint depth and stiffness. Section 4.6 addresses the calculation of the mechanical efficiency of the robotic fish adopting the flexible joint. Finally, concluding remarks are provided in Section 4.7.

4.2 Design of Flexible Feathering Joint

This section covers the details of design and prototyping of the flexible feathering joint. As mentioned earlier, each pectoral fin follows a rowing motion prescribed by the servo motor, which actuates the proximal end of the fin symmetrically during the power and recovery strokes. Our primary goal is to minimize the drag force during the recovery stroke, by adding another degree of freedom to the pectoral fin, without utilizing any additional actuator. To accomplish this goal, a flexible feathering joint is designed to enable the pectoral fin feather passively when it is rowed back during the recovery stroke. This mode of swimming is called drag-based labriform swim, and is illustrated in Figure 4.1. In particular, the pectoral fin maintains the servo-prescribed rowing motion during the power stroke, to produce a maximum net thrust, while it rotates passively along the transverse axis (feathers) during the recovery stroke, to reduce the hydrodynamic drag on the fin.

The proposed feathering joint design is shown in Figure 4.2. The entire joint mechanism consists of a rigid servo arm connector that connects the whole joint/fin structure to the servo motor, a mechanical stopper, a fin mount and a rectangular flexible piece (shown in black in Figure 4.2(a) and (b)), serving as the feathering joint, which connects the fin mount structure to the servo arm

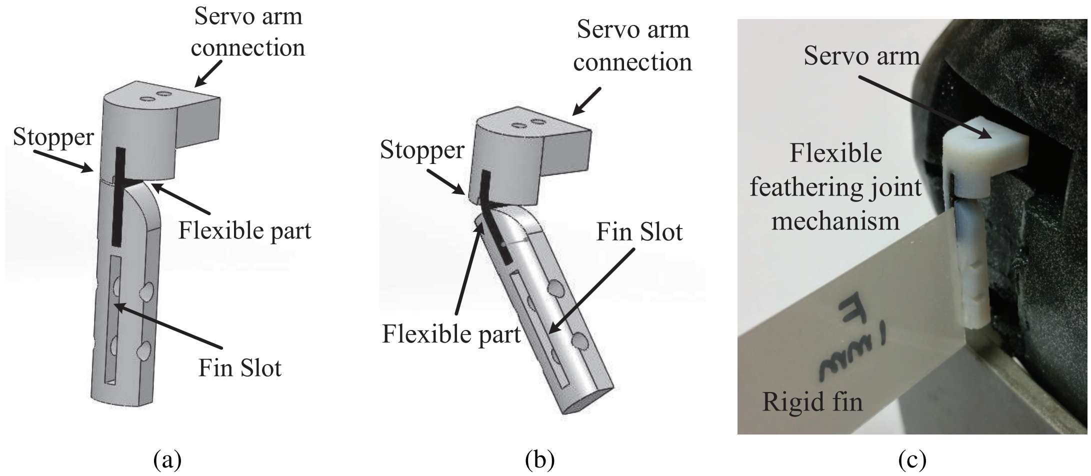

Figure 4.2: The proposed flexible feathering joint: (a) During the power stroke, the mechanical stopper prevents the fin from feathering, (b) during the recovery stroke, the fin rotates and tends to align with the horizontal surface, to reduce the drag force on the fin, and (c) 3D-printed feathering passive joint assembled on the robotic fish.

connector. During the power stroke, the mechanical stopper enable the pectoral fin to maintain the rowing motion prescribed by the servo motor, as shown in Figure 4.1(a) and Figure 4.2(a), while during the recovery stroke, the flexible joint enables the fin to feather passively and reduce the hydrodynamic drag force, as shown in Figure 4.1(b) and Figure 4.2(b).

Flexible feathering joints are prototyped using a multi-material 3D printer (Connex 350 from Object), which is capable of simultaneously jetting rigid and flexible materials, resulting in seamless integration of the pliable and rigid components of the flexible joint mechanism, as shown in Figure 4.2(c). All the rigid parts (servo arm connector and fin mount) are printed with the material RGD835 (VeroWhitePlus). Two different flexible materials, FLX980 (TangeBlackPlus), which is the most flexible material supported by the printer, and DM9850 (Digital Material 9850), which is stiffer than FLX980 but still flexible enough, are explored for the flexible part of the feathering joint structure. Other than different materials, it is also our goal to investigate the impact of joint dimensions on the propulsion performance. For this purpose, a total of four joints are printed, three using FLX980 and one using DM9850. All joints have width of 4 mm and thickness of 1 mm, to ensure adequate strength for surviving through extensive experiments. The three FLX980 joints have different values for their depth, 0.5 mm, 1 mm and 1.5 mm, while the DM9850 joint has a depth of 0.5 mm. Here the joint depth refers to the extent of the gap between the top and bottom rigid elements on the side opposite to the mechanical stopper. The gap is negligible on the stopper side. The four joints, with their different combinations of materials and depths, enable a compact set of experiments for validating the proposed dynamic model and revealing design trade-offs. The joints are referenced as follows. Joint "JF1", with FLX980 as the flexible material and depth of 0.5 mm, joint "JF2" with FLX980 as the flexible material and depth of 1 mm, joint "JF3" with FLX980 as the flexible material and depth of 1.5 mm, and finally, joint "JF4" with DM9850 as the flexible material and depth of 0.5 mm.

4.3 Dynamic Model of Fin-Actuated Robotic Fish Incorporating the Flexible Feathering Joint

4.3.1 Hydrodynamic Forces on the Fin

In this section, first we describe the use of blade element theory in representing the hydrodynamic force on the fin, for a given fin movement pattern, which is determined by the (yet to solve) dynamics of the flexible joint, namely, the feathering dynamics. The hydrodynamic force is then incorporated into the dynamic model for the feathering motion, which is captured via a pair of torsional spring and damper. Finally, the total hydrodynamic forces and moments resulting from the fin mechanism are used to develop the dynamic model for the robotic fish propelled by the fins.

Adapted from [5], the blade element theory is used to evaluate the hydrodynamic forces on the pectoral fins. For all these calculations, we assume an anchored robotic fish body. This assumption

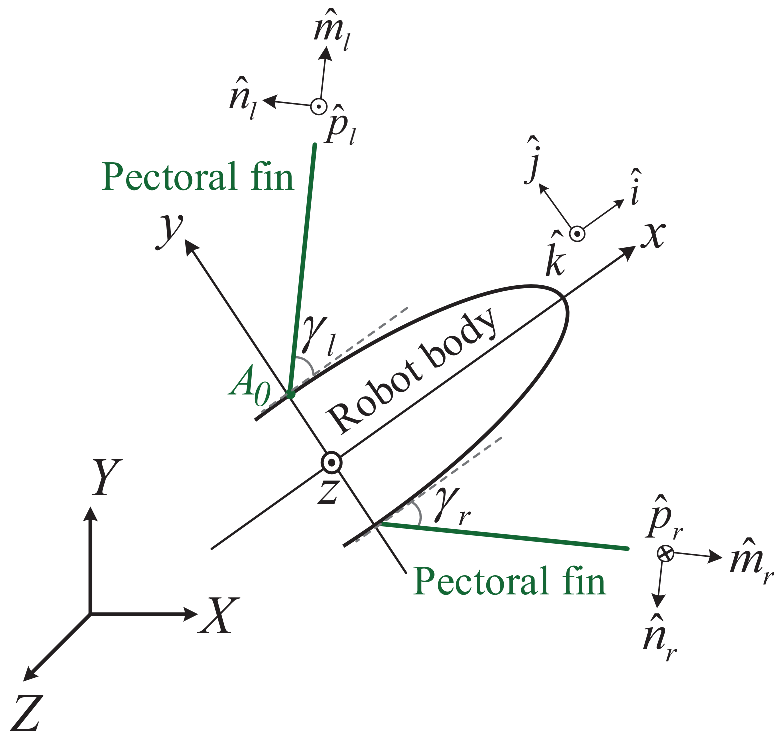

Figure 4.3: Top view of the robotic fish actuated by pectoral fins in planar motion.

is often adopted in the literature for similar problems [2, 19, 29]. While this simplification introduces modeling error, the resulting error is typically acceptable considering the much larger fin velocity comparing to the velocity of the robotic fish itself. For ease of calculation, the pectoral fin is considered to be rigid and rectangular with span length S and chord length (depth) C. Figure 4.3 shows the top view of a robotic fish, consisting of a rigid body and paired pectoral fins. $[X,Y,Z]^T$ indicates the inertial coordinate system and $[x,y,z]^T$ represents the body-fixed coordinate system, with corresponding unit vectors $[\hat{i},\hat{j},\hat{k}]$, which is attached to the center of mass of the robotic fish. We use $[\hat{m},\hat{n},\hat{p}]$ to denote the unit vectors of the pectoral fin coordinate system, where subscripts r and l are used to represent right and left fins, respectively. Here $\hat{m}$ is parallel and $\hat{n}$ is perpendicular to the pectoral fin and $\hat{p}$ is automatically formed by the right-hand orthonormal principle. The notation $\vec{r}_{c_p} = c_p\hat{j}$ denotes the vector pointing from the robotic fish center of mass to the pectoral fin servo motor base (point A_0).

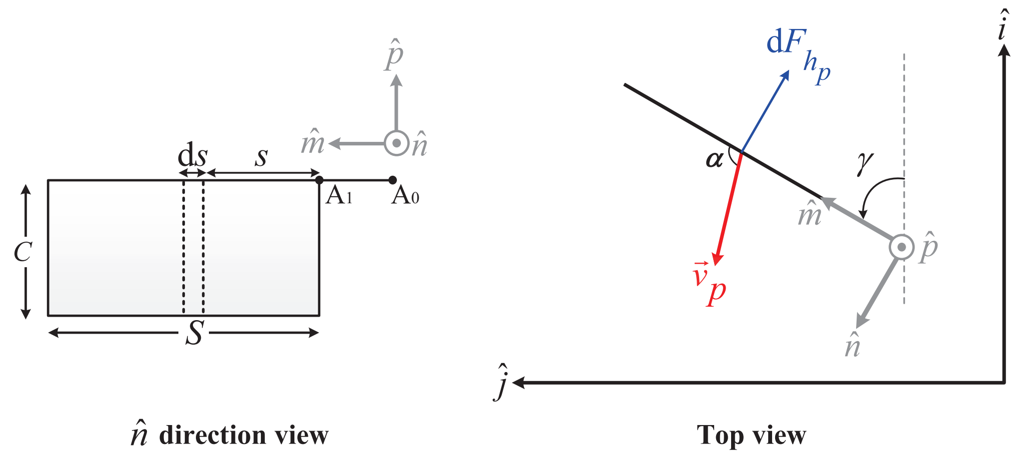

Figure 4.4: Illustration of a rigid, rectangular pectoral fin and its parameters, during the power stroke.

We divide the pectoral fin movement cycle into power and recovery strokes, and study each separately. During the power stroke, the pectoral fin undergoes a rowing motion prescribed by the servo motor; therefore, the fin plane stays vertical and the hydrodynamic forces are restricted to the horizontal plane, as shown in Figure 4.4. Here, all the calculations are done for the left pectoral fin, which can be extended to the right fin in a straightforward manner.

During the power stroke, the relation between the orthonormal unit vectors $[\hat{m}, \hat{n}, \hat{p}]$ and the body-fixed coordinate system is given by

$$\hat{m} = \cos\gamma\, \hat{i} + \sin\gamma\, \hat{j}, \tag{4.1}$$

$$\hat{n} = -\sin\gamma\, \hat{i} + \cos\gamma\, \hat{j}, \tag{4.2}$$

$$\hat{p} = \hat{k}. \tag{4.3}$$

where γ is the prescribed angle of the servo arm with respect to the body heading $\hat{i}$.

In blade element theory, the hydrodynamic force $\mathrm{d}F_{h_p}(s,t)$ on each defined blade element, ds, at time t, is calculated as

$$\mathrm{d}F_{h_p}(s,t) = -\frac{1}{2}C_n(\alpha(s,t))\rho|\vec{v}_p^2(s,t)|C\,\mathrm{d}s\ \hat{n}, \tag{4.4}$$

where ρ denotes the water density, $\vec{v}_p(s,t)$ is the velocity of each blade element of the pectoral fin, and C_n is the normal force coefficient, which is dependent on the angle of attack of the blade, $\alpha(s,t)$. Here, we consider $C_n = 3.4\sin\alpha(s,t)$, by utilizing an empirically evaluated model for insect wing which was used for a robotic fly [122] and robotic "boxfish" [63]. Even though insects (or robotic insects) fly in air while robotic fish swim in water, the associated fluid dynamics will have similar behavior if their Reynolds numbers are close. In particular, the Reynolds number of the robotic fish in this work is at the order of 10^3, which is close to the Reynolds number reported in [122] for the robotic fly (30-1000).

The velocity of each element, $\vec{v}_p(s,t)$, is expressed as

$$\begin{aligned}\vec{v}_p(s,t) &= v_{px}\,\hat{i} + v_{py}\,\hat{j} \\ &= \Big\{-(l_1+s)\dot{\gamma}\sin\gamma\Big\}\,\hat{i} + \Big\{(l_1+s)\dot{\gamma}\cos\gamma\Big\}\,\hat{j},\end{aligned} \tag{4.5}$$

where l_1 is the length of the servo arm.

The angle of attack of each blade element can be evaluated via

$$\tan\alpha = \frac{< v_p(s,t), \hat{n} >}{< v_p(s,t), \hat{m} >} = \frac{-v_{px}\sin\gamma + v_{py}\cos\gamma}{v_{px}\cos\gamma + v_{py}\sin\gamma}, \tag{4.6}$$

where $< \cdot,\cdot >$ denotes the inner product. With the anchored body assumption, it is easy to verify that the angle of attack is 90°.

The total hydrodynamic force acting on each pectoral fin is calculated by integrating the force

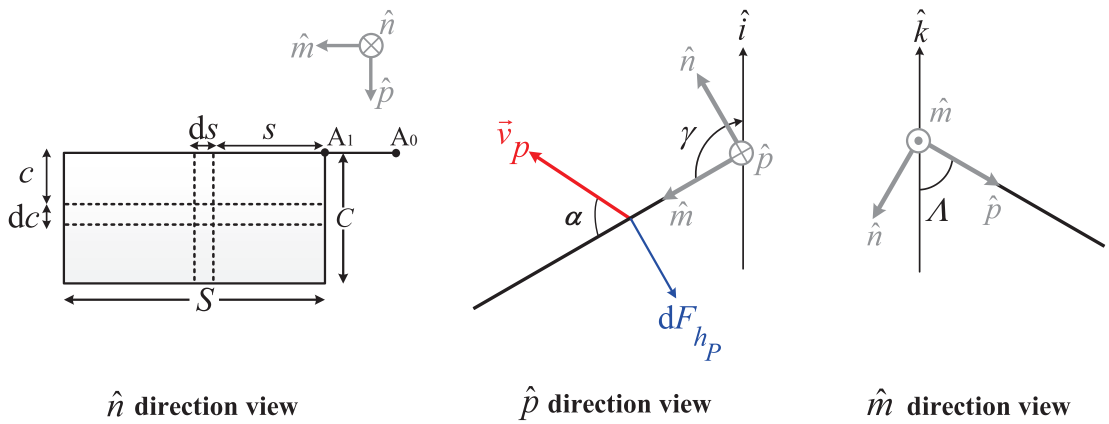

Figure 4.5: Illustration of a rigid, rectangular pectoral fin and its parameters, during the recovery stroke.

density along the span length of the fin

$$\vec{F}_{h_p}(t) = \int_0^S \mathrm{d}F_{h_p}(s,t). \tag{4.7}$$

On the other hand, during the recovery stroke, the pectoral fin undergoes a 3D motion. We modify the blade element theory, so that we have blades in both span and chord length of the fin, resulting in 2D elements, which we use to evaluate the hydrodynamic forces. The fin parameters during the recovery stroke are shown in Figure 4.5, where Λ is the feathering angle that we need to find in order to fully know the pectoral fin dynamics. Note that the feathering angle $\Lambda = 0$ during the power stroke.

The relationship between the pectoral fin coordinate system and the body-fixed coordinate system is as follows

$$\hat{m} = \cos\gamma\hat{i} + \sin\gamma\hat{j} + 0\hat{k}, \tag{4.8}$$

$$\hat{n} = \sin\gamma\cos\Lambda\hat{i} - \cos\gamma\cos\Lambda\hat{j} - \sin\Lambda\hat{k}, \tag{4.9}$$

$$\hat{p} = -\sin\gamma\sin\Lambda\hat{i} + \cos\gamma\sin\Lambda\hat{j} - \cos\Lambda\hat{k}. \tag{4.10}$$

where Λ is the feathering angle defined with respect to $-\hat{k}$.

The blade element theory is revised to evaluate the hydrodynamic forces on a 2D element of the pectoral fin. The hydrodynamic drag force produced by each element dcds during the recovery stroke is evaluated as

$$\mathrm{d}F_{hp}(c,s,t) = -\frac{1}{2}C_n(\alpha(c,s,t))\rho|\vec{v}_p^2(c,s,t)|\mathrm{d}c\mathrm{d}s\ \ \hat{e}_{v_p}, \tag{4.11}$$

where $\hat{e}_{v_p}$ is a unit vector in the direction of $\vec{v}_p(c,s,t)$, $\alpha(c,s,t) = \mathrm{atan}\frac{<v_p(c,s,t),\hat{n}>}{<v_p(c,s,t),\hat{m}>}$ is the angle of attack, and $\vec{v}_p(c,s,t)$ is the velocity of each element dcds, and is represented as

$$\begin{aligned}
\vec{v}_p(c,s,t) &= v_{px}\hat{i} + v_{py}\hat{j} + v_{pz}\hat{k} \\
&= \Big\{-(l_1+s)\dot{\gamma}\sin\gamma - c\dot{\gamma}\cos\gamma\sin\Lambda - c\dot{\Lambda}\sin\gamma\cos\Lambda\Big\}\hat{i} \\
&+ \Big\{(l_1+s)\dot{\gamma}\cos\gamma - c\dot{\gamma}\sin\gamma\sin\Lambda + c\dot{\Lambda}\cos\gamma\cos\Lambda\Big\}\hat{j} \\
&- \Big\{c\dot{\Lambda}\sin\Lambda\Big\}\hat{k}
\end{aligned} \tag{4.12}$$

We note that there is notation abuse associated with dF_{h_p}, α, and $\vec{v}_p$, which depend only on s and t in (4.4) but depend on s, c, and t in (4.11), and hope their meanings will be clear from the context. The total hydrodynamic force is evaluated by integrating the force density over the surface of the pectoral fin

$$\vec{F}_{hp}(t) = \int_0^S \int_0^C \mathrm{d}F_{hp}(c,s,t). \tag{4.13}$$

4.3.2 Solving the Feathering Dynamics

During the power stroke, the rigid fin follows the servo motion ($\Lambda = 0$), and the corresponding hydrodynamic force on the fin can be evaluated given the servo motion. On the other hand, during the recovery stroke, the evaluation of the hydrodynamic force (Eq. (4.11)) requires knowing the feathering angle Λ, which has to be solved for through the dynamics equation for the feathering joint.

The total force acting on the rigid fin is represented as

$$\vec{F}_2 = \vec{F}_{hP} - \vec{F}_{A_1} = m_p \left.\frac{\mathrm{d}\vec{v}_p(c,s,t)}{\mathrm{dt}}\right|_{s=\frac{S}{2}, c=\frac{C}{2}}, \tag{4.14}$$

where $\vec{F}_{hP}$ is the hydrodynamic force on the rigid fin (calculated based on the equations presented in Section 4.3.1), $\vec{F}_{A_1}$ represents the force applied by the rigid fin (through the joint) on the servo arm, and m_p is the effective mass of the rigid pectoral fin, which contains the fin mass and the added mass (where the added mass is calculated base on a rigid plate moving in the water).

Since we need to find the feathering angle of the fin, Λ, the projection of the hydrodynamic force in $\hat{n}$ direction produces the corresponding moment. The moment of the rigid fin relative to its pivot point is evaluated as

$$\vec{M}_{hP}(t) = \int_0^S \int_0^C c\hat{p} \times \mathrm{d}F_{hP}(c,s,t). \tag{4.15}$$

Here $\vec{M}_{hP}$ is a function of Λ and $\dot{\Lambda}$. The moment produced by the flexible feathering joint, which is modeled as a pair of torsional spring and damper, is evaluated as

$$\vec{M}_{(S+D)} = (-K_S\,\Lambda - K_D\,\dot{\Lambda})\ \hat{m}, \tag{4.16}$$

where K_S and K_D are the spring and damper coefficients used to model the flexible feathering joint.

The total moment equation of the rigid fin relative to its pivot point of feathering is written as

$$\vec{M}_2 = \vec{M}_{h_P} + \vec{M}_{(S+D)} = -I_p \ddot{\Lambda}, \tag{4.17}$$

where I_p is the effective inertia of the rigid fin (which contains the fin inertia and the added inertia, and is calculated base on a rigid plate moving in the water) and $\ddot{\Lambda}$ is the angular acceleration of the fin in $\hat{m}$-direction. By solving Eq. (4.17), the dynamics of the pectoral fin with a flexible feathering joint during the recovery stroke is fully described.

4.3.3 Hydrodynamic Forces and Moments on the Robotic Fish

The hydrodynamic force transmitted to the servo arm can be obtained as

$$-\vec{F}_{A_1} = \vec{F}_{h_P} - m_p \frac{\mathrm{d}\vec{v}_p(c,s,t)}{\mathrm{dt}}\bigg|_{s=\frac{S}{2},c=\frac{C}{2}}. \tag{4.18}$$

The total force exerted by the arm on the robot body is

$$\vec{F}_h = F_{h_x}\hat{\imath} + F_{h_y}\hat{\jmath} = \vec{F}_{A_1}. \tag{4.19}$$

The moment applied by the fin on the body is represented as

$$\vec{M}_h = M_{h_z}\hat{k} = c_p\hat{\jmath} \times \vec{F}_{A_1}. \tag{4.20}$$

Other than hydrodynamic forces and moment transmitted from the pectoral fins, the robotic fish body experiences drag force F_D, lift force F_L, and drag moment M_D, which can be represented as [28, 29, 44]

$$F_D = \frac{1}{2}\rho V_C^2 S_A C_D, \tag{4.21}$$

$$F_L = \frac{1}{2}\rho V_C^2 S_A C_L \beta, \tag{4.22}$$

$$M_D = -C_M \omega_{C_z}^2 \operatorname{sgn}(\omega_{C_z}), \tag{4.23}$$

where V_C is the linear velocity magnitude of the robotic fish body, ω_{C_z} is the angular velocity of the body about the z-axis, ρ is the mass density of water, S_A is the wetted surface area for the body, β is the angle of attack of the body, formed by the direction of body velocity vector with respect to the x-axis. C_D, C_L and C_M are the dimensionless drag force, lift force, and damping drag moment coefficients, respectively, and sgn(.) is the signum function.

4.3.4 Rigid-Body Dynamics of a Pectoral Fin-actuated Robotic Fish Undergoing Planar Motion

The dynamic equations of rigid body undergoing planar motion in the body-fixed coordinates are represented as [20, 85, 102]

$$(m_b - m_{a_x})\dot{V}_{C_x} = (m_b - m_{a_y})V_{C_y}\omega_{C_z} + f_x, \tag{4.24}$$

$$(m_b - m_{a_y})\dot{V}_{C_y} = -(m_b - m_{a_x})V_{C_x}\omega_{C_z} + f_y, \tag{4.25}$$

$$(I_z - I_{a_z})\dot{\omega}_{C_z} = \tau_z, \tag{4.26}$$

where m_b is the robotic fish actual mass, $-m_{a_x}$ and $-m_{a_y}$ represent the added mass effects along the x and y directions of the body-fixed coordinates, respectively. I_z is the robot inertia and $-I_{a_z}$ is the added inertia of the robot about the z-axis. The variables f_x, f_y and τ_z indicate the external hydrodynamic forces and moment exerted on the fish body center of mass, which are induced by the pectoral fin motion and the interaction of the robotic fish body with the surrounding fluid, which can be described as

$$f_x = F_{h_x} - F_D \cos\ \beta + F_L \sin\ \beta, \tag{4.27}$$

$$f_y = F_{h_y} - F_D \sin\ \beta - F_L \cos\ \beta, \tag{4.28}$$

$$\tau_z = M_{h_z} + M_D, \tag{4.29}$$

Finally, the kinematic equations for the robot in the inertial coordinate system are described as [29],

$$\dot{X} = V_{C_x}\ \cos\ \psi - V_{C_y}\ \sin\ \psi, \tag{4.30}$$

$$\dot{Y} = V_{C_y}\ \cos\ \psi + V_{C_x}\ \sin\ \psi, \tag{4.31}$$

$$\dot{\psi} = \omega_{C_z}. \tag{4.32}$$

where ψ denote the angle between the x-axis and X-axis.

4.4 Experimental Results

4.4.1 Robotic Fish Prototype and Experimental Setup

Experiments are performed to study the performance of a robotic fish with flexible feathering joint and validate the proposed mathematical model. The robotic fish body is designed in SolidWorks software and 3D-printed, as shown in Figure 4.6. The body is about 15 cm long, 8 cm high and 4.6 cm wide without the pectoral and caudal fins, and weighs close to 0.3 kg. An Arduino pro

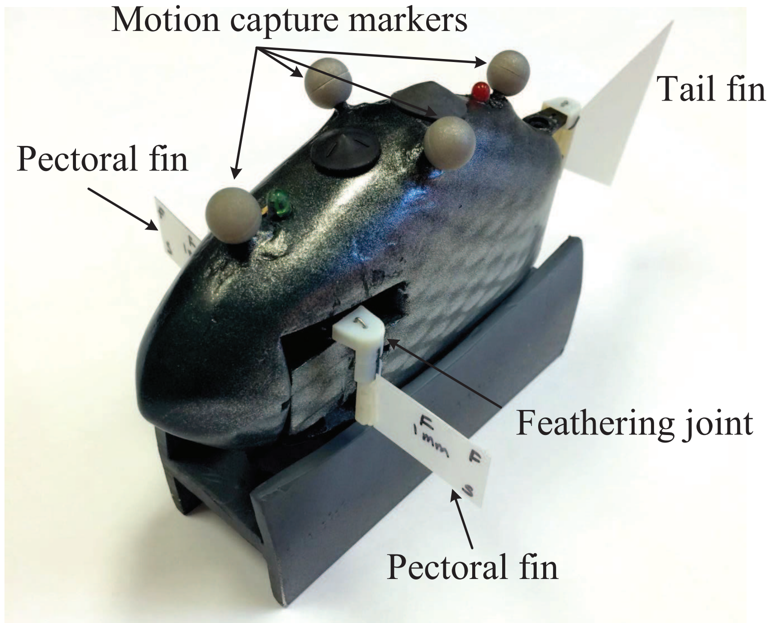

Figure 4.6: 3D-printed robotic fish prototype along with mounted fins.

mini microcontroller board is incorporated in the robot to realize the control of servos. The robot body also houses a power converter printed-circuit board with voltage regulators for the motor and electronics. The motors used for actuation of the pectoral and caudal fins are Traxxas 2065 waterproof servos with maximum speed of 200 °/sec. Although the robot is capable of moving its caudal fin, tail actuation is not included in this study. The servomotors are programmed to rotate each pectoral fin according to

$$\gamma(t) = \gamma_A \sin(\omega_\gamma \ t) + 90^\circ, \tag{4.33}$$

where γ_A is the amplitude in degrees and ω_γ denotes the angular frequency of fin flapping. The pectoral fins are made of a light plastic material (polypropylene) that has 0.5 mm thickness with Young's modulus of approximately 2 GPa, which is considered to be almost rigid.

As shown in Figure 4.7, the experiments are conducted in a water tank that measures 2 feet wide, 6 feet long, and 2 feet deep. The tank is equipped with a motion capture system from NaturalPoint, which contains four Optitrack Flex 13 cameras along with Motive software to capture the

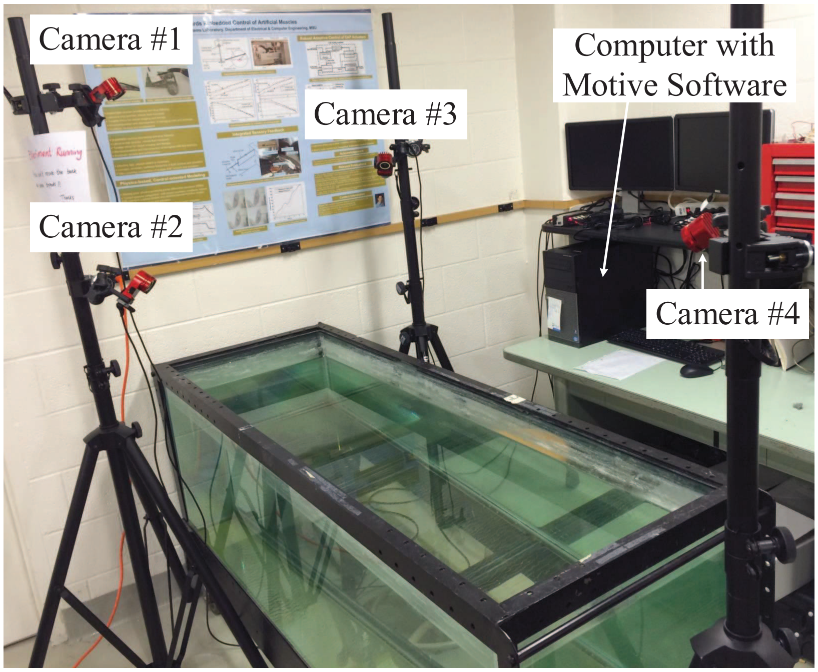

Figure 4.7: Experimental setup for free-swimming robotic fish.

motion of robotic fish. Two different experiments are conducted to evaluate the proposed dynamic model. First, the robotic fish is studied when the body is anchored to measure the feathering angle, and second, free-swimming of the robotic fish is run to measure the forward swimming velocity, turning radius, and turning period. All the measurements are done approximately 30 seconds after the robot initiated swimming to ensure that it has reached steady-state motion. The experiment for each setting is repeated 10 times. At the end, the captured videos are analyzed by the Motive software to extract the steady-state speed for the forward swimming, and the turning radius and period for the turning motion.

4.4.2 Parameter Identification

The parameters of the mathematical model are either measured directly or identified experimentally as follows: The body inertia about z-axis is evaluated as $I_z = \frac{1}{5}m_b(a^2+c^2)$, where $a = \frac{\text{Body length}}{2}$ and $c = \frac{\text{Body width}}{2}$ are semi-axis lengths of the body [28]. The added masses, added inertia and

Table 4.1: Identified Model Parameters.

Component	Parameter	Value	Unit
Body	Mass (m_b)	0.295	Kg
	Inertia (I_z)	4.26×10^{-4}	Kg/m^2
	$-m_{a_x}$	0.095	Kg
	$-m_{a_y}$	0.1794	Kg
	$-I_{a_z}$	2.7×10^{-5}	Kg/m^2
	Wet surface area (S_A)	0.0325	m^2
	Drag coef. (C_D)	0.42	–
	Lift coef. (C_L)	4.86	–
	Moment coef. (C_M)	7.6×10^{-4}	Kg/m^2
Fin	Length (S)	0.035	m
	Depth (C)	0.02	m
	Servo arm length (l_1)	0.01	m
	Effective mass (m_p)	0.0166	Kg
	Effective inertia (I_p)	3.32×10^{-6}	Kg/m^2
	Distance from body center to servo base, c_p	0.025	m
	Water density (ρ)	1000	Kg.m^3

wetted surface are calculated by approximating the robot body as an prolate spheroid accelerating in the fluid [28, 88]. The parameters used in simulations are listed in Table 4.1.

The robotic fish drag and lift coefficients, C_D, C_L, and C_M, are identified empirically using the collected data from the robotic fish equipped with rigid joints for the pectoral fins. With rigid joints, we need to have different power and recovery stroke speeds to produce a net thrust [21]. This ratio is indicated as $\frac{P}{R}(\frac{\text{Power stroke speed}}{\text{Recovery stroke speed}})$, which is equal to 1 for the symmetric fin flapping. Here, we experiment with the cases of $\frac{P}{R}$ = 2, 3, 4, and 5. The experimental results for both forward and turning swimming motions of the robotic fish with $\frac{P}{R}$ = 2 are used to identify the body parameters, where turning is realized by actuating one pectoral fin only. C_D, C_L, and C_M are tuned to match the forward velocity, turning radius, and turning period obtained in simulation with the experimental measurement when the power stroke is completed in 0.5s and 0.3s, respectively.

The fin beat amplitude is set to 25°. The identified coefficients are $C_D = 0.42$, $C_L = 4.86$, and $C_M = 7.6 \times 10^{-4}\text{Kg}/\text{m}^2$. These parameters are then used in independent model validation for all other cases using the flexible feathering joint.

Among all the feathering joints mentioned in Section 4.2, joint "JF1" results in the highest forward velocity in the tested frequency range. So, without the loss of generality, this joint is chosen to perform the model validation. To identify the spring and damper coefficients for this joint, K_S and K_D are tuned to match the forward swimming velocity of the robotic fish obtained in simulation with the experimental measurements for fin beat frequencies of 1 Hz, 1.5 Hz and 2 Hz. The coefficients are identified as $K_S = 1.31 \times 10^{-4}\ \text{N} \cdot \text{m}$ and $K_D = 4.64 \times 10^{-5}\ \text{N} \cdot \text{m} \cdot \text{s}$. These parameters are then used for model validation of various other cases involving the same feathering joint.

4.4.3 Comparison between Flexible Feathering and Rigid Joints

First, we provide a comparison on the forward swimming velocity of the robotic fish with the flexible feathering joint, with that of a rigid joint. Here, rigid joint refers to a rigid connection between the servo arms and the pectoral fins. For the rigid joint case, in order to have a net thrust, we use different power and recovery stroke speeds, introduced in Section 4.4.2. Figure 4.8(a) provides the experimental results on forward swimming velocity with the rigid joint, where $\frac{P}{R}$= 1, 2, 3, 4, 5, and with the flexible feathering joint "JF1", over different power stroke times. Figure 4.8(b) presents the same results in terms of the effective fin beat frequency. Here, the effective fin beat frequency is calculated as $\frac{1}{T}$, where T is the period of each fin beat cycle, combining both power and recovery strokes. The servos are programmed to run up to the limit of 200 °/sec, which refers to the rightmost point in each curve of Figure 4.8(b). From Figure 4.8, one can conclude that, the performance of the flexible feathering joint outperforms the rigid joint case at higher frequencies

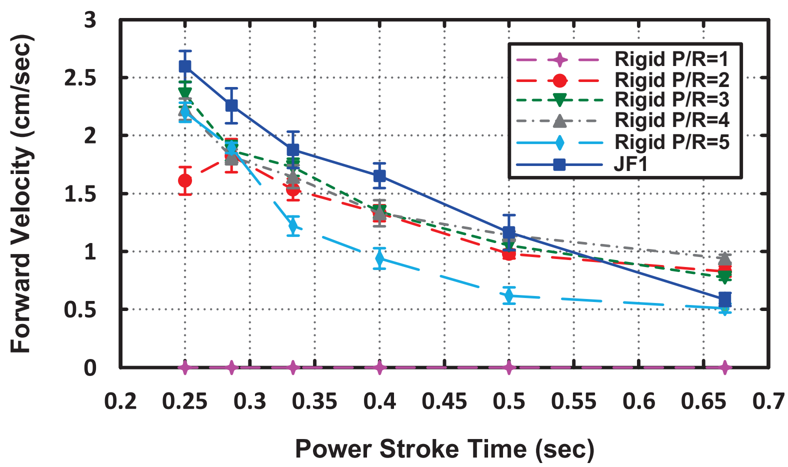

(a)

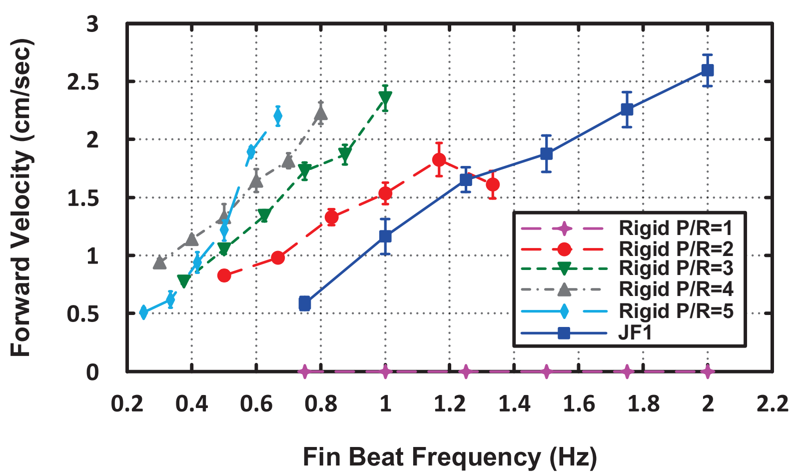

(b)

Figure 4.8: Experimental results of the forward swimming velocity in terms of (a) the power stroke time, and (b) the effective actuation frequency, for the cases of rigid joint and flexible feathering joint “JF1”.

(1.3 Hz and above). For lower fin beat frequencies, the rigid joint cases outperform the flexible feathering joint. Note that the relationship between the flapping frequency and the swimming speed is almost linear up to a threshold value for the flapping frequency, which is observed naturally in fish [123].

4.4.4 Dynamic Model Validation

This subsection describes the experiments carried out on the robotic fish with flexible feathering joint, to validate the proposed mathematical model. Two kinds of experiments are performed in still water for validation purposes. For the first set of experiments, the robot body is fixed using a bracket. The pectoral fins are actuated with $\gamma(t) = 25^{\circ}\sin(\omega_{\gamma}\ \ t) + 90^{\circ}$. The motion of the right pectoral fin is tracked from the side (xz plane), using a Casio Exilim (EX-FH25) high-speed camera, recording at 40 frames per second. The videos are then processed and the maximum feathering angle with respect to $-\hat{k}$ is measured and compared to those predicted by the model. Figure 4.9 shows the maximum feathering angle during the recovery stroke, in both simulation and experiments at different fin-beat frequencies. The model is able to capture the maximum feathering angle well for all frequencies up to 1.5 Hz. For higher frequencies, the discrepancy between the model prediction and the measurement starts to grow. This can be attributed to the constraint of the fabrication, which imposes a limitation on the feathering angle of the joint.

For the second set of experiments, the robotic fish is allowed to swim freely in the tank. Both forward swimming and turning are enabled with the pectoral fins incorporating the flexible feathering joints. Figure 4.10 shows the experimental and simulation results where the forward swimming velocities of the robotic fish are plotted at different fin-beat frequencies. The forward swimming velocities of the robotic fish is reported both in cm/sec and BL/sec scales. Figures 4.11 and 4.12 show similar comparisons on the turning radius and turning period of a free-swimming robotic fish. The results of Figures 4.10 - 4.12 show that the proposed model is able to capture the motion of the robotic fish with flexible feathering joints very well. In particular, for the tested frequency range, the forward swimming velocity increases with the fin-beat frequency. In the turning case, the turning period (the time it takes to complete one turn) drops with the increasing fin-beat frequency,

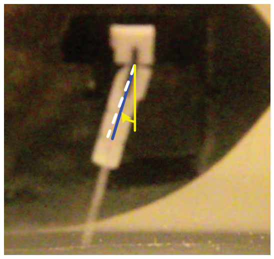

Experiment = 18°
Simulation = 21°

(a)

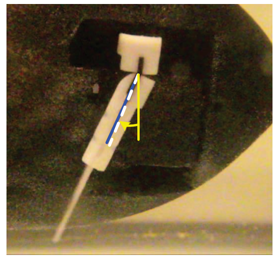

Experiment = 25°
Simulation = 24°

(b)

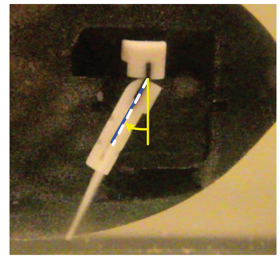

Experiment = 30°
Simulation = 29°

(c)

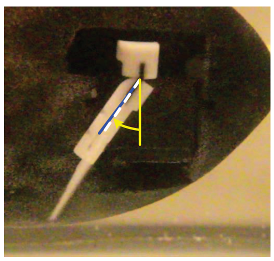

Experiment = 37°
Simulation = 36°

(d)

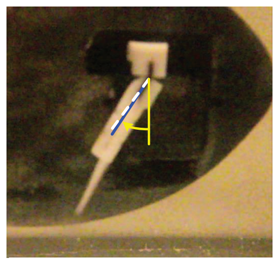

Experiment = 34°
Simulation = 37°

(e)

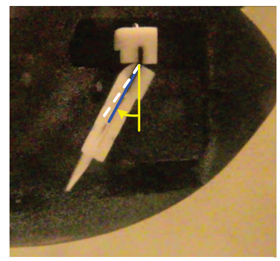

Experiment = 32°
Simulation = 38°

(f)

Figure 4.9: Comparison between model prediction (white dashed line) and experimental measurement (blue solid line) of the maximum feathering angle during the recovery stroke, with fin beat frequencies of (a) 0.75 Hz, (b) 1 Hz, (c) 1.25 Hz, (d) 1.5 Hz, (e) 1.75 Hz, and (f) 2 Hz. The yellow solid line indicates the $-\hat{k}$ direction.

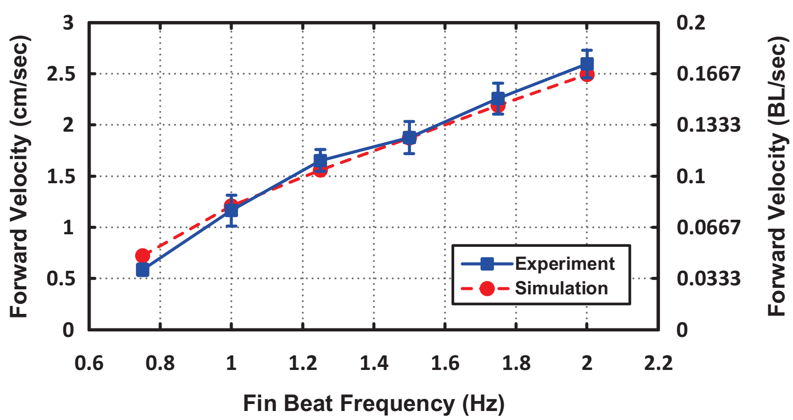

Figure 4.10: Case of feathering joint (JF1): Comparison between the model-predicted and measured forward swimming speed, for different fin beat frequencies. The forward swimming velocity is reported in cm/sec scale on the left y-axis and in BL/sec on the right y-axis.

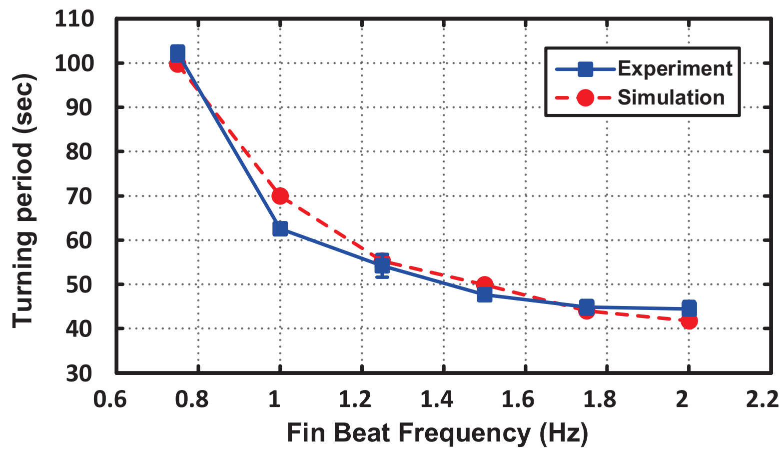

Figure 4.11: Case of feathering joint (JF1): Comparison between the model-predicted and measured turning period, for different fin beat frequencies.

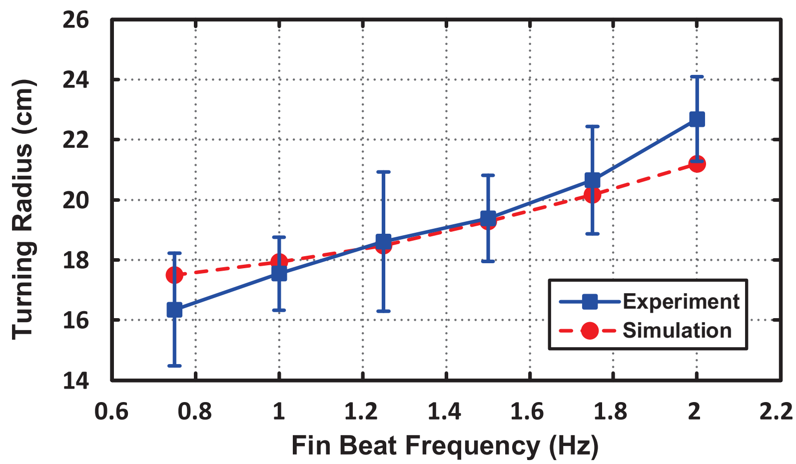

Figure 4.12: Case of feathering joint (JF1): Comparison between the model-predicted and measured turning radius, for different fin beat frequencies.

which matches with one's intuition, and the turning radius increases with fin-beat frequency.

4.5 Effect of Flexible Joint Depth and Stiffness

Here, we study the effect of different parameters of the flexible feathering joint on its performance. As described in [91], the stiffness of the torsional spring constant is evaluated as

$$K_S = \frac{Edh^3}{12l}, \tag{4.34}$$

where h is the thickness, l is the length (which corresponds to the depth in the case of the proposed flexible joint), d is the width, and E is the Young's modulus of the flexible material used for the passive joint. The damper coefficient K_D is evaluated as $K_D = \kappa K_S$, where κ is a proportional constant. Keeping the width and thickness of the joint constant, the spring coefficient can be varied by changing the depth (l) and stiffness (E) of the flexible joint. This study will let us further validate the proposed mathematical model and provides useful information on the joint optimization.

We choose three different depth for the flexible feathering joint made of FLX980 material, 0.5 mm, 1 mm and 1.5 mm (Joints JF1, JF2, and JF3). The spring and damper constants for JF2 and JF3 are calculated using Eq. (4.34), where the Young's modulus (E) and κ values are kept the same as the ones for JF1. Figure 4.13 shows the model prediction and experimental results of forward swimming velocity at different fin-beat frequencies, for different flexible feathering joint lengths. The joint JF1 (least flexible among the three) has the best performance among the three joints in the higher fin-beat frequencies (higher than 1.75 Hz). For lower frequencies, joint JF3 (most flexible among the three) outperforms the other two. So we can conclude that the more flexible joint performs better at lower frequencies, while the stiffer joint has a better performance at higher frequencies. We can see that the model is able to capture the joint depth-dependence of the forward swimming velocity effectively for all three cases. Here, the experimental limit for the actuation frequency is 2 Hz, so we have extended the simulation results to fin-beat frequency of

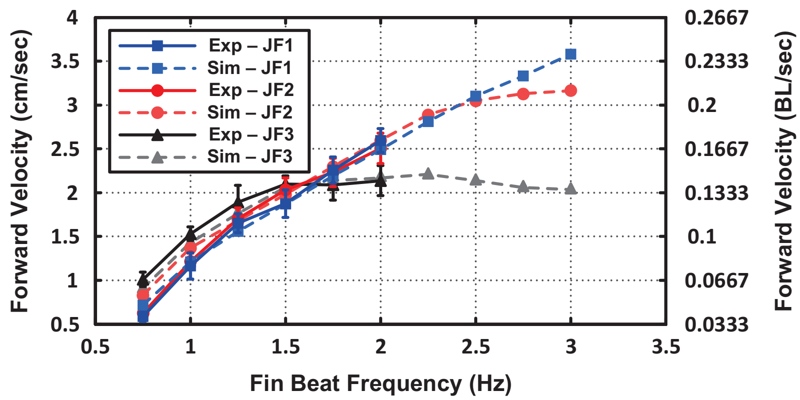

Figure 4.13: Model prediction and experimental measurement of the forward swimming velocity of the robotic fish using three different flexible feathering joints, made of FLX980, with different depths. The forward swimming velocity is reported in cm/sec scale on the left y-axis and in BL/sec on the right y-axis.

3 Hz in order to capture the performance trend of each joint. The forward swimming speed will drop after reaching an optimal frequency for each case.

Finally, we investigate the effect of changing the stiffness (E) of the joint on the robotic fish performance. Here, we choose two flexible feathering joints with the same dimension, one using FLX980 as the flexible material, joint JF1, and the other using DM9850 as the flexible material, joint JF4. The spring and damper coefficients for JF4 are identified to be $K_S = 0.0018\ \mathrm{N \cdot m}$ and $K_D = 0.0064\ \mathrm{N \cdot m \cdot s}$ using the same method described in Section 4.4.2, and are kept the same for model prediction of all other cases using the same joint. The comparison of forward swimming velocity using these two joints are reported in Figure 4.14. It can be seen that there is good match between the model prediction and experimental data. Overall, the joint JF1 outperforms JF4 at lower frequencies, while the joint JF4 starts to outperform joint JF1 at higher frequencies. Again, we have extended the model prediction results to capture the performance of the joints at higher frequencies.

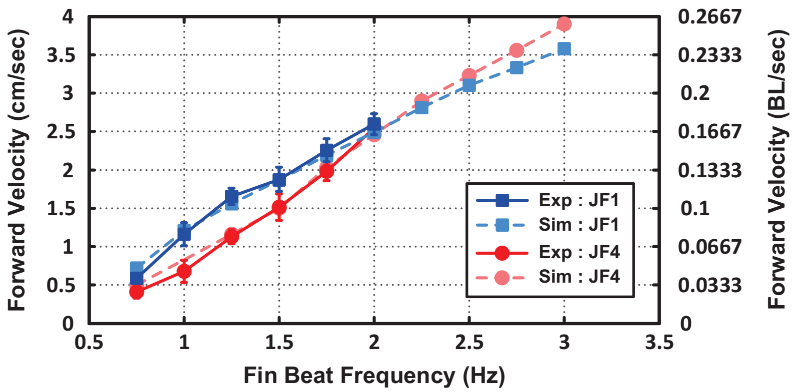

Figure 4.14: Model prediction and experimental results of the forward swimming velocity of the robotic fish with the use of two flexible feathering joints with different stiffness values. The forward swimming velocity is reported in cm/sec scale on the left y-axis and in BL/sec on the right y-axis.

4.6 Mechanical Efficiency

In this section, we calculate the propulsive efficiency of the robotic fish swimming with the flexible feathering joint for the pectoral fins. The efficiency during the steady-state swimming is calculated as [5]

$$\eta = \frac{W_b}{W_T}, \tag{4.35}$$

where W_b is the amount of useful work needed to propel the robotic fish and W_T is the total work done by the pectoral fins for each fin-beat cycle. This efficiency is called mechanical efficiency, since the energy losses, such as frictional losses or the power used to run the motors, are not considered in the calculations. During steady-state swimming, when the robot swims with a constant speed $V_{C_{mean}}$, the drag force acting on the body is balanced by the thrust force F_T. So we have

$$F_T = \frac{1}{2}\rho V_{C_{mean}}^2 S_A C_D. \tag{4.36}$$

So the useful propulsive power is calculated by multiplying thrust force, F_T, by the constant speed, $V_{C_{mean}}$, resulting in the useful work

$$W_b = F_T V_{C_{mean}} T_0 = \frac{1}{2}\rho V_{C_{mean}}^3 S_A C_D T_0, \tag{4.37}$$

where $T_0 = T_p + T_R$ denotes the total duration of each fin-beat cycle, consists of duration of power and recovery strokes, where $T_P = T_R = \frac{T0}{2}$. Note that even at the steady state, the actual velocity is not a constant; instead, it periodically fluctuates around some value. Therefore, $V_{C_{\mathrm{mean}}}$ in Eq. (4.36) is evaluated by the distance traveled over N cycles (for example, $N = 10$) divided by NT_0.

The total work done by the paired pectoral fins, W_T, is obtained as

$$\begin{aligned}
W_T = {} & 2\int_{t_0}^{t_0+T_P} \max\left\{0, \int_0^S \mathrm{d}F_{h_p}(s,t)\cdot\vec{v}_p(s,t)\right\} \mathrm{d}t \\
& + 2\int_{t_0+T_P}^{t_0+T_P+T_R} \max\left\{0, \int_0^S\int_0^C \mathrm{d}F_{h_p}(c,s,t)\cdot\vec{v}_p(c,s,t)\right\} \mathrm{d}t \\
= {} & 2\int_{t_0}^{t_0+T_P} \max\left\{0, \int_0^S \frac{1}{2}C_n(\alpha(s,t))\rho|\vec{v}_p(s,t)|^2\cdot\vec{v}_p(s,t)\ \mathrm{d}s\right\} \mathrm{d}t \\
& + 2\int_{t_0+T_P}^{t_0+T_P+T_R} \max\left\{0, \int_0^S\int_0^C \frac{1}{2}C_n(\alpha(c,s,t))\rho|\vec{v}_p(c,s,t)|^2\cdot\vec{v}_p(c,s,t)\ \mathrm{d}c\,\mathrm{d}s\right\} \mathrm{d}t,
\end{aligned} \tag{4.38}$$

where, t_0 denotes the beginning of a fin-beat cycle and "$\cdot$" denotes the inner product. Note that at some time instants t, the instantaneous mechanical power exerted by pectoral fins on water could be negative; however, since the servos cannot reclaim this energy from water, we treat the instantaneous power at such t as zero, which explains the operator $\max\{0,\cdot\}$ in Eq. (4.38).

Figure 4.15 shows the results for calculated mechanical efficiency, along with the corresponding forward swimming velocity, for joints JF1, JF2 and JF3. Joint JF3 has highest efficiency at lower frequencies and joint JF1 is the most efficient at higher frequencies. Each joint has a maxi-

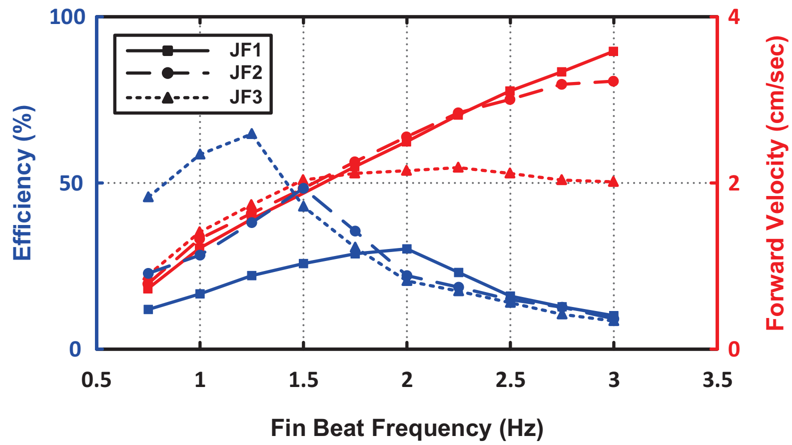

Figure 4.15: Calculated mechanical efficiency (blue) and forward swimming velocity (red) for different flexible feathering joints at different fin beat frequencies.

mum efficiency at a certain frequency. So we can conclude that a more flexible joint (JF3) is more efficient at lower frequencies and a less flexible joint (JF1) is more efficient at higher frequencies. Figure 4.16(a) shows the efficiency curve versus different fin-beat frequencies and spring constant values (K_S). This figure shows that the robotic fish performs more efficiently in lower fin-beat frequencies with more flexible feathering joints up to a certain optimal stiffness. Figure 4.16(b) shows the spring constant of the feathering joints that have maximum mechanical efficiency in different fin-beat frequencies. From this figure, we can conclude that, the more flexible feathering joints are performing more efficiently at lower fin-beat frequencies, while the stiffer joints act more efficiently at higher frequencies. Note that, there is an optimal point for the maximum efficiency among all the feathering joints. From Figure 4.16(c), one can see there is an optimal spring constant for the maximum efficiency. For any joint stiffer or more flexible than this optimal amount, the efficiency starts to drop. Note that a similar trend is observed in [124–127]. Overall, Figures 4.15 and 4.16 indicate that the optimization of the flexible joint presents an interesting, multi-objective design problem that involves consideration of the joint stiffness, dimension, and the frequency of fin operation. The proposed dynamic model in this paper shows promise in addressing the optimal

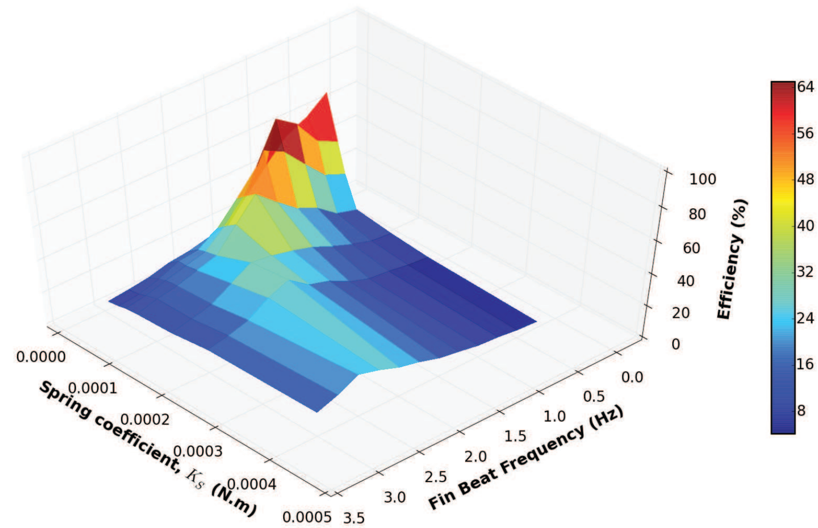

(a)

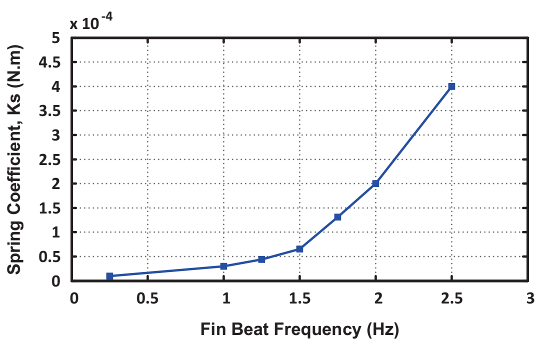

(b)

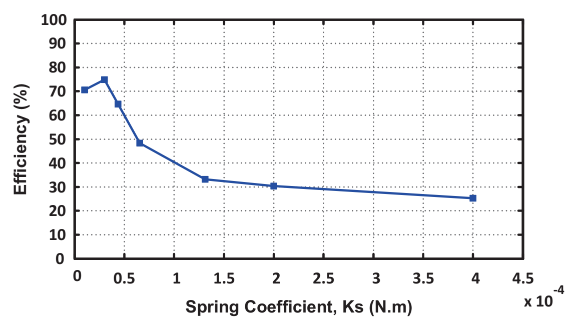

(c)

Figure 4.16: Mechanical efficiency: (a) Calculated mechanical efficiency versus fin-beat frequency and spring constant of the flexible feathering joint, (b) Spring constant of the feathering joint with maximum efficiency versus fin-beat frequency, (c) Maximum efficiency versus spring constant.

design problem.

Table 4.2 presents the mechanical efficiency and Strouhal number for joints JF1, JF2, and JF3. Here the Strouhal number of the robotic fish is calculated as

$$\mathrm{St} = \frac{fA}{V_{C_{mean}}} \tag{4.39}$$

where f is the flapping frequency, A is the flapping amplitude for pectoral fin, and $V_{C_{mean}}$ is the

Table 4.2: Mechanical efficiency versus the Strouhal number.

Frequency (Hz)	Joint JF1		Joint JF2		Joint JF3	
	Efficiency (%)	Strouhal number	Efficiency (%)	Strouhal number	Efficiency (%)	Strouhal number
0.75	11	3.7911	23	3.5436	46	2.3843
1	17	2.5447	28	2.4366	59	2.1383
1.25	22	2.3680	38	2.2194	**64**	**2.0430**
1.5	27	2.3653	**48**	**2.1865**	43	2.2005
1.75	29	2.2947	36	2.3189	30	2.5797
2	**32**	**2.2798**	22	2.3611	20	2.8766
2.25	23	2.3688	19	2.3437	17	3.0533
2.5	15	2.3857	15	2.4653	15	3.5051
2.75	13	2.4653	12	2.5583	10	4.0076
3	10	2.4790	9	2.7562	8	4.4154

average swimming speed. Here the flapping amplitude $A = 2S\sin\gamma$, where S is the pectoral fin span length and γ is the angular amplitude of flapping [27, 35]. We observe consistent (negative) correlation between the efficiency and the Strouhal number. In particular, for each joint, at the fin-beat frequency where the efficiency achieves the maximum, the corresponding Strouhal number is the lowest. Note that the Strouhal number for biological fish is usually in the range of 0.05-0.6, and the numbers presented here are bigger than that range. The reason is that the robotic fish used in this study swims forward with its pectoral fins alone, which results in relatively slow speeds and thus relatively high Strouhal numbers comparing to its biological counterparts. From Table 4.2, the robotic fish tends to have higher mechanical efficiency when its Strouhal number gets closer to the range for biological data.

4.7 Conclusion

In this study, we have proposed a novel design for a flexible passive joint, which enables the pectoral fins to move similar to the drag-based labriform swimming mode. A dynamic model is presented for a robotic fish propelled by a pair of rigid pectoral fins connected to the actuators via the proposed flexible feathering joints. The joint enables the pectoral fin to be actuated symmetrically to row for power and recovery strokes, while providing feathering about the transverse axis during the recovery stroke to minimize the drag force. The combined rowing and feathering results in 3D movement of the pectoral fin, which needs to be captured properly in the modeling. The blade element theory is used to evaluate the hydrodynamic forces on the pectoral fin during both power and recovery strokes. The flexible feathering joint is modeled as a pair of torsional spring and damper. A complete dynamic model for a robotic fish incorporating the proposed joints is also presented. To validate the proposed dynamic model, we have measured the feathering angle of an anchored robotic fish, along with the forward velocity, turning radius and period of the robot during free swimming, and compared those to the model predictions. Multiple flexible feathering joints have been explored to study the effect of depth and stiffness of the flexible part. The mechanical efficiency of the robotic fish in forward swimming is explored numerically, to understand the trade-offs in the joint design and operation frequency.

Chapter 5

Design and Dynamic Modeling of Electrorheological Fluid-Based Variable-Stiffness Fin for Robotic Fish

Fish propel in water by moving different fins or deforming the body [16,17], which has inspired the development of robotic fish that accomplish locomotion in ways that emulate those of biological fish [9, 86, 87, 128–130]. Compared with rigid fins, flexible fins and fin joints introduce additional dynamic behavior that can be exploited to enhance robotic fish performance [21,29,58,84,85,117, 131–135]. Although passive compliant fins could result in more efficient swimming, the optimal flexibility changes with parameters such as fin-beat frequency or amplitude [86, 87, 94, 136]. For example, with an increased fin-beat frequency and amplitude, the optimal stiffness tends to increase [135, 137, 138]. The connection between propulsor stiffness and swimming performance has also been studied for biological fish. The live fish adjust the stiffness of the fins/body to complete different tasks [38, 42, 43].

The discussions above indicate that it is of interest to actively tune the fin stiffness for robotic fish according to swimming conditions, and there has been some limited work reported in this area over the past few years [68, 69, 139]. Ziegler *et al.* [139] introduced a tail-actuated robotic fish, where the tail fin was capable of changing its elasticity, which was realized by actively inserting additional foils into the tail fin or removing these foils from the fin using two servo motors. Park *et al.* [68] designed a fin with a variable-stiffness flapping mechanism, which was realized by compressing a compliant material to increase the stiffness. The designed tail consisted of six rigid plates, also used as the backbone of the fish. Two tendons were used for driving the tail and two other tendons were used to change its stiffness. In particular, when the latter tendons were pulled, the variable stiffness structure would be compressed and result in an increase in axial stiffness. Nakabayashi *et al.* [69] developed a robotic fish with a variable stiffness mechanism using a variable effective-length spring mechanism, achieved by altering the length of a rigid plate, which resulted in changing the effective-length of the spring and hence the stiffness. All these reported mechanisms were bulky and complex.

In this work, we propose a compact mechanism for fin stiffness tuning using electrorheological (ER) fluid. This fluid consists of a base liquid (usually silicone oil) with suspended polymer particles. An ER fluid experiences changes in rheological properties in the presence of an electric field, going from the liquid phase to a solid gel phase as the electric field increases. In particular, the particles align with the electric field line, resulting in changes in viscosity, yield stress, and some other properties of the fluid. The response time of the ER fluid is in the order of milliseconds, which provides a fast solution for stiffness tuning. ER fluids have a range of engineering applications, such as shock absorbers [140], brakes and clutch systems [141], and vibration control [142–144]. The proposed stiffness-tuning fin consists of an ER fluid-filled urethane rubber, with embedded copper sheets as electrodes. A dynamic model for the fin is presented, which is derived using the Hamilton's principle and uses large-amplitude elongated-body theory to capture the hydrodynamic forces on the fin. The final equations of motion are obtained through a finite-element procedure and solved numerically. Experiments are conducted on a fin prototype to examine the performance of stiffness-tuning, identify model parameters (including, in particular, the complex shear modulus of the ER fluid under different electric fields, and the hydrodynamic function), and validate the proposed dynamic model. First, for a given electric field, passive damped vibration of the flexible fin in air is measured to extract the natural frequency and damping ratio, which are used subsequently to identify the complex shear modulus of the ER fluid. Next, a similar procedure is repeated in water to identify the complex hydrodynamic coefficient of the flexible fin. Finally, the behavior of the base-actuated oscillation is studied, in an anchored robotic fish body setup, to validate the proposed dynamic model. Specifically, good match between the measured beam shape and tip deflection and their model predictions indicate the efficacy of the model. The experiments also demonstrate the fin's capability in modulating stiffness. For example, when the electric field is increased from 0 V/m to 1.5×10^6 V/m, the fin's natural frequency increases from 8.1 Hz to 10.1 Hz in air (25% change), and from 3.6 Hz to 5.1 Hz in water (40% change).

The organization of the remainder of this chapter is as follows. First, the fabrication procedure of the ER fluid-filled fin is presented in Section 5.1. In Section 5.2, the dynamic model is described. The experimental results are provided in Section 5.3, where the effect of changing the electric field on the fin stiffness is studied and the proposed dynamic model is validated. Finally, concluding remarks are provided in Section 5.4.

5.1 Fabrication Procedure

5.1.1 Materials

The ER fluid used in this study is LID-3354D from Smart Technology Ltd., West Midlands, England. This fluid consists of 37.5% of sub-45 μm polymer particles in a density-matched silicone

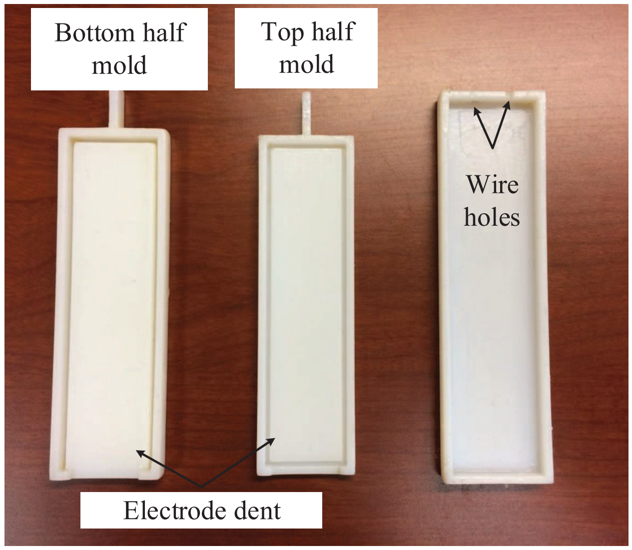

Figure 5.1: 3D-printed molds used to prototype the variable stiffness fin.

oil. The density of the ER fluid is 1460 $\mathrm{Kg/m^3}$ and the viscosity is 110 $\mathrm{mPa \cdot s}$ at 30°C. Two thin copper foils (Copper 110, 99.9 % pure, from Basic Copper, Carbondale, IL, USA) with dimensions of 15 mm $\times$ 8 mm $\times$ 0.035 mm are used as the electrodes. The flexible encasing is made of Vytaflex10, which is a liquid urethane rubber from Smooth-On Inc., Macungie, PA, USA. This rubber has a density of 1000 $\mathrm{Kg/m^3}$.

5.1.2 Manufacturing Procedure

The prototyping of the variable-stiffness fin is done in multiple stages. First, three different molds are designed and 3D-printed for the encasing: Bottom half, top half, and that for assembling the two halves. The actual 3D-printed molds are shown in Fig. 5.1. The molds are designed to make a fin with dimensions of 65 mm $\times$ 20 mm $\times$ 4 mm. The bottom and top molds have a small dent in them to secure the electrodes in place. A gap of 1.5 mm is formed between the two electrodes, where the ER fluid will be injected. In the first step, the copper electrodes are cut and placed in the designed dent in each mold, and the Vytaflex mixture is poured over them. The parts are placed in a vacuum chamber for degassing (29” Hg of vacuum for 5 minutes), and is set to cure for 24

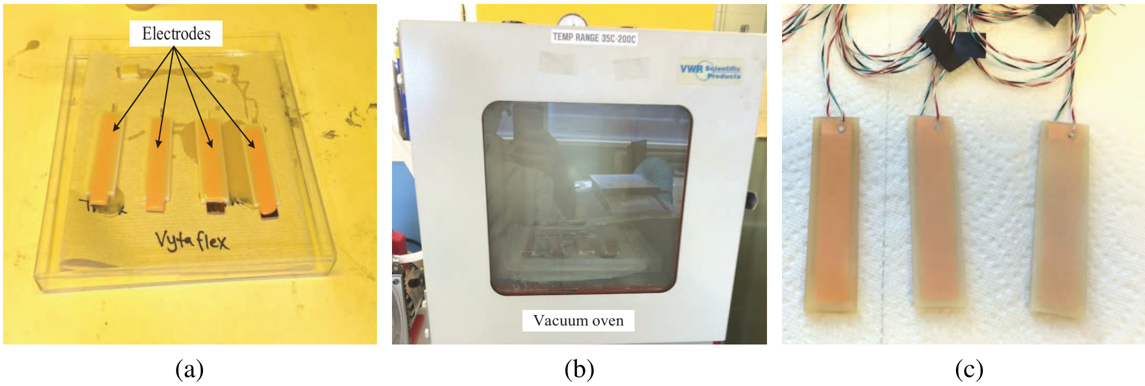

Figure 5.2: Prototyping the variable-stiffness fin: (a) The halves of the fin, with electrodes incorporated; (b) degassing the parts in a vacuum oven; (c) final product: hollow fins with wires attached to the electrodes.

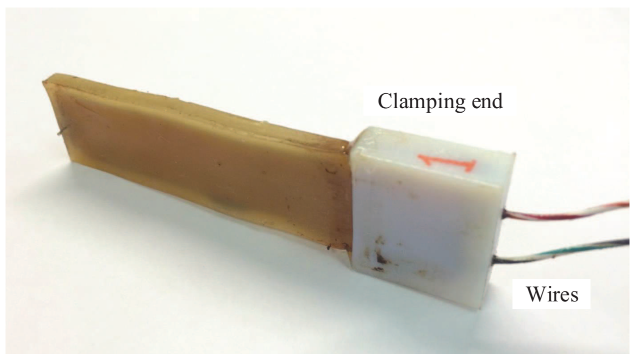

Figure 5.3: Prototyped variable-stiffness fin with ER fluid filled.

hours. Next, we remove the two prototyped halves of the fin from the molds, attach a wire to each electrode, put both in the third mold, pour Vytaflex mixture, degas, and let it cure for another 24 hours. The resulting prototype is a hollow, flexible fin with the electrodes and wires incorporated. The described prototyping steps are illustrated in Fig. 5.2. Finally, a 3D-printed rigid clamping part is attached to the wire end of the fin and the ER fluid is injected from the posterior end of the beam into the hollow gap between the two halves and the injection holes are sealed afterward. Fig. 5.3 shows a final ER fluid-filled prototype.

5.2 Dynamic Model for the Variable-Stiffness Fin

Although the presented fabrication procedure in Section II can be used to make different variable-stiffness fins (such as caudal fin, pectoral fin, among others), this study is focused on the use for the caudal fin (tail). To simplify the modeling procedure, we consider the robotic fish body to be anchored, so the calculations of the body dynamics are not covered in this paper. The motion of the variable-stiffness caudal fin, filled with ER fluid, is modeled using Hamilton's principle. The resulting equations of motion are complex and highly nonlinear, so finite element method is used to numerically solve the equations.

5.2.1 Evaluation of Hydrodynamic Force Using Lighthill's Large-Amplitude Elongated-Body Theory

The hydrodynamic force on the variable-stiffness fin is evaluated using Lighthill's large-amplitude elongated-body theory, which was developed to study the carangiform swimming mode of a fish [70]. As illustrated in Fig. 5.4, $[X,Y,Z]^T$ is the inertial frame, $[x_t,y_t,z_t]^T$ are the tail-fixed coordinate (origin at the base of the tail), and $(\hat{m},\hat{n})$ are the unit vectors tangential and perpendicular to the flexible fin, respectively. The robotic fish is assumed to have a planar motion in the XY-plane. We assume that the water far from the robotic fish body is at rest, and the extensibility of the caudal fin is negligible. The Lagrangian coordinate s indicates a point on the flexible tail and its distance from the base of the fin, which varies from 0 to L (length of the caudal fin). The location of each point on the fin at time t, in the inertial frame, is denoted as $(x(s,t),y(s,t))$. The inextensibility assumption is expressed as

$$\left(\frac{\partial x}{\partial s}\right)^2+\left(\frac{\partial y}{\partial s}\right)^2=1. \tag{5.1}$$

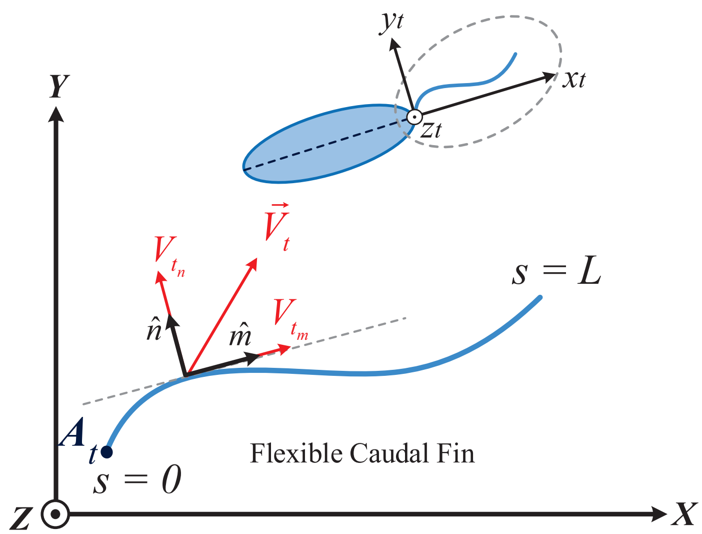

Figure 5.4: Planar view of the robotic fish and the detailed illustration of the flexible tail coordinate system.

The tangential ($\hat{m}$) and normal ($\hat{n}$) unit vectors are represented as

$$\hat{m} = \left(\frac{\partial x}{\partial s}, \frac{\partial y}{\partial s}\right), \tag{5.2}$$

$$\hat{n} = \left(-\frac{\partial y}{\partial s}, \frac{\partial x}{\partial s}\right). \tag{5.3}$$

The velocity vector of the caudal fin $\vec{V}_t = (\partial x/\partial t, \partial y/\partial t)$ has tangential and normal components, represented respectively by,

$$V_{t_m} =< \vec{V}_t, \hat{m} >= \frac{\partial x}{\partial t}\frac{\partial x}{\partial s} + \frac{\partial y}{\partial t}\frac{\partial y}{\partial s}, \tag{5.4}$$

$$V_{t_n} =< \vec{V}_t, \hat{n} >= \frac{\partial y}{\partial t}\frac{\partial x}{\partial s} - \frac{\partial x}{\partial t}\frac{\partial y}{\partial s}, \tag{5.5}$$

where $< \cdot, \cdot >$ denotes the inner product of the vectors. Finally, the hydrodynamic force density experienced by the caudal fin, due to the added-mass effect, for $s < L$ is obtained by

$$\vec{f}_h(s) = -m_v \Gamma \frac{\mathrm{d}}{\mathrm{d}t} V_{t_n} \hat{n}, \tag{5.6}$$

where m_v denotes the virtual mass of the tail and is close to $\frac{1}{4}\pi\rho b^2$, with ρ indicating the density of water and b showing the depth of the caudal fin in z direction, and Γ is the complex hydrodynamic coefficient for the beam [39, 145], which is identified later through experiments. At $s = L$, there is a concentrated force calculated as

$$\vec{F}_{h_L} = \left[m_v V_{t_n} V_{t_m} \hat{n} - \frac{1}{2} m_v V_{t_n}^2 \hat{m} \right]_{s=L}. \tag{5.7}$$

5.2.2 Dynamic Modeling of the Variable-Stiffness Caudal Fin Filled with ER Fluid

We need the information about the movement of the flexible tail, particularly its normal and tangential velocity components at each point, to determine the hydrodynamic forces and moments on the fin. For this purpose, we follow [144, 146–148] and use Hamilton's principle to develop the equations of motion of the flexible tail.

The variable-stiffness fin has a five-layer structure. It consists of an ER fluid core with two copper foil layers around it, which is further encased by the flexible rubber on both sides. Driven by a servomotor, the fin can oscillate at its base with the oscillation angle given by

$$\theta(t) = \theta_A \sin(\omega_\theta t), \tag{5.8}$$

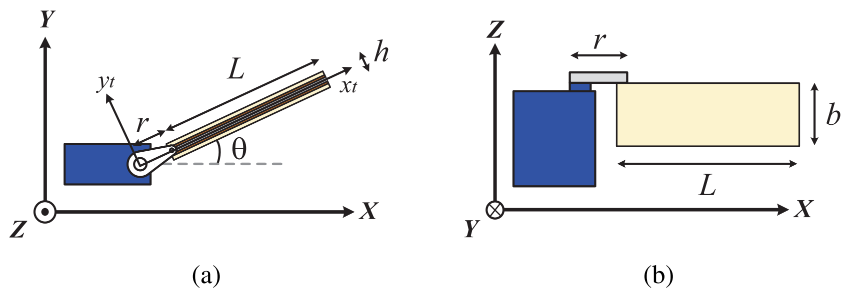

Figure 5.5: Schematic for actuation of the ER fluid-filled caudal fin. (a) Top view, (b) side view.

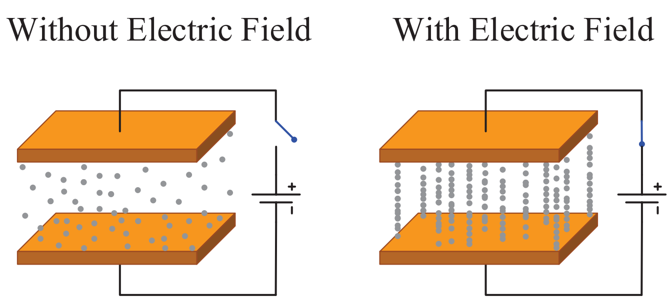

Figure 5.6: ER fluid reaction to the electric field.

where θ_A is the amplitude (in degree) and ω_θ is the angular frequency of the fin actuation. Fig. 5.5 shows the actuation schematic for the fin, which has a length of L, thickness of h, and depth of b.

5.2.2.1 ER Fluid

An ER fluid is a type of smart fluid that changes rheological properties in the presence of an electric field. Typically an ER fluid consists of a non-polar liquid with dielectric particles suspended in it. As illustrated in Fig. 5.6, the fluid changes state from liquid (in the absence of an electric field) to a solid gel form (in the presence of a strong electric field), when the suspended particles are aligned with the lines of the electric field [149, 150].

When filled in a multi-layer beam configuration, the fluid functions in its pre-yield (static) regime and behaves as a viscoelastic material [151, 152]. Therefore, its property can be modeled with a parameter called complex shear modulus (G^*). The linear relationship between shear stress,

τ, and shear strain, γ, is as follows:

$$\tau = G^* \gamma \tag{5.9}$$

where G^* is a function of the electric field and consists of a storage modulus (G') and a loss modulus (G'') [144]:

$$G^* = G' + iG'' \tag{5.10}$$

5.2.2.2 Multi-layer Beam

To model the flexible fin filled with ER fluid, first, some kinematic relationships need to be defined. We make a few assumptions to simplify these kinematic relationships: There is no slippage between the ER fluid layer and the electrodes; the transverse displacement (along the y_t-axis) is the same for all the layers; there is no normal stress in the ER fluid layer and there is no shear strain in the electrodes or in the rubber layers; the rubber and copper layers are bonded perfectly, resulting in the same displacement in longitudinal direction. Therefore, the shear strain, γ, and the longitudinal deflection of the ER fluid layer, u_3, is expressed as follows [147, 148]

$$\gamma = \frac{u_1 - u_5}{h_3} + \frac{h}{h_3}\frac{\partial w}{\partial x}, \tag{5.11}$$

$$u_3 = \frac{u_1 + u_5}{2} + \frac{(h_1 + h_2) - (h_4 + h_5)}{4}\frac{\partial w}{\partial x}, \tag{5.12}$$

where u_k ($k = 1, \cdots, 5$) are the longitudinal displacements of the mid-plane of the kth layer with ($u_1 = u_2$) and ($u_4 = u_5$), w is the transverse displacement of the beam, h_k ($k = 1, \cdots, 5$) is the thickness of the kth layer, with $h = h_1/2 + h_2 + h_3 + h_4 + h_5/2$, and $\frac{\partial w}{\partial x}$ is the deflection angle. A schematic of a portion of the ER fluid-filled flexible fin, in a deflected configuration, is shown in Fig. 5.7.

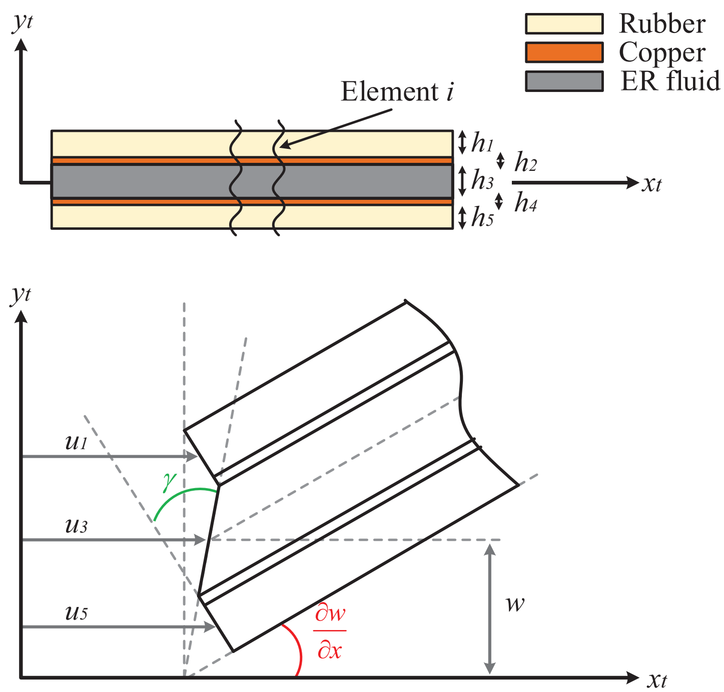

Figure 5.7: Schematics of the deflected ER fluid-filled flexible fin.

The governing equations of motion for the variable stiffness flexible fin filled with ER fluid are obtained using the Hamilton's principle, which is described as follows

$$\int_{t_1}^{t_2} \delta(T - U + W)dt = 0, \tag{5.13}$$

where T is the kinetic energy, U is the potential energy, W is the work done by external loads, and δ is the variational operator throughout the flexible caudal fin. The kinetic energy is determined as

$$T = \frac{1}{2}\int_0^L \sum_{k=1}^{5} \rho_k A_k \dot{r}_k^T \dot{r}_k \, dx + \frac{1}{2} J\dot{\theta}^2, \tag{5.14}$$

where ρ_k is the density of the kth layer, A_k is the cross-sectional area of the kth layer ($A_k = b_k h_k$), where $k = 1, \cdots, 5$, L denotes the length of the fin, and J is the moment of inertia associated with the servomotor actuation. The velocity vector $\dot{r}_k$ is defined as

$$\dot{r}_k = (\dot{u}_k - w\dot{\theta})\hat{x}_t + (x\dot{\theta} + u_k\dot{\theta} + \dot{w})\hat{y}_t, \tag{5.15}$$

where $\hat{x}_t$ and $\hat{y}_t$ are the unit vectors in the x_t and y_t directions, respectively.

The potential energy is calculated as follows

$$\begin{aligned} U = \frac{1}{2}\int_0^L \Bigg[\sum_{k=1,2,4,5} \Big(E_k A_k (\frac{\partial u_k}{\partial x})^2 + E_k I_k (\frac{\partial^2 w}{\partial x^2})^2 \Big) + G^* A_3 \gamma^2 \\ + mb\dot{\theta}^2 [\frac{1}{2}(L^2 - x^2) + r(L-x)](\frac{\partial w}{\partial x})^2 \Bigg] \mathrm{d}x, \end{aligned} \tag{5.16}$$

where E_k is the Young's modulus of the kth layer, I_k is the moment of inertia of the kth layer, m is the total mass of the fin, x is the distance from fixed end of the fin, and r is the servo arm length.

The total work done by the external forces (servo arm and hydrodynamic forces) are defined as follows

$$W = \tau\theta + \int_0^L f_h \, w \quad \mathrm{d}x + \left(F_{h_L - x} u_3 + F_{h_L - y} w \right)\Big|_{x=L}, \tag{5.17}$$

where τ is the rotational torque from the servomotor and the hydrodynamic forces f_h and F_{h_L} are determined base on Lighthill's large-amplitude elongated-body theory.

By substituting Eqs. (5.14), (5.16), and (5.17) into Eq. (5.13), we obtain the dynamic equations of motion:

$$
\begin{aligned}
&(\rho_1 A_1 + \rho_2 A_2 + \frac{1}{4}\rho_3 A_3)\ddot{u}_1 + \frac{1}{4}\rho_3 A_3 \ddot{u}_5 \\
&\qquad - 2(\rho_1 A_1 + \rho_2 A_2 + \frac{1}{2}\rho_3 A_3) w\ddot{\theta} \\
&\qquad - 3(\rho_1 A_1 + \rho_2 A_2 + \frac{1}{2}\rho_3 A_3) \dot{w}\dot{\theta} \\
&\qquad - (\rho_1 A_1 + \rho_2 A_2)(r + x + u_1)\dot{\theta}^2 \\
&\qquad - \frac{1}{2}\rho_3 A_3 (r + x + \frac{u_1 + u_5}{2})\dot{\theta}^2 \\
&\qquad + \frac{1}{2}(E_1 A_1 + E_2 A_2)\frac{\partial}{\partial u_1}\Big(\frac{\partial u_1}{\partial x}\Big)^2 \\
&\qquad + \frac{G^* A_3}{h_3^2}(u_1 - u_5) = 0,
\end{aligned}
\tag{5.18}
$$

$$
\begin{aligned}
&(\frac{1}{4}\rho_3 A_3 + \rho_4 A_4 + \rho_5 A_5)\ddot{u}_5 + \frac{1}{4}\rho_3 A_3 \ddot{u}_1 \\
&\qquad - 2(\frac{1}{2}\rho_3 A_3 + \rho_4 A_4 + \rho_5 A_5) w\ddot{\theta} \\
&\qquad - 3(\frac{1}{2}\rho_3 A_3 + \rho_4 A_4 + \rho_5 A_5) \dot{w}\dot{\theta} \\
&\qquad - (\rho_4 A_4 + \rho_5 A_5)(r + x + u_5)\dot{\theta}^2 \\
&\qquad - \frac{1}{2}\rho_3 A_3 (r + x + \frac{u_1 + u_5}{2})\dot{\theta}^2 \\
&\qquad + \frac{1}{2}(E_4 A_4 + E_5 A_5)\frac{\partial}{\partial u_5}\Big(\frac{\partial u_5}{\partial x}\Big)^2 \\
&\qquad - \frac{G^* A_3}{h_3^2}(u_1 - u_5) = 0,
\end{aligned}
\tag{5.19}
$$

$$
\begin{aligned}
&(\rho_1 A_1 + \rho_2 A_2 + \rho_3 A_3 + \rho_4 A_4 + \rho_5 A_5)\ddot{w} \\
&\quad + (\rho_1 A_1 + \rho_2 A_2)(x + r + u_1)\ddot{\theta} \\
&\quad + (\rho_4 A_4 + \rho_5 A_5)(x + r + u_5)\ddot{\theta} \\
&\quad + \rho_3 A_3 (x + r + \frac{u_1 + u_5}{2})\ddot{\theta} \\
&\quad + 3(\rho_1 A_1 + \rho_2 A_2)\dot{u}_1 \dot{\theta} + 3(\rho_4 A_4 + \rho_5 A_5)\dot{u}_5 \dot{\theta} \\
&\quad + \rho_3 A_3 (\frac{\dot{u}_1 + \dot{u}_5}{2})\dot{\theta} \\
&\quad - (\rho_1 A_1 + \rho_2 A_2 + \rho_3 A_3 + \rho_4 A_4 + \rho_5 A_5) w \dot{\theta}^2 \\
&\quad + \frac{1}{2}(E_1 I_1 + E_2 I_2 + E_4 I_4 + E_5 I_5)\frac{\partial}{\partial w}\left(\frac{\partial^2 w}{\partial x^2}\right)^2 \\
&\quad + \frac{1}{2} m b \dot{\theta}^2 \left[\frac{1}{2}(L^2 - x^2) + r(L - x)\right]\frac{\partial}{\partial w}\left(\frac{\partial w}{\partial x}\right)^2 \\
&\quad + G^* A_3 \frac{h^2}{h_3^2}\frac{\partial}{\partial w}\left(\frac{\partial w}{\partial x}\right)^2 - f_h w \\
&\quad + \left(F_{h_L - x} u_3 + F_{h_L - y} w\right)\Big|_{x=L} = 0.
\end{aligned}
\tag{5.20}
$$

5.2.2.3 Discretization using Finite Element Method (FEM)

The equations of motion (Eqs. (5.18), (5.19), and (5.20)), which are coupled and nonlinear, are solved using finite element method [146–148]. Each element consists of two nodes, and each node has four degrees of freedom. Node displacements of element i are formed by the following vector which is bounded between nodes j and k (with $k = j + 1$):

$$
\mathbf{q}_i = \left[u_{1j}\ \ u_{5j}\ \ w_j\ \ \frac{\partial w_j}{\partial x}\ \ u_{1k}\ \ u_{5k}\ \ w_k\ \ \frac{\partial w_k}{\partial x}\right]^T. \tag{5.21}
$$

A schematic of the flexible fin elements and nodes, and the details of one element are shown in Fig. 5.8.

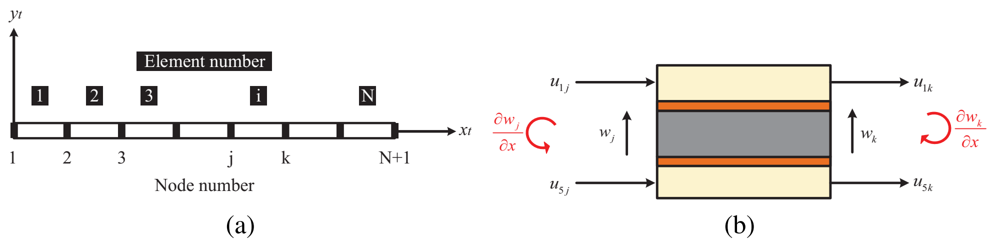

Figure 5.8: Schematic of the flexible fin in FEM: (a) Configuration of the element and node numbers, (b) element i, its two nodes, and degrees of freedom.

The deflection vector, represented in terms of the node deflection vector, is given by

$$[u_1 \;\; u_3 \;\; u_5 \;\; w \;\; \frac{\partial w}{\partial x} \;\; \gamma]^T = [N_1 \;\; N_2 \;\; N_3 \;\; N_4 \;\; N_5 \;\; N_6]^T \mathbf{q}_i, \tag{5.22}$$

where FEM shape functions N_1, N_2, N_3, N_4, N_5 and N_6 are defined as

$$N_1 = [1-\xi \quad 0 \quad 0 \quad 0 \quad \xi \quad 0 \quad 0 \quad 0], \tag{5.23}$$

$$N_2 = \frac{1}{2}(N_1 + N_3), \tag{5.24}$$

$$N_3 = [0 \quad 1-\xi \quad 0 \quad 0 \quad 0 \quad \xi \quad 0 \quad 0], \tag{5.25}$$

$$N_4 = [0 \quad 0 \quad 1-3\xi^2+2\xi^3 \quad (\xi-2\xi^2+\xi^3)L_i \tag{5.26}$$

$$0 \quad 0 \quad 3\xi^2-2\xi^3 \quad (-\xi^2+\xi^3)L_i], \tag{5.27}$$

$$N_5 = [\frac{\partial N_4}{\partial x}], \tag{5.28}$$

$$N_6 = [\frac{N_1 - N_3}{h_3} + \frac{h}{h_3} N_5], \tag{5.29}$$

where $\xi = \frac{x}{L_i}$, with L_i being the length of each element.

Applying the FEM presented in Eq. (5.22) to the Hamilton's principle, we obtain the dynamic equation of motion at the elemental level:

$$\mathbf{M}_i\ddot{\mathbf{q}}_i + 2\dot{\theta}\mathbf{C}_i\dot{\mathbf{q}}_i + \mathbf{K}_i\mathbf{q}_i = \mathbf{F}_i, \tag{5.30}$$

where $\mathbf{M}_i$ is the element mass matrix, $\mathbf{C}_i$ is the element gyroscopic effect matrix, $\mathbf{K}_i$ is the element stiffness matrix, and $\mathbf{F}_i$ is the element force matrix, which are formed as follows:

$$\mathbf{M}_i = \int_0^{L_i} \sum_{k=1}^{5} \left[\rho_k A_k (N_k^T N_k + N_4^T N_4)\right] \, \mathrm{d}x, \tag{5.31}$$

$$\mathbf{C}_i = \int_0^{L_i} \sum_{k=1}^{5} \left[\rho_k A_k (N_k^T N_4 - N_k N_4^T)\right] \, \mathrm{d}x + \int_0^{L_i} G'' A_3 N_6^T N_6 \, \mathrm{d}x, \tag{5.32}$$

$$\mathbf{K}_i = \mathbf{K}_{i-1} + \dot{\theta}^2(\mathbf{K}_{i-2} - \mathbf{M}_i) - \ddot{\theta}\mathbf{C}_i, \tag{5.33}$$

where

$$\begin{aligned}\mathbf{K}_{i-1} &= \int_0^{L_i} \sum_{k=1,2,4,5} \left[(E_k A_k N_{k,x}^T N_{k,x} + E_k I_k N_{4,xx}^T N_{4,xx})\right] \, \mathrm{d}x \\ &\quad + \int_0^{L_i} G' A_3 N_6^T N_6 \, \mathrm{d}x, \end{aligned} \tag{5.34}$$

$$\begin{aligned}\mathbf{K}_{i-2} &= \frac{1}{2}\int_0^{L_i} \Big(\sum_{k=1}^{5} \rho_k A_k\Big)\big[L^2 - (x_i + x)^2\big] N_5^T N_5 \, \mathrm{d}x \\ &\quad + r\int_0^{L_i} \Big(\sum_{k=1}^{5} \rho_k A_k\Big)\big[L - (x_i + x)\big] N_5^T N_5 \, \mathrm{d}x, \end{aligned} \tag{5.35}$$

$$
\begin{aligned}
\mathbf{F}_i = \int_0^{L_i} \Bigg\{ & \sum_{k=1}^{5} \left[\rho_k A_k \dot{\theta}^2 (r + x_i + x) N_k^T\right] \\
& - \sum_{k=1}^{5} \left[\rho_k A_k \ddot{\theta}^2 (r + x_i + x) N_4^T\right] \\
& + f_h N_4^T \Bigg\} \, \mathrm{d}x + \left(F_{h_L - x} u_3 + F_{h_L - y} w\right)\Big|_{i=N}.
\end{aligned} \tag{5.36}
$$

The final equation of motion, resulting from a standard FEM assembly procedure, is formed as follows

$$
\mathbf{M}\ddot{\mathbf{q}} + 2\dot{\theta}\mathbf{C}\dot{\mathbf{q}} + \mathbf{K}\mathbf{q} = \mathbf{F}, \tag{5.37}
$$

with u_1, u_5, w, and $\frac{\partial w}{\partial x}$ being zero at the base of the beam.

5.3 Experimental Results

5.3.1 Identification of Shear Modulus Values

The detailed specifications of the designed beam are presented in Section 5.1. Other than those physical specifications, the ER fluid has a complex shear modulus, G^*, that needs to be identified for the system at each electric field level. To do so, a set of experiments are conducted on the prototyped beam. The ER fluid-filled beam is clamped to a standard precision dovetail Z-axis stage (ZDTLS80, Misumi USA) via a custom-made 3D-printed platform. A laser sensor (Baumer Electric, OADM 20I6441/A14F) is attached to a standard precision dovetail XY-axis stage (XY-DTS90, Misumi USA). The two stages are fixed on a setup plate (Misumi USA), so that the laser is pointed at the center tip of the flexible fin. The laser sensor output is captured by a dSPACE system (RTI 1104, dSPACE). A high voltage generator power module (Input voltage: 3 V, output voltage: 7 kV, Sunkee, China) is used to generate the desired electric field. For the experiment, the

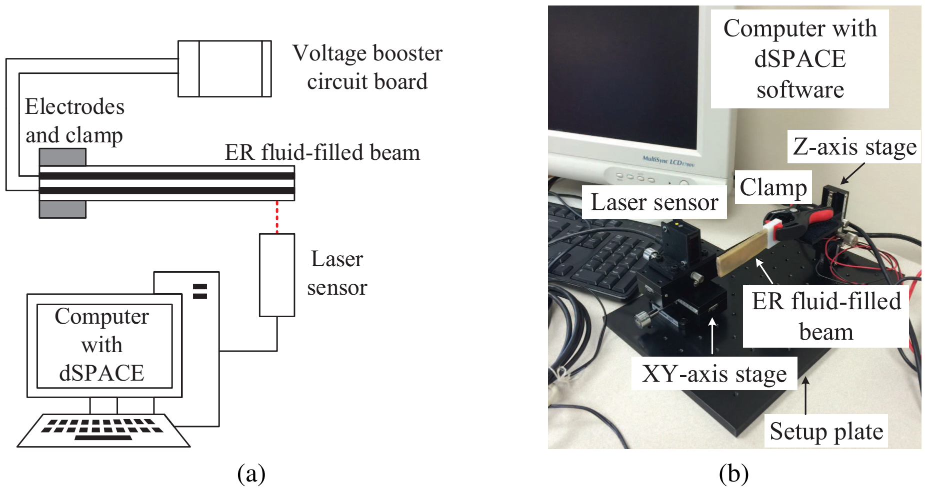

Figure 5.9: Experimental setup for observing passive, damped vibration of the ER fluid-filled flexible fin under different electric fields. (a) Schematic, (b) actual.

beam is deflected manually around 1 cm at the tip and then released, so the displacement of the tip is recorded using the laser sensor as the beam oscillates. The experiment is repeated 20 times for each electric field value. The experimental setup is shown in Fig. 5.9.

From the recorded signals, the natural frequency and the damping ratio of the beam for the given electric field are extracted, which are subsequently used to identify the corresponding G^*. The damping ratio, ζ, is calculated from the two consecutive peaks of the recorded signal (X_c and X_{c+1}, respectively), as follows:

$$\zeta = \sqrt{\frac{1}{\left(\frac{2\pi}{\ln\left(\frac{X_c}{X_{c+1}}\right)}\right)^2}}. \tag{5.38}$$

The natural frequency, f_n, is obtained from the time instances of two consecutive peaks (T_c and T_{c+1}, respectively) of the recorded signal, as follows:

$$f_n = \frac{1}{(T_{c+1} - T_c)\sqrt{1-\zeta^2}}. \tag{5.39}$$

To identify the parameters G' and G'', we use exhaustive search in range [0, 50000] for G' and [0,

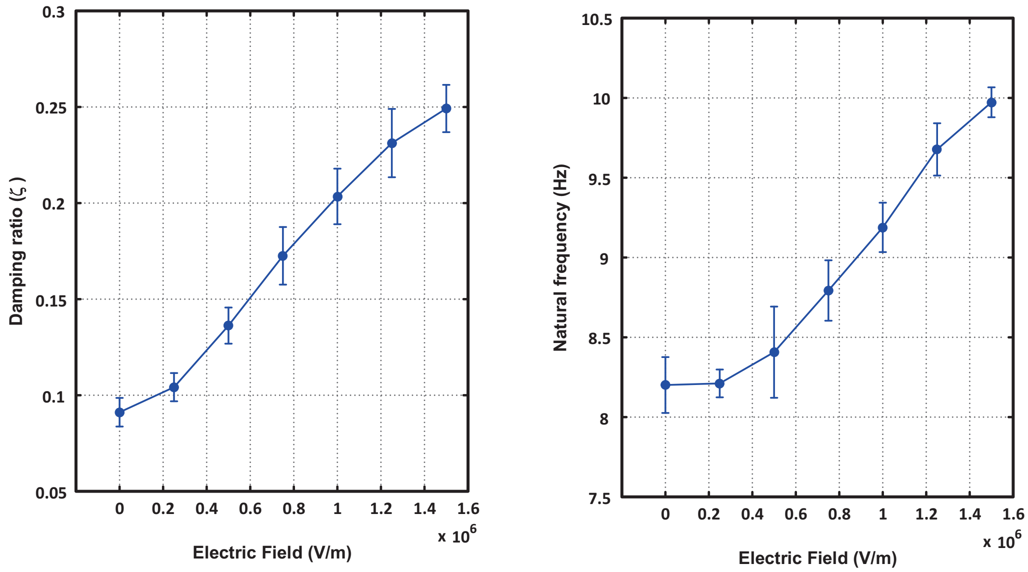

Figure 5.10: Identified parameters under different electric fields in the air. (a) Damping ratio, (b) natural frequency.

5000] for G''. Specifically, we start with a coarse grid and evaluated the resulting normalized error by

$$J = \left[\left(\frac{f_n^{\text{Sim}} - f_n^{\text{Exp}}}{f_n^{\text{Exp}}} \right)^2 + \left(\frac{\zeta^{\text{Sim}} - \zeta^{\text{Exp}}}{\zeta^{\text{Exp}}} \right)^2 \right] \tag{5.40}$$

After finding the minimum value for J, we search in a finer grid around the corresponding G' and G''. This procedure is repeated until the error drops bellow 5% for both ζ and f_n. Fig. 5.10(a) and (b) show the empirical damping ratio, ζ, and natural frequency, f_n, for different electric fields, respectively. The damping ratio increases from 0.09 to 0.25 (170% change) and the natural frequency increases from 8.1 Hz to 10.1 Hz (25% change), when the electric field is increased from 0 V/m to 1.5×10^6 V/m. One can see how increasing the electric field affects the performance of the beam. In the absence of the electric field, the fin is at its most flexible configuration, and thus has the lowest natural frequency. By increasing the electric field, the natural frequency and damping ratio of the flexible fin increases, and it becomes stiffer.

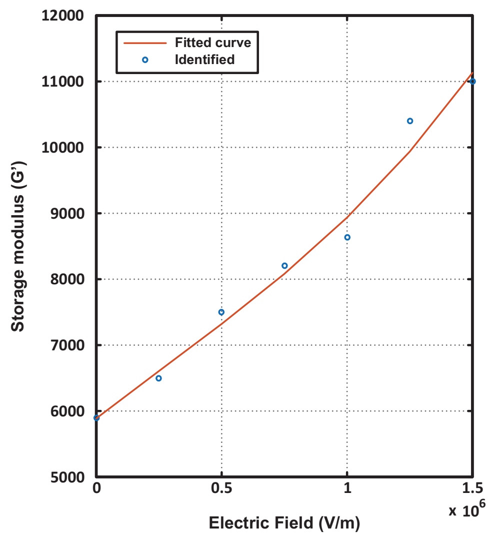

(a)

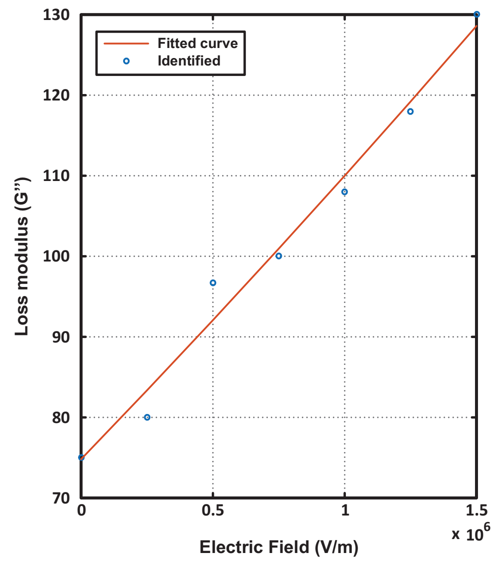

(b)

Figure 5.11: Identified complex shear modulus values and the fitted curve under different electric fields. (a) Storage modulus (G'), (b) loss modulus (G'').

The storage modulus G' and the loss modulus G'' are identified to be

$$G' = 10^3 \times (0.053E_f^3 - 0.043E_f^2 + 0.295E_f + 0.588), \tag{5.41}$$

$$G'' = 1.33E_f^2 + 33.8E_f + 74.8, \tag{5.42}$$

where E_f is the electric field applied to the ER fluid. Figs. 5.11 shows the identified complex shear modulus values and the fitted curve under different electric fields. Matlab command `polyfit` is used to fit a third order polynomial to the identified storage modulus and a second order polynomial to the identified loss modulus. These parameters are used throughout simulation of all other experimental settings (passive damped oscillations and base-actuated rotations) discussed in the rest of this section. Fig. 5.12 shows both the simulation and experimental data on the tip displacement of ER fluid-filled flexible fin for different electric field values.

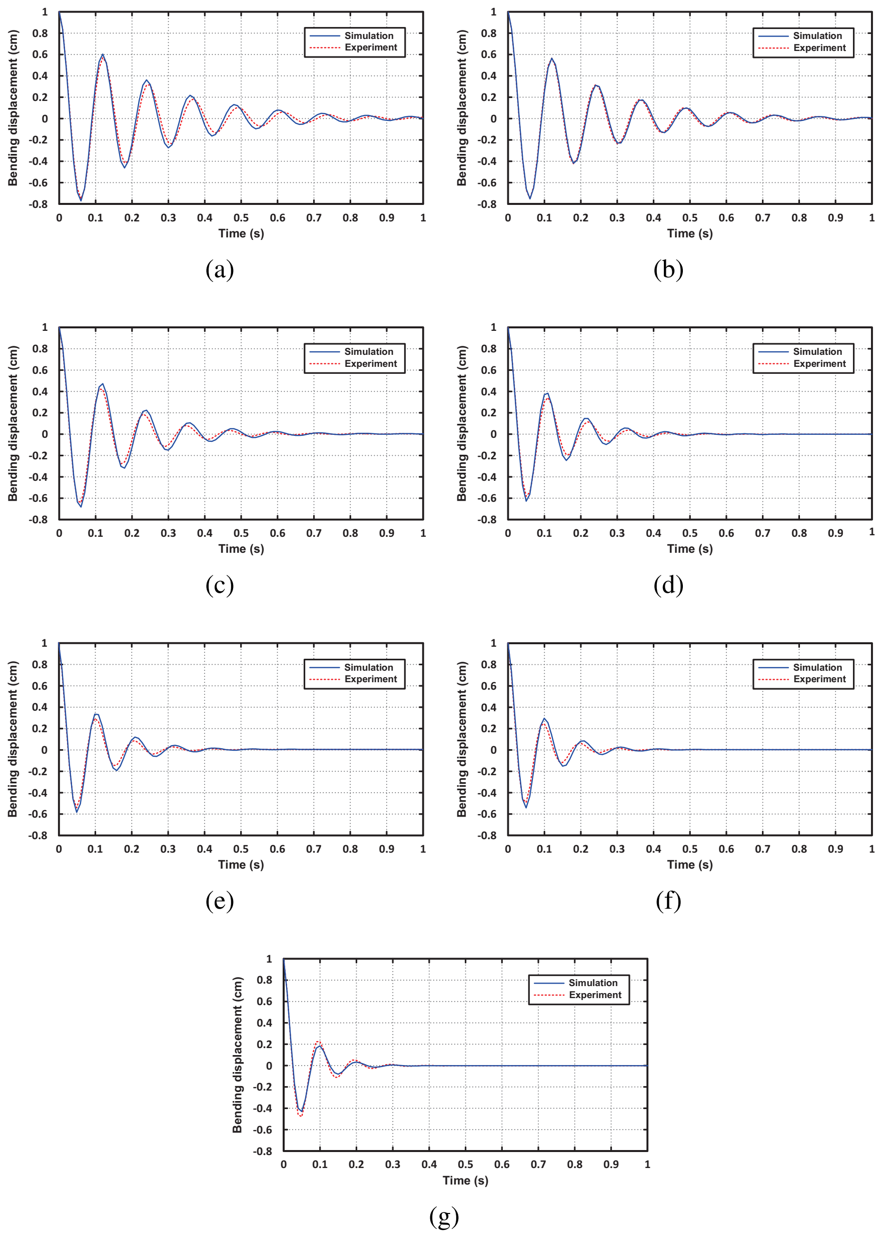

Figure 5.12: A sample of experimentally measured damped oscillations of the beam tip, along with simulation results corresponding to the matched parameters, for each applied electric field. (a) $E_f = 0\ \frac{\mathrm{V}}{\mathrm{m}}$, (b) $E_f = 0.25\times10^6\ \frac{\mathrm{V}}{\mathrm{m}}$, (c) $E_f = 0.5\times10^6\ \frac{\mathrm{V}}{\mathrm{m}}$, (d) $E_f = 0.75\times10^6\ \frac{\mathrm{V}}{\mathrm{m}}$, (e) $E_f = 1\times10^6\ \frac{\mathrm{V}}{\mathrm{m}}$, (f) $E_f = 1.25\times10^6\ \frac{\mathrm{V}}{\mathrm{m}}$, (g) $E_f = 1.5\times10^6\ \frac{\mathrm{V}}{\mathrm{m}}$.

5.3.2 Identification of Hydrodynamic Coefficients

A similar set of experiments, but with the proposed stiffness-tuning fin submersed in water, are conducted to identify the complex hydrodynamic coefficient, Γ, in Eq. (5.6). The experimental

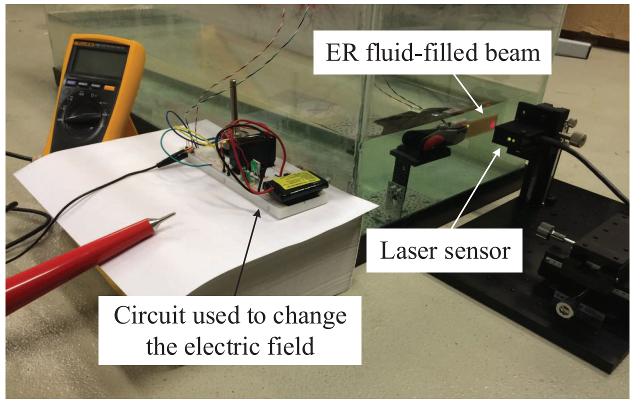

Figure 5.13: Experimental setup for measuring damped oscillations of the flexible fin in water.

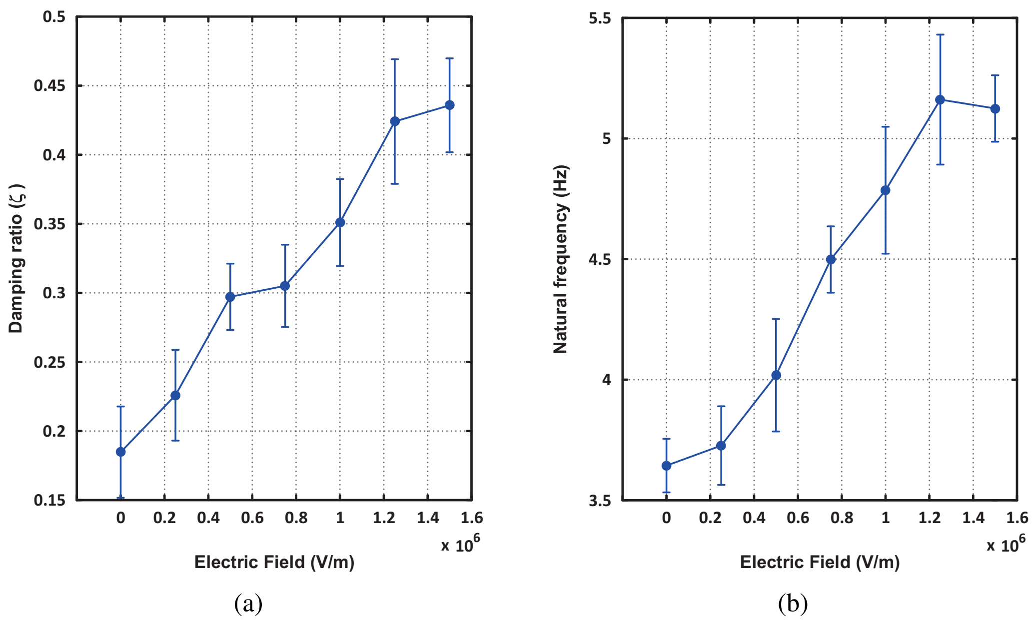

Figure 5.14: Identified parameters under different electric fields in water. (a) Damping ratio, (b) natural frequency.

setup is shown in Fig. 5.13. The beam is deflected manually around 1 cm at the tip and then released to generate passive, damped oscillations, which are recorded using the laser sensor. The experiment is repeated 20 times for each electric field value. The natural frequency and the damping ratio are extracted from the recorded signal, and are matched to the ones from the simulation to identify the complex hydrodynamic coefficient. Fig. 5.14(a) and (b) show the empirical damping ratio, ζ, and natural frequency, f_n, for different electric fields, respectively, when the beam is in water. The damping ratio increases from 0.18 to 0.42 (130% change) and the natural frequency increases from 3.64 Hz to 5.12 Hz (40% change), when the electric field is increased from 0 V/m to 1.5×10^6 V/m. Note that the natural frequency and damping ratio decrease when the beam is submersed in water (versus the case when it is in air). The same procedure as described in Section 5.3.1 is applied to find complex hydrodynamic coefficient, $\Gamma = \Gamma' + i\Gamma''$, with range [0, 10] for both Γ' and Γ''. The identified values of Γ are closed to each other for all the tested electric field values; therefore, we consider the mean value among all the electric fields to be our complex hydrodynamic coefficient. This complex hydrodynamic coefficient, Γ, is identified to be

$$\Gamma = 4.31 + i3.84 \tag{5.43}$$

Note that the complex shear modulus used in these simulations is identified as discussed in Section 5.3.1.

Fig. 5.15 shows the comparison of experimentally observed damped oscillations with the simulated ones using the identified hydrodynamic coefficient, where we can see that they match well.

5.3.3 Base Actuation Experiments for Model Validation

The last set of experiments involve actuating the flexible fin in water on its base with a servomotor, emulating the configuration of an anchored robotic fish flapping its tail. The purpose is to examine the stiff-tuning behavior in this new setting and to validate the identified dynamic model with independent experiments. The flexible fin is actuated with a waterproof servo (HS-5086WP from Hitec), fixed in the tank, and the motion of the fin is recorded from above using a high-speed camera (Casio Exilim EX-FH25) at 120 frames/s. The experimental setup is shown in Fig. 5.16.

Fig. 5.17 compares the measured time-dependent beam shapes and those predicted by the dy-

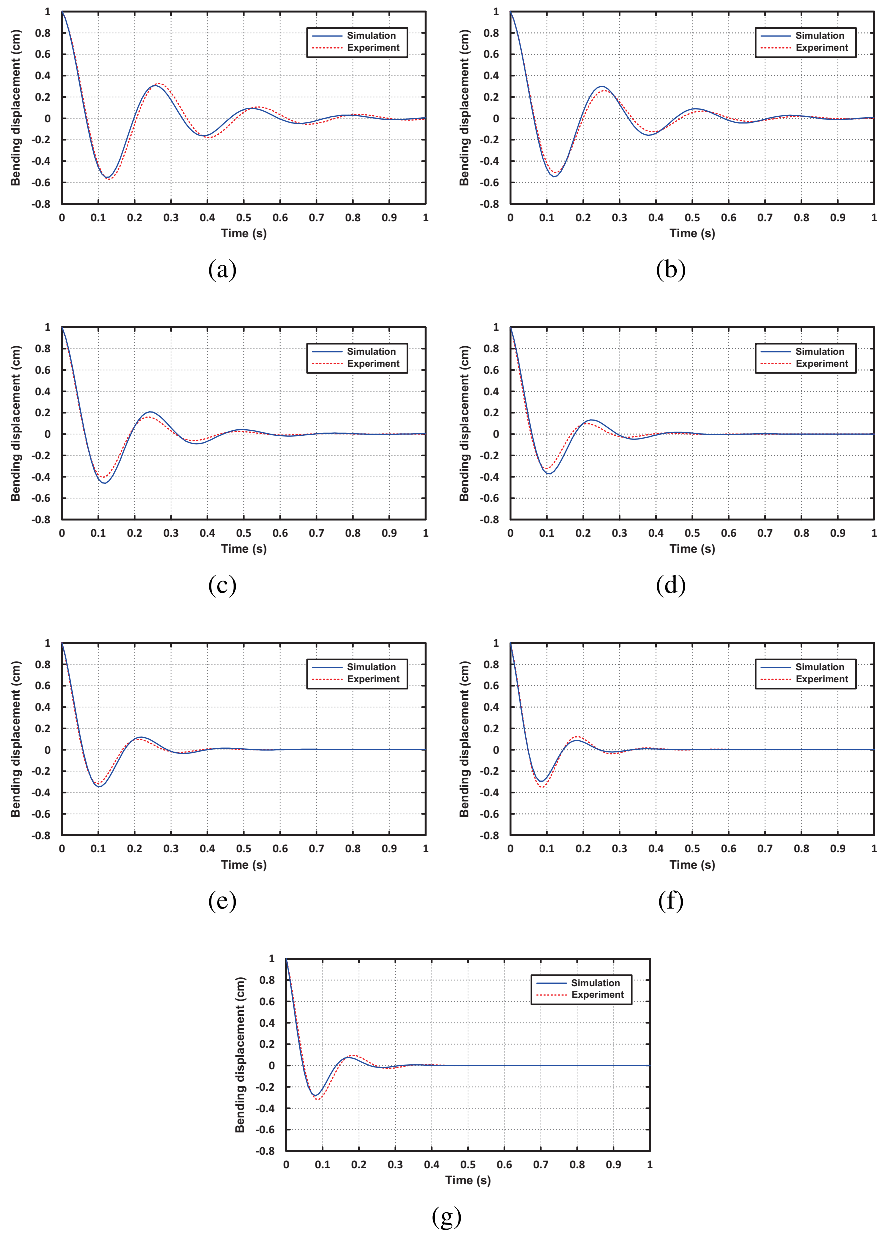

Figure 5.15: Passive, damped vibration of the ER fluid filled flexible beam in water: (a) $E_f = 0\ \frac{\mathrm{V}}{\mathrm{m}}$, (b) $E_f = 0.25 \times 10^6\ \frac{\mathrm{V}}{\mathrm{m}}$, (c) $E_f = 0.5 \times 10^6\ \frac{\mathrm{V}}{\mathrm{m}}$, (d) $E_f = 0.75 \times 10^6\ \frac{\mathrm{V}}{\mathrm{m}}$, (e) $E_f = 1 \times 10^6\ \frac{\mathrm{V}}{\mathrm{m}}$, (f) $E_f = 1.25 \times 10^6\ \frac{\mathrm{V}}{\mathrm{m}}$, (g) $E_f = 1.5 \times 10^6\ \frac{\mathrm{V}}{\mathrm{m}}$

namic model for fin-beat amplitude of 22.5° and frequency of 2 Hz, for two different electric fields, 0 V/m (Fig. 5.17(a) and (b)) and 1.5×10^6 V/m (Fig. 5.17(c) and (d)). To be brief, we show the first and last frames of each half-cycle. It can be seen that, with an increasing electric field, the fin becomes stiffer and as a result, the tip displacement gets smaller, and good agreement between

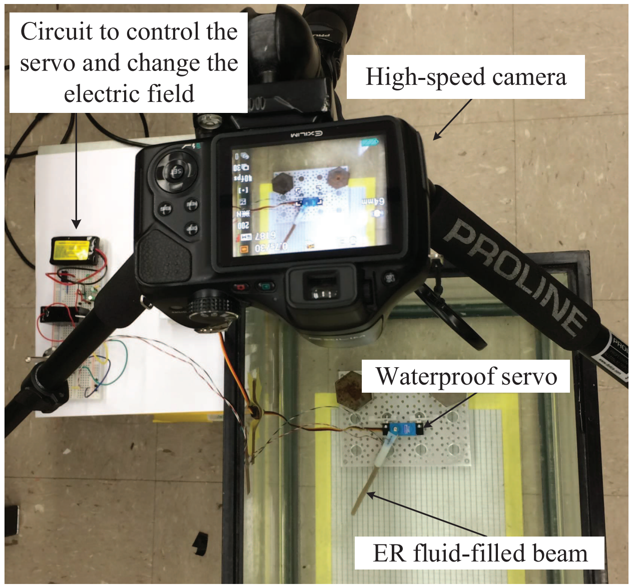

Figure 5.16: Experimental setup for measuring the fin shape under base actuation (top view).

the experimental and simulation results provides validation of the proposed dynamic model. The comparison of the simulated time-dependent ER fluid filled flexible beam tip displacements for the two electric field values is further shown in Fig. 5.17(e).

Finally, we conduct similar experiments with fin-beat frequency of 4 Hz, which is close to the natural frequency of the fin in water. To achieve this flapping frequency, the amplitude of the servo motion is reduced to $\theta_A = 10°$, in order for the servo to under its actuation limit. The high-speed camera is set to record at 240 frames/s. Fig. 5.18 shows the comparison between experimental measurement of the time-dependent fin shapes with model predictions. Overall, the model-predicted beam shape trajectories match well with the model predictions. The discrepancy between the model prediction and the experimental measurement can be attributed to some limitations in the prototyping process. First, the fin was not perfectly symmetric and there was a small difference between liquid urethane rubber thicknesses on two sides. There was no precise control on the amount of the rubber that leaked on the surface of the copper electrodes during the prototyping procedure, which resulted in another factor in breaking the symmetry. In addition, the

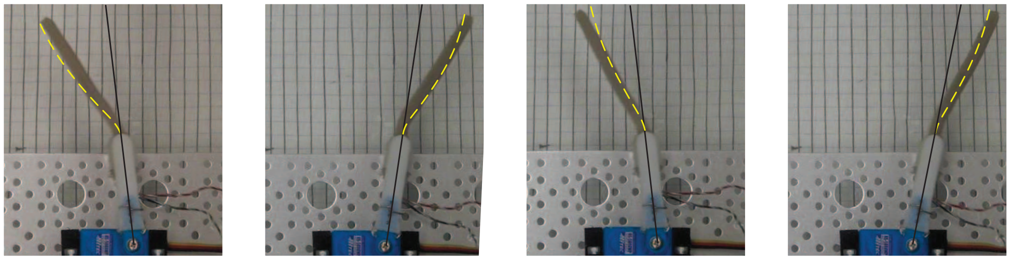

(a) (b) (c) (d)

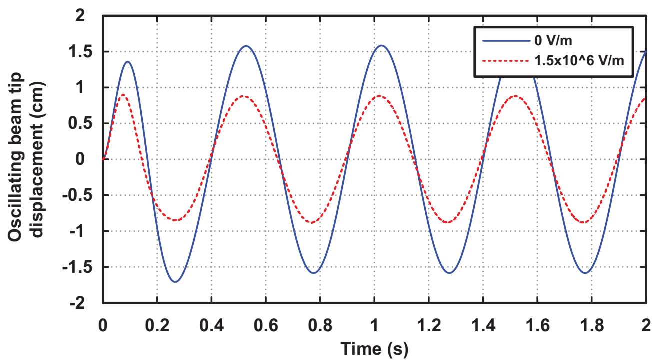

(e)

Figure 5.17: Base-actuated stiffness-tunable fin with fin-beat amplitude of 22.5° and frequency of 2 Hz: (a)-(b) Comparison between experimental measurement of the time-dependent beam shapes with model predictions, where the electric field applied to the beam is $E_f = 0\ \frac{\mathrm{V}}{\mathrm{m}}$, (c)-(d) comparison between experimental measurement of the time-dependent beam shapes with model predictions, where the electric field applied to the beam is $E_f = 1.5 \times 10^6\ \frac{\mathrm{V}}{\mathrm{m}}$, where the solid black line corresponds to the servo arm direction and the yellow dashed line represents the fin shape by the dynamic model, and (e) comparison between the simulated tip displacements under the two different electric fields.

bonding agent used to seal the two halves of the beam together was not considered in the modeling procedure. This bonding agent resulted in a stiffer beam than expected.

5.4 Conclusion

The goal of this work was to introduce a novel compact mechanism for a flexible fin with actively tunable stiffness. This was achieved by embedding ER fluid in flexible rubber, and it was demonstrated in experiments that the stiffness could be tuned at a fast speed. A dynamic model derived

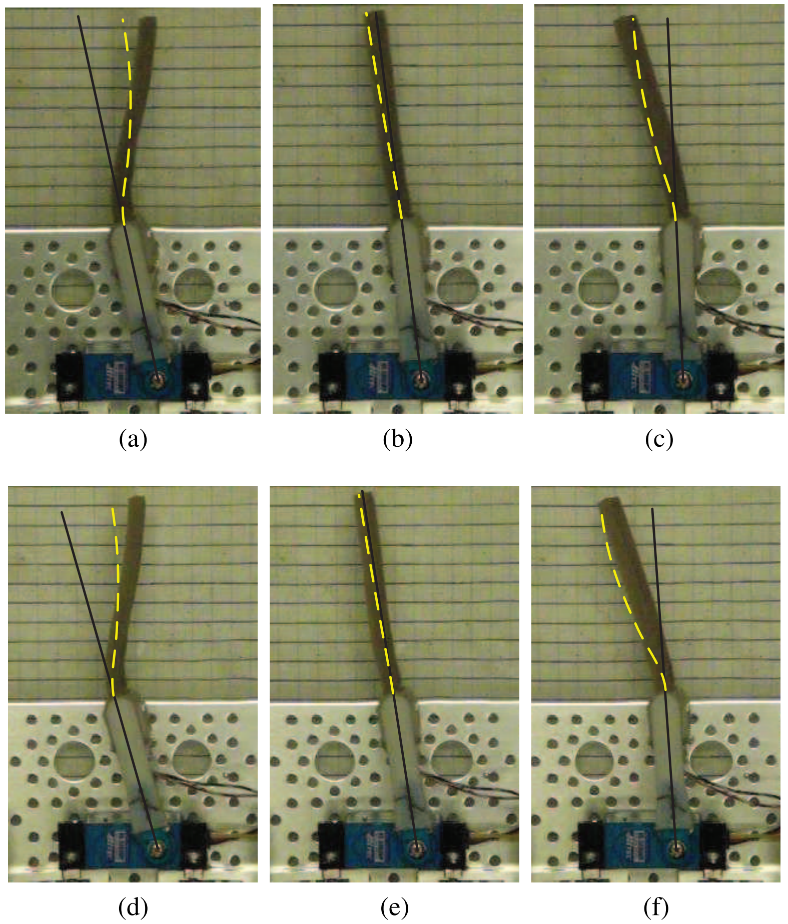

Figure 5.18: Base-actuated stiffness-tunable fin with fin-beat amplitude of 10° and frequency of 4 Hz: (a)-(c) Comparison between experimental measurement of the time-dependent beam shapes with model predictions, where the electric field applied to the beam is $E_f = 0\ \frac{\mathrm{V}}{\mathrm{m}}$, (d)-(f) comparison between experimental measurement of the time-dependent beam shapes with model predictions, where the electric field applied to the beam is $E_f = 1.5 \times 10^6\ \frac{\mathrm{V}}{\mathrm{m}}$, where the solid black line corresponds to the servo arm direction and the yellow dashed line represents the fin shape by the dynamic model.

using Hamilton's principle was proposed to capture the fin's behavior, where the hydrodynamic force on the fin was incorporated. The model parameters were identified with passive oscillation experiments in air and in water, and the model was further validated with base-actuation experiments emulating a flapping fin setting.

Chapter 6

Conclusions and Future Work

6.1 Concluding Remarks

Throughout this dissertation, we have investigated the design, development and dynamic modeling of flexible elments of a robotic fish, and studied the effect of flexibility on its performance.

First, the swimming performance and mechanical efficiency of flexible pectoral fins, connected to actuator shafts via rigid links, are studied, where it is found that flexible fins demonstrate advantages over rigid fins in speed and efficiency at relatively low fin-beat frequencies, while the rigid fins outperform the flexible fins at higher frequencies. The presented model offers a promising tool for the design of fin flexibility and swimming gait, to achieve speed and efficiency objectives for the robotic fish.

Second, a flexible passive rowing joint is proposed. This novel joint enables the pectoral fin to perform a symmetric rowing motion, as opposed to the traditional rigid joint, where one needs a faster power stroke and slower recovery stroke speed to have a net thrust (this fin flapping mechanism was used in Chapter 2). This joint allows the pectoral fin to sweep back passively during the recovery stroke while it follows the prescribed motion of the actuator during the power stroke, which results in net thrust even under symmetric actuation for power and recovery strokes. The flexibility of the joint is modeled as a pair of torsional spring and damper, and the blade element theory is used to evaluate the hydrodynamic forces. The dynamic model of a robotic fish equipped with such joints is developed and validated through extensive experiments. Motivated by the need for design optimization, the model is further utilized to investigate the influences of the joint length and stiffness on the robot locomotion performance and efficiency.

Third, an alternative flexible joint for pectoral fins is also proposed, which enables the pectoral fin to operate primarily in the rowing mode, while undergoing passive feathering during the recovery stroke to reduce hydrodynamic drag on the fin. Here, the pectoral fin undergoes a 3D motion, which results in calculation of hydrodynamic forces in 3D space. A dynamic model, verified experimentally, is developed to examine the trade-off between swimming speed and mechanical efficiency in the fin design.

Finally, we investigate flexible fins with actively tunable stiffness, enabled by electrorheological (ER) fluids. The tunable stiffness can be used in optimizing the robotic fish speed or maneuverability in different operating regimes. Fins with tunable stiffness are prototyped with ER fluids enclosed between layers of liquid urethane rubber (Vytaflex 10). Free oscillation and base-excited oscillation behaviors of the fins are measured underwater when different electric fields are applied for the ER fluid, which are subsequently used to develop a dynamic model for the stiffness-tunable fins.

6.2 Future Work

The investigation on the effect of flexibility on the performance of a robotic fish can be extended further. For the flexible passive joint, we considered rigid, rectangular pectoral fins; however, flexible pectoral fins with different sizes and shapes are worth further investigation. Another interesting problem is to combine the flexible passive rowing joint and flexible passive feathering joint designs, and explore the resulting performance. Interactions of flexible caudal fin and pectoral fins present interesting challenges, which can be studied further. For the stiffness-tunable fins, first, the fabrication procedure for the fin can be refined so that the limitations discussed in Section 5.3.3 are addressed. Also, the stiffness-tunable fin needs to be integrated with a free-swimming robotic fish, to investigate the active onboard control of stiffness when the robot operates in different regimes (fast/slow speeds, for example), for optimization of the swimming efficiency.

REFERENCES

REFERENCES

[1] C. C. Lindsey, "1 - Form, function, and locomotory habits in fish," in *Fish Physiology*, ser. Locomotion, W. S. Hoar and D. J. Randall, Eds. Academic Press, 1978, vol. 7, pp. 1–100.

[2] P. Valdivia y Alvarado and K. Youcef-Toumi, "Design of machines with compliant bodies for biomimetic locomotion in liquid environments," *Journal of Dynamic Systems, Measurement, and Control*, vol. 128, no. 1, pp. 3–13, Sep. 2005.

[3] T. Ichikizaki and I. Yamamoto, "Development of robotic fish with various swimming functions," in *Symposium on Underwater Technology (UT) and Workshop on Scientific Use of Submarine Cables and Related Technologies*, Tokyo, Japan, Apr. 2007, pp. 378–383.

[4] J. Yu, M. Tan, S. Wang, and E. Chen, "Development of a biomimetic robotic fish and its control algorithm," *IEEE Transactions on Systems, Man, and Cybernetics, Part B (Cybernetics)*, vol. 34, no. 4, pp. 1798–1810, Aug. 2004.

[5] R. W. Blake, *Fish Locomotion*. Cambridge: Cambridge University Press, May 1983.

[6] H. Wang, "Design and implementation of a biomimetic robotic fish," Masters Thesis, Concordia University, Montreal, Quebec, Canada, 2009.

[7] P. R. Bandyopadhyay, D. N. Beal, and A. Menozzi, "Biorobotic insights into how animals swim," *Journal of Experimental Biology*, vol. 211, no. 2, pp. 206–214, Jan. 2008.

[8] X. Tan, D. Kim, N. Usher, D. Laboy, J. Jackson, A. Kapetanovic, J. Rapai, B. Sabadus, and X. Zhou, "An autonomous robotic fish for mobile sensing," in *IEEE/RSJ International Conference on Intelligent Robots and Systems (IROS)*, Beijing, China, Oct. 2006, pp. 5424–5429.

[9] J. Liu and H. Hu, "Biological inspiration: From carangiform fish to multi-joint robotic fish," *Journal of Bionic Engineering*, vol. 7, no. 1, pp. 35–48, Mar. 2010.

[10] J. M. Anderson, K. Streitlien, D. S. Barrett, and M. S. Triantafyllou, "Oscillating foils of high propulsive efficiency," *Journal of Fluid Mechanics*, vol. 360, pp. 41–72, Apr. 1998.

[11] M. Sfakiotakis, D. M. Lane, and J. B. C. Davies, "Review of fish swimming modes for aquatic locomotion," *IEEE Journal of Oceanic Engineering*, vol. 24, no. 2, pp. 237–252, Apr. 1999.

[12] M. S. Triantafyllou, G. S. Triantafyllou, and D. K. P. Yue, "Hydrodynamics of fishlike swimming," *Annual Review of Fluid Mechanics*, vol. 32, no. 1, pp. 33–53, 2000.

[13] X. Tan, "Autonomous robotic fish as mobile sensor platforms: Challenges and potential solutions," *Marine Technology Society Journal*, vol. 45, no. 4, pp. 31–40, Jul. 2011.

[14] F. Zhang, O. Ennasr, E. Litchman, and X. Tan, "Autonomous sampling of water columns using gliding robotic fish: Algorithms and harmful-algae-sampling experiments," *IEEE Systems Journal*, vol. 10, no. 3, pp. 1271–1281, Sep. 2016.

[15] S. Marras and M. Porfiri, "Fish and robots swimming together: attraction towards the robot demands biomimetic locomotion," *Journal of The Royal Society Interface*, vol. 9, no. 73, pp. 1856–1868, Aug. 2012.

[16] C. M. Breder, *The Locomotion of Fishes*, ser. Aquarium nature series. New York, USA: New York Zoological Society, 1926.

[17] J. N. Newman and T. Y. Wu, "Hydromechanical aspects of fish swimming," in *Swimming and Flying in Nature*, T. Y.-T. Wu, C. J. Brokaw, and C. Brennen, Eds. Springer US, 1975, pp. 615–634, dOI: 10.1007/978-1-4757-1326-8.

[18] G. V. Lauder and J. L. Tangorra, "Fish locomotion: Biology and robotics of body and fin-based movements," in *Robot Fish*, ser. Springer Tracts in Mechanical Engineering, R. Du, Z. Li, K. Youcef-Toumi, and P. V. y. Alvarado, Eds. Berlin Heidelberg: Springer, 2015, pp. 25–49, dOI: 10.1007/978-3-662-46870-8.

[19] V. Kopman and M. Porfiri, "Design, modeling, and characterization of a miniature robotic fish for research and education in biomimetics and bioinspiration," *IEEE/ASME Transactions on Mechatronics*, vol. 18, no. 2, pp. 471 – 483, Apr. 2013.

[20] J. Wang and X. Tan, "A dynamic model for tail-actuated robotic fish with drag coefficient adaptation," *Mechatronics*, vol. 23, no. 6, pp. 659–668, Sep. 2013.

[21] S. Bazaz Behbahani, J. Wang, and X. Tan, "A dynamic model for robotic fish with flexible pectoral fins," in *IEEE/ASME International Conference on Advanced Intelligent Mechatronics (AIM)*, Wollongong, Australia, Jul. 2013, pp. 1552–1557.

[22] B. Kim, D.-H. Kim, J. Jung, and J.-O. Park, "A biomimetic undulatory tadpole robot using ionic polymermetal composite actuators," *Smart Materials and Structures*, vol. 14, no. 6, p. 1579, 2005.

[23] Z. Wang, G. Hang, J. Li, Y. Wang, and K. Xiao, "A micro-robot fish with embedded SMA wire actuated flexible biomimetic fin," *Sensors and Actuators A: Physical*, vol. 144, no. 2, pp. 354–360, Jun. 2008.

[24] K. H. Low and A. Willy, "Biomimetic motion planning of an undulating robotic fish fin," *Journal of Vibration and Control*, vol. 12, no. 12, pp. 1337–1359, Dec. 2006.

[25] C. Zhou, M. Tan, N. Gu, Z. Cao, S. Wang, and L. Wang, "The design and implementation of a biomimetic robot fish," *International journal of advanced robotic systems*, vol. 5, no. 2, pp. 185–192, 2008.

[26] A. J. Ijspeert, A. Crespi, D. Ryczko, and J.-M. Cabelguen, "From swimming to walking with a salamander robot driven by a spinal cord model," *Science*, vol. 315, no. 5817, pp. 1416–1420, Mar. 2007.

[27] P. Kodati, J. Hinkle, A. Winn, and X. Deng, "Microautonomous robotic ostraciiform (MARCO): Hydrodynamics, design, and fabrication," *IEEE Transactions on Robotics*, vol. 24, no. 1, pp. 105–117, Feb. 2008.

[28] M. Aureli, V. Kopman, and M. Porfiri, "Free-locomotion of underwater vehicles actuated by ionic polymer metal composites," *IEEE/ASME Transactions on Mechatronics*, vol. 15, no. 4, pp. 603–614, Aug. 2010.

[29] J. Wang, P. K. McKinley, and X. Tan, "Dynamic modeling of robotic fish with a base-actuated flexible tail," *Journal of Dynamic Systems, Measurement, and Control*, vol. 137, no. 1, p. 011004, Aug. 2014.

[30] G. V. Lauder, P. G. A. Madden, R. Mittal, H. Dong, and M. Bozkurttas, "Locomotion with flexible propulsors: I. Experimental analysis of pectoral fin swimming in sunfish," *Bioinspiration & Biomimetics*, vol. 1, no. 4, pp. S25–34, Dec. 2006.

[31] R. Mittal, H. Dong, M. Bozkurttas, G. Lauder, and P. Madden, "Locomotion with flexible propulsors: II. Computational modeling of pectoral fin swimming in sunfish," *Bioinspiration & Biomimetics*, vol. 1, no. 4, p. S35, 2006.

[32] J. Palmisano, R. Ramamurti, K. J. Lu, J. Cohen, W. Sandberg, and B. Ratna, "Design of a biomimetic controlled-curvature robotic pectoral fin," in *IEEE International Conference on Robotics and Automation (ICRA)*, Rome, Italy, Apr. 2007, pp. 966–973.

[33] K. A. Morgansen, T. M. L. Fond, and J. X. Zhang, "Agile maneuvering for fin-actuated underwater vehicles," in *Second International Symposium on Communications, Control and Signal Processing*, Marrakech, Morocco, Jan. 2006.

[34] D. Lachat, A. Crespi, and A. J. Ijspeert, “BoxyBot: a swimming and crawling fish robot controlled by a central pattern generator,” in *IEEE/RAS-EMBS International Conference on Biomedical Robotics and Biomechatronics (BIOROB)*, Pisa, Italy, Feb. 2006, pp. 643–648.

[35] P. E. Sitorus, Y. Y. Nazaruddin, E. Leksono, and A. Budiyono, “Design and implementation of paired pectoral fins locomotion of labriform fish applied to a fish robot,” *Journal of Bionic Engineering*, vol. 6, no. 1, pp. 37–45, Mar. 2009.

[36] N. Kato and T. Inaba, “Guidance and control of fish robot with apparatus of pectoral fin motion,” in *IEEE International Conference on Robotics and Automation (ICRA)*, vol. 1, Leuven, Belgium, May 1998, pp. 446–451.

[37] C. Rossi, W. Coral, J. Colorado, and A. Barrientos, “A motor-less and gear-less bio-mimetic robotic fish design,” in *IEEE International Conference on Robotics and Automation (ICRA)*, Shanghai, China, May 2011, pp. 3646–3651.

[38] G. V. Lauder, P. G. A. Madden, J. L. Tangorra, E. Anderson, and T. V. Baker, “Bioinspiration from fish for smart material design and function,” *Smart Materials and Structures*, vol. 20, no. 9, p. 094014, 2011.

[39] Z. Chen, S. Shatara, and X. Tan, “Modeling of biomimetic robotic fish propelled by an ionic polymer metal composite caudal fin,” *IEEE/ASME Transactions on Mechatronics*, vol. 15, no. 3, pp. 448–459, Jun. 2010.

[40] Z. Chen, T. I. Um, J. Zhu, and H. Bart-Smith, “Bio-inspired robotic cownose ray propelled by electroactive polymer pectoral fin,” in *ASME International Mechanical Engineering Congress and Exposition*, vol. 2. Denver, Colorado, USA: ASME, Jan. 2011, pp. 817–824.

[41] F. E. Fish and G. V. Lauder, “Passive and active flow control by swimming fishes and mammals,” *Annual Review of Fluid Mechanics*, vol. 38, no. 1, pp. 193–224, 2006.

[42] n. Mchenry, n. Pell, and n. Jr, “Mechanical control of swimming speed: stiffness and axial wave form in undulating fish models,” *The Journal of Experimental Biology*, vol. 198, no. Pt 11, pp. 2293–2305, 1995.

[43] J. Long, M. Hale, M. Mchenry, and M. Westneat, “Functions of fish skin: flexural stiffness and steady swimming of longnose gar, Lepisosteus osseus,” *Journal of Experimental Biology*, vol. 199, no. 10, pp. 2139–2151, Oct. 1996.

[44] K. A. Morgansen, B. I. Triplett, and D. J. Klein, "Geometric methods for modeling and control of free-swimming fin-actuated underwater vehicles," *IEEE Transactions on Robotics*, vol. 23, no. 6, pp. 1184–1199, Dec. 2007.

[45] E. Kanso, J. E. Marsden, C. W. Rowley, and J. B. Melli-Huber, "Locomotion of articulated bodies in a perfect fluid," *Journal of Nonlinear Science*, vol. 15, no. 4, pp. 255–289, Aug. 2005.

[46] S. D. Kelly and R. M. Murray, "Modelling efficient pisciform swimming for control," *International Journal of Robust and Nonlinear Control*, vol. 10, no. 4, pp. 217–241, Apr. 2000.

[47] Y.-H. Zhang, J.-H. He, J. Yang, S.-W. Zhang, and K. H. Low, "A computational fluid dynamics (CFD) analysis of an undulatory mechanical fin driven by shape memory alloy," *International Journal of Automation and Computing*, vol. 3, no. 4, pp. 374–381, 2006.

[48] H. Liu, R. Wassersug, and K. Kawachi, "A computational fluid dynamics study of tadpole swimming," *Journal of Experimental Biology*, vol. 199, no. 6, pp. 1245–1260, Jun. 1996.

[49] H. Dong, M. Bozkurttas, R. Mittal, P. Madden, and G. V. Lauder, "Computational modelling and analysis of the hydrodynamics of a highly deformable fish pectoral fin," *Journal of Fluid Mechanics*, vol. 645, pp. 345–373, Feb. 2010.

[50] P. W. Webb, "Kinematics of pectoral fin propulsion in Cymatogaster Aggregata," *Journal of Experimental Biology*, vol. 59, no. 3, pp. 697–710, Dec. 1973.

[51] ——, *Hydrodynamics and energetics of fish propulsion*. Dept. of the Environment Fisheries and Marine Service, 1975.

[52] R. W. Blake, "The mechanics of labriform locomotion I. Labriform locomotion in the Angelfish (Pterophyllum Eimekei): An analysis of the power stroke," *Journal of Experimental Biology*, vol. 82, no. 1, pp. 255–271, Oct. 1979.

[53] ——, "Short communications: The mechanics of Labriform locomotion: II. An analysis of the recovery stroke and the overall fin-beat cycle propulsive efficiency in the Angelfish," *Journal of Experimental Biology*, vol. 85, no. 1, pp. 337–342, Apr. 1980.

[54] F.-C. Chiu, C.-K. Chen, and J. Guo, "A practical method for simulating pectoral fin locomotion of a biomimetic autonomous underwater vehicle," in *International Symposium on Underwater Technology (UT)*, Taipei, Taiwan, Apr. 2004, pp. 323–329.

[55] N. Kato and M. Furushima, “Pectoral fin model for maneuver of underwater vehicles,” in *Symposium on Autonomous Underwater Vehicle Technology (AUV)*, Monterey, CA,USA, Jun. 1996, pp. 49–56.

[56] X. Deng and S. Avadhanula, “Biomimetic micro underwater vehicle with oscillating fin propulsion: System design and force measurement,” in *IEEE International Conference on Robotics and Automation (ICRA)*, Barcelona, Spain, Apr. 2005, pp. 3312–3317.

[57] S. Licht, V. Polidoro, M. Flores, F. S. Hover, and M. S. Triantafyllou, “Design and projected performance of a flapping foil AUV,” *IEEE Journal of Oceanic Engineering*, vol. 29, no. 3, pp. 786–794, Jul. 2004.

[58] I. Yamamoto, Y. Terada, T. Nagamatu, and Y. Imaizumi, “Propulsion system with flexible/rigid oscillating fin,” *IEEE Journal of Oceanic Engineering*, vol. 20, no. 1, pp. 23–30, Jan. 1995.

[59] F. S. Hover, . Haugsdal, and M. S. Triantafyllou, “Effect of angle of attack profiles in flapping foil propulsion,” *Journal of Fluids and Structures*, vol. 19, no. 1, pp. 37–47, Jan. 2004.

[60] M. Ruffo, “GhostSwimmer: Tactically relevant, biomimetically inspired, silent, highly efficient and maneuverable autonomous underwater vehicle,” *ONR STTR N08-030, US Navy*, Nov. 2010.

[61] J. L. Tangorra, S. N. Davidson, I. W. Hunter, P. G. A. Madden, G. V. Lauder, H. Dong, M. Bozkurttas, and R. Mittal, “The development of a biologically inspired propulsor for unmanned underwater vehicles,” *IEEE Journal of Oceanic Engineering*, vol. 32, no. 3, pp. 533–550, Jul. 2007.

[62] N. Kato, Y. Ando, A. Tomokazu, H. Suzuki, K. Suzumori, T. Kanda, and S. Endo, “Elastic pectoral fin actuators for biomimetic underwater vehicles,” in *Bio-mechanisms of Swimming and Flying*, N. Kato and S. Kamimura, Eds. Japan: Springer, 2008, pp. 271–282, dOI: 10.1007/978-4-431-73380-5.

[63] G. Barbera, “Analisi teorica e sperimentale di un sistema di controllo per un veicolo biomimetico Boxfish,” Master Thesis, University of Padua, Padua, Italy, 2008.

[64] K. Shoele and Q. Zhu, “Numerical simulation of a pectoral fin during labriform swimming,” *The Journal of Experimental Biology*, vol. 213, no. Pt 12, pp. 2038–2047, Jun. 2010.

[65] D. H. Thorsen, M. H. Green, and M. E. Hale, “Motor control of the Zebrafish pectoral fin,” *Integrative and Comparative Biology*, vol. 46, p. E257, 2006.

[66] C. D. Wilga and G. V. Lauder, “Locomotion in sturgeon: function of the pectoral fins,” *Journal of Experimental Biology*, vol. 202, no. 18, pp. 2413–2432, Sep. 1999.

[67] M. Ziegler and R. Pfeifer, “Sensory feedback of a fish robot with tunable elastic tail fin,” in *Biomimetic and Biohybrid Systems*, ser. Lecture Notes in Computer Science, N. F. Lepora, A. Mura, H. G. Krapp, P. F. M. J. Verschure, and T. J. Prescott, Eds. Springer Berlin Heidelberg, Jul. 2013, no. 8064, pp. 335–346, dOI: 10.1007/978-3-642-39802-5.

[68] Y.-J. Park, T. M. Huh, D. Park, and K.-J. Cho, “Design of a variable-stiffness flapping mechanism for maximizing the thrust of a bio-inspired underwater robot,” *Bioinspiration & Biomimetics*, vol. 9, no. 3, p. 036002, 2014.

[69] M. Nakabayashi, R. Kobayashi, S. Kobayashi, and H. Morikawa, “Bioinspired propulsion mechanism using a fin with a dynamic variable-effective-length spring,” *Journal of Biomechanical Science and Engineering*, vol. 4, no. 1, pp. 82–93, 2009.

[70] M. J. Lighthill, “Large-amplitude elongated-body theory of fish locomotion,” *Proceedings of the Royal Society of London B: Biological Sciences*, vol. 179, no. 1055, pp. 125–138, Nov. 1971.

[71] J. Wang and X. Tan, “Averaging tail-actuated robotic fish dynamics through force and moment scaling,” *IEEE Transactions on Robotics*, vol. 31, no. 4, pp. 906–917, Aug. 2015.

[72] S. D. Kelly, “The mechanics and control of robotic locomotion with applications to aquatic vehicles,” phD Thesis, California Institute of Technology, Pasadena, California, 1998.

[73] R. Mittal, “Computational modeling in biohydrodynamics: trends, challenges, and recent advances,” *IEEE Journal of Oceanic Engineering*, vol. 29, no. 3, pp. 595–604, Jul. 2004.

[74] K. A. Harper, M. D. Berkemeier, and S. Grace, “Modeling the dynamics of spring-driven oscillating-foil propulsion,” *IEEE Journal of Oceanic Engineering*, vol. 23, no. 3, pp. 285–296, Jul. 1998.

[75] R. Mason and J. W. Burdick, “Experiments in carangiform robotic fish locomotion,” in *IEEE International Conference on Robotics and Automation (ICRA)*, vol. 1, San Francisco, CA, Apr 2000, pp. 428–435.

[76] R. Mason, “Fluid locomotion and trajectory planning for shape-changing robots,” PhD Thesis, California Institute of Technology, Pasadena, California, 2003.

[77] J. Melli, C. Rowley, and D. Rufat, “Motion planning for an articulated body in a perfect planar fluid,” *SIAM Journal on Applied Dynamical Systems*, vol. 5, no. 4, pp. 650–669, Jan. 2006.

[78] E. Kanso, “Swimming due to transverse shape deformations,” *Journal of Fluid Mechanics*, vol. 631, pp. 127–148, Jul. 2009.

[79] J. E. Fontanella, F. E. Fish, E. I. Barchi, R. Campbell-Malone, R. H. Nichols, N. K. DiNenno, and J. T. Beneski, “Two- and three-dimensional geometries of batoids in relation to locomotor mode,” *Journal of Experimental Marine Biology and Ecology*, vol. 446, pp. 273–281, Aug. 2013.

[80] L. J. Rosenberger, “Pectoral fin locomotion in batoid fishes: undulation versus oscillation,” *The Journal of Experimental Biology*, vol. 204, no. Pt 2, pp. 379–394, Jan. 2001.

[81] N. Kato, B. W. Wicaksono, and Y. Suzuki, “Development of biology-inspired autonomous underwater vehicle “BASS III” with high maneuverability,” in *International Symposium on Underwater Technology (UT)*, Tokyo, Japan, 2000, pp. 84–89.

[82] J. Liu, I. Dukes, and H. Hu, “Novel mechatronics design for a robotic fish,” in *IEEE/RSJ International Conference on Intelligent Robots and Systems (IROS)*, Alberta, Canada, Aug. 2005, pp. 807–812.

[83] C. Phelan, J. Tangorra, G. Lauder, and M. Hale, “A biorobotic model of the sunfish pectoral fin for investigations of fin sensorimotor control,” *Bioinspiration & Biomimetics*, vol. 5, no. 3, p. 035003, Sep. 2010.

[84] S. Bazaz Behbahani and X. Tan, “A flexible passive joint for robotic fish pectoral fins: Design, dynamic modeling, and experimental results,” in *IEEE/RSJ International Conference on Intelligent Robots and Systems (IROS)*, Chicago, IL, USA, Sep. 2014, pp. 2832–2838.

[85] ——, “Design and dynamic modeling of a flexible feathering joint for robotic fish pectoral fins,” in *ASME Dynamic Systems and Control Conference (DSCC)*, vol. 1. San Antonio, Texas, USA: ASME, Oct. 2014, p. V001T05A005.

[86] ——, “Bio-inspired flexible joints with passive feathering for robotic fish pectoral fins,” *Bioinspiration & Biomimetics*, vol. 11, no. 3, p. 036009, Jun. 2016.

[87] ——, “Design and modeling of flexible passive rowing joint for robotic fish pectoral fins,” *IEEE Transactions on Robotics*, vol. 32, no. 5, pp. 1119–1132, Oct. 2016.

[88] T. I. Fossen, *Guidance and Control of Ocean Vehicles*, 1st ed. Chichester ; New York: Wiley, Aug. 1994.

[89] G. V. Lauder and E. G. Drucker, “Morphology and experimental hydrodynamics of fish fin control surfaces,” *IEEE Journal of Oceanic Engineering*, vol. 29, no. 3, pp. 556–571, Jul. 2004.

[90] S. Vogel, *Life in Moving Fluids: The Physical Biology of Flow*, 2nd ed. Princeton, N.J.: Princeton University Press, Apr. 1996.

[91] A. K. Banerjee and S. Nagarajan, “Efficient simulation of large overall motion of beams undergoing large deflection,” *Multibody System Dynamics*, vol. 1, no. 1, pp. 113–126, 1997.

[92] M. Nakashima, N. Ohgishi, and K. Ono, “A study on the propulsive mechanism of a double jointed fish robot utilizing self-excitation control,” *JSME International Journal Series C*, vol. 46, pp. 982–990, 2003.

[93] H. Suzuki, N. Kato, and K. Suzumori, “Load characteristics of mechanical pectoral fin,” *Experiments in Fluids*, vol. 44, no. 5, pp. 759–771, Nov. 2007.

[94] A. J. Clark, X. Tan, and P. K. McKinley, “Evolutionary multiobjective design of a flexible caudal fin for robotic fish,” *Bioinspiration & Biomimetics*, vol. 10, no. 6, p. 065006, Dec. 2015.

[95] M. S. Triantafyllou and G. S. Triantafyllou, “An efficient swimming machine,” *Scientific American*, vol. 272, pp. 64–70, Mar. 1995.

[96] J. J. Rohr and F. E. Fish, “Strouhal numbers and optimization of swimming by odontocete cetaceans,” *Journal of Experimental Biology*, vol. 207, no. 10, pp. 1633–1642, Apr. 2004.

[97] W. Wang and G. Xie, “CPG-based locomotion controller design for a Boxfish-like robot,” *International Journal of Advanced Robotic Systems*, vol. 11, no. 6, p. 87, Jun. 2014.

[98] A. Crespi, D. Lachat, A. Pasquier, and A. J. Ijspeert, “Controlling swimming and crawling in a fish robot using a central pattern generator,” *Autonomous Robots*, vol. 25, no. 1-2, pp. 3–13, Dec. 2007.

[99] J. Gao, S. Bi, Y. Xu, and C. Liu, “Development and design of a robotic manta ray featuring flexible pectoral fins,” in *IEEE International Conference on Robotics and Biomimetics (ROBIO)*, Sanya, China, Dec. 2007, pp. 519–523.

[100] Z. Chen, T. I. Um, and H. Bart-Smith, “Bio-inspired robotic manta ray powered by ionic polymermetal composite artificial muscles,” *International Journal of Smart and Nano Materials*, vol. 3, no. 4, pp. 296–308, Dec. 2012.

[101] N. Kato, “Control performance in the horizontal plane of a fish robot with mechanical pectoral fins,” *IEEE Journal of Oceanic Engineering*, vol. 25, no. 1, pp. 121–129, Jan. 2000.

[102] G. Barbera, L. Pi, and X. Deng, “Attitude control for a pectoral fin actuated bio-inspired robotic fish,” in *IEEE International Conference on Robotics and Automation (ICRA)*, Shanghai, China, May 2011, pp. 526–531.

[103] E. Drucker, J. Walker, and M. Westneat, “Mechanics of pectoral fin swimming in fishes,” *Fish Biomechanics*, pp. 369–423, Jan. 2006.

[104] R. G. Dong, *Effective mass and damping of submerged structures*. National Technical Information Service, Apr. 1978.

[105] J. J. Videler and F. Hess, “Fast continuous swimming of two Pelagic Predators, Saithe (Pollachius Virens) and Mackerel (Scomber Scombrus): a kinematic analysis,” *Journal of Experimental Biology*, vol. 109, no. 1, pp. 209–228, Mar. 1984.

[106] M. E. Hale, R. D. Day, D. H. Thorsen, and M. W. Westneat, “Pectoral fin coordination and gait transitions in steadily swimming juvenile reef fishes,” *The Journal of Experimental Biology*, vol. 209, no. Pt 19, pp. 3708–3718, Oct. 2006.

[107] J. M. Anderson and N. K. Chhabra, “Maneuvering and stability performance of a robotic tuna,” *Integrative and Comparative Biology*, vol. 42, no. 1, pp. 118–126, Feb. 2002.

[108] P. R. Bandyopadhyay, “Maneuvering hydrodynamics of fish and small underwater vehicles,” *Integrative and Comparative Biology*, vol. 42, no. 1, pp. 102–117, Feb. 2002.

[109] J.-D. Liu and H. Hu, “Biologically inspired behaviour design for autonomous robotic fish,” *International Journal of Automation and Computing*, vol. 3, no. 4, pp. 336–347, 2006.

[110] Q. S. Nguyen, S. Heo, H. C. Park, and D. Byun, “Performance evaluation of an improved fish robot actuated by piezoceramic actuators,” *Smart Materials and Structures*, vol. 19, no. 3, p. 035030, 2010.

[111] C. Rossi, J. Colorado, W. Coral, and A. Barrientos, “Bending continuous structures with SMAs: a novel robotic fish design,” *Bioinspiration & Biomimetics*, vol. 6, no. 4, p. 045005, Dec. 2011.

[112] L. Wen, T. M. Wang, G. H. Wu, and J. H. Liang, “Hydrodynamic investigation of a self-propelled robotic fish based on a force-feedback control method,” *Bioinspiration & Biomimetics*, vol. 7, no. 3, p. 036012, Sep. 2012.

[113] S. H. Kim, K. Shin, S. Hashi, and K. Ishiyama, “Magnetic fish-robot based on multi-motion control of a flexible magnetic actuator,” *Bioinspiration & Biomimetics*, vol. 7, no. 3, p. 036007, Sep. 2012.

[114] H. E. Daou, T. Salume, L. D. Chambers, W. M. Megill, and M. Kruusmaa, “Modelling of a biologically inspired robotic fish driven by compliant parts,” *Bioinspiration & Biomimetics*, vol. 9, no. 1, p. 016010, 2014.

[115] A. K. Kancharala and M. K. Philen, “Study of flexible fin and compliant joint stiffness on propulsive performance: theory and experiments,” *Bioinspiration & Biomimetics*, vol. 9, no. 3, p. 036011, Sep. 2014.

[116] S. Childress, *Mechanics of Swimming and Flying*, ser. Cambridge Studies in Mathematical Biology (Book 2). Cambridge: Cambridge University Press, Jul. 1981.

[117] K. H. Low and C. W. Chong, “Parametric study of the swimming performance of a fish robot propelled by a flexible caudal fin,” *Bioinspiration & Biomimetics*, vol. 5, no. 4, p. 046002, 2010.

[118] Y. Ko, S. Na, Y. Lee, K. Cha, S. Y. Ko, J. Park, and S. Park, “A jellyfish-like swimming mini-robot actuated by an electromagnetic actuation system,” *Smart Materials and Structures*, vol. 21, no. 5, p. 057001, 2012.

[119] S. Bazaz Behbahani and X. Tan, “Dynamic Modeling of Robotic Fish Caudal Fin With Electrorheological Fluid-Enabled Tunable Stiffness,” in *ASME 2015 Dynamic Systems and Control Conference (DSCC)*, vol. 3. Columbus, Ohio, USA: ASME, Oct. 2015, p. V003T49A006.

[120] A. Gibb, B. Jayne, and G. Lauder, “Kinematics of pectoral fin locomotion in the Bluegill Sunfish Lepomis Macrochirus,” *Journal of Experimental Biology*, vol. 189, no. 1, pp. 133–161, Apr. 1994.

[121] M. W. Westneat and J. A. Walker, “Applied aspects of mechanical design, behavior, and performance of pectoral fin swimming in fishes,” in *Special Session on Bio-Engineering Research Related to Autonomous Underwater Vehicles, 10th Intern. Symp. Unmanned Untethered Submersible Technology*, Jan. 1997, pp. 153–165.

[122] X. Deng, L. Schenato, W. C. Wu, and S. S. Sastry, “Flapping flight for biomimetic robotic insects: part I-system modeling,” *IEEE Transactions on Robotics*, vol. 22, no. 4, pp. 776–788, Aug. 2006.

[123] R. Bainbridge, “The speed of swimming of fish as related to size and to the frequency and amplitude of the tail beat,” *Journal of Experimental Biology*, vol. 35, no. 1, pp. 109–133, Mar. 1958.

[124] D. B. Quinn, G. V. Lauder, and A. J. Smits, “Scaling the propulsive performance of heaving flexible panels,” *Journal of Fluid Mechanics*, vol. 738, pp. 250–267, Jan. 2014.

[125] ——, “Maximizing the efficiency of a flexible propulsor using experimental optimization,” *Journal of Fluid Mechanics*, vol. 767, pp. 430–448, Mar. 2015.

[126] S. Alben, C. Witt, T. V. Baker, E. Anderson, and G. V. Lauder, “Dynamics of freely swimming flexible foils,” *Physics of Fluids (1994-present)*, vol. 24, no. 5, p. 051901, May 2012.

[127] S. Michelin and S. G. L. Smith, “Resonance and propulsion performance of a heaving flexible wing,” *Physics of Fluids (1994-present)*, vol. 21, no. 7, p. 071902, Jul. 2009.

[128] D. S. Barrett, “Propulsive efficiency of a flexible hull underwater vehicle,” PhD Thesis, Massachusetts Institute of Technology, 1996.

[129] R. Fan, J. Yu, L. Wang, G. Xie, Y. Fang, and Y. Hu, “Optimized design and implementation of biomimetic robotic dolphin,” in *IEEE International Conference on Robotics and Biomimetics (ROBIO)*, 2005, pp. 484–489.

[130] K. H. Low, “Modelling and parametric study of modular undulating fin rays for fish robots,” *Mechanism and Machine Theory*, vol. 44, no. 3, pp. 615–632, Mar. 2009.

[131] J. L. Tangorra, G. V. Lauder, I. W. Hunter, R. Mittal, P. G. A. Madden, and M. Bozkurttas, “The effect of fin ray flexural rigidity on the propulsive forces generated by a biorobotic fish pectoral fin,” *Journal of Experimental Biology*, vol. 213, no. 23, pp. 4043–4054, Dec. 2010.

[132] E. Kanso and P. K. Newton, “Passive locomotion via normal-mode coupling in a submerged springmass system,” *Journal of Fluid Mechanics*, vol. 641, pp. 205–215, Dec. 2009.

[133] B. Ahlborn, S. Chapman, R. Stafford, and R. Harper, “Experimental simulation of the thrust phases of fast-start swimming of fish,” *The Journal of Experimental Biology*, vol. 200, no. Pt 17, pp. 2301–2312, 1997.

[134] H. E. Daou, T. Salume, A. Ristolainen, G. Toming, M. Listak, and M. Kruusmaa, “A biomimetic design and control of a fish-like robot using compliant structures,” in *15th International Conference on Advanced Robotics (ICAR)*, Tallinn, Jun. 2011, pp. 563–568.

[135] Y. J. Park, U. Jeong, J. Lee, S. R. Kwon, H. Y. Kim, and K. J. Cho, “Kinematic condition for maximizing the thrust of a robotic fish using a compliant caudal fin,” *IEEE Transactions on Robotics*, vol. 28, no. 6, pp. 1216–1227, Dec. 2012.

[136] S. Bazaz Behbahani and X. Tan, “Role of pectoral fin flexibility in robotic fish performance,” *Journal of Nonlinear Science*, 2016, submitted.

[137] S. Kobayashi, T. Ozaki, M. Nakabayashi, H. Morikawa, and A. Itoh, “Bioinspired aquatic propulsion mechanisms with real-time variable apparent stiffness fins,” in *IEEE International Conference on Robotics and Biomimetics (ROBIO)*, Dec. 2006, pp. 463–467.

[138] M. Nakabayashi, R. Kobayashi, S. Kobayashi, and H. Morikawa, “A novel propulsion mechanism using a fin with a variable-effective-length spring,” in *IEEE International Conference on Robotics and Biomimetics (ROBIO)*, Feb. 2009, pp. 1515–1521.

[139] M. Ziegler, M. Hoffmann, J. P. Carbajal, and R. Pfeifer, “Varying body stiffness for aquatic locomotion,” in *IEEE International Conference on Robotics and Automation (ICRA)*, Shanghai, China, May 2011, pp. 2705–2712.

[140] J. E. Lindler and N. M. Wereley, “Double adjustable shock absorbers using electrorheological fluid,” *Journal of Intelligent Material Systems and Structures*, vol. 10, no. 8, pp. 652–657, Aug. 1999.

[141] T. Nakamura, N. Saga, and M. Nakazawa, “Impedance control of a single shaft-type clutch using homogeneous electrorheological fluid,” *Journal of Intelligent Material Systems and Structures*, vol. 13, no. 7-8, pp. 465–469, Jul. 2002.

[142] R. A. DiTaranto, “Theory of vibratory bending for elastic and viscoelastic layered finite-length beams,” *Journal of Applied Mechanics*, vol. 32, no. 4, pp. 881–886, Dec. 1965.

[143] Z.-F. Yeh and Y.-S. Shih, “Critical load, dynamic characteristics and parametric instability of electrorheological material-based adaptive beams,” *Computers & Structures*, vol. 83, no. 2526, pp. 2162–2174, Sep. 2005.

[144] K. Wei, G. Meng, W. Zhang, and S. Zhou, “Vibration characteristics of rotating sandwich beams filled with electrorheological fluids,” *Journal of Intelligent Material Systems and Structures*, vol. 18, no. 11, pp. 1165–1173, Nov. 2007.

[145] J. E. Sader, "Frequency response of cantilever beams immersed in viscous fluids with applications to the atomic force microscope," *Journal of Applied Physics*, vol. 84, no. 1, pp. 64–76, Jul. 1998.

[146] J. Chung and H. H. Yoo, "Dynamic analysis of a rotating cantilever beam by using the finite element method," *Journal of Sound and Vibration*, vol. 249, no. 1, pp. 147–164, Jan. 2002.

[147] K. Wei, W. Zhang, P. Xia, and Y. Liu, "Nonlinear dynamics of an electrorheological sandwich beam with rotary oscillation," *Journal of Applied Mathematics*, vol. 2012, p. e659872, Dec. 2012.

[148] E. H. K. Fung and D. T. W. Yau, "Vibration characteristics of a rotating flexible arm with ACLD treatment," *Journal of Sound and Vibration*, vol. 269, no. 12, pp. 165–182, Jan. 2004.

[149] H. Block and J. P. Kelly, "Electro-rheology," *Journal of Physics D: Applied Physics*, vol. 21, no. 12, p. 1661, 1988.

[150] K. D. Weiss, J. D. Carlson, and J. P. Coulter, "Review : Material aspects of electrorheological systems," *Journal of Intelligent Material Systems and Structures*, vol. 4, no. 1, pp. 13–34, Jan. 1993.

[151] J.-Y. Yeh, L.-W. Chen, and C.-C. Wang, "Dynamic stability of a sandwich beam with a constrained layer and electrorheological fluid core," *Composite Structures*, vol. 64, no. 1, pp. 47–54, Apr. 2004.

[152] M. Yalcintas and J. P. Coulter, "Electrorheological material based non-homogeneous adaptive beams," *Smart Materials and Structures*, vol. 7, no. 1, p. 128, 1998.